DOE/ER/01198--1403

DE84 000468

MOMENTUM DENSITY OF HCP AND LIQUID HELIUM-4 BY INELASTIC NEUTRON SCATTERING

BY

RUSSELL OTTO HILLEKE

B.S., Georgia Institute of Technology, 1973
M.S., University of Illinois, 1976

THESIS

Submitted in partial fulfillment of the requirements
for the degree of Doctor of Philosophy in Physics
in the Graduate College of the
University of Illinois at Urbana-Champaign, 1983

Urbana, Illinois

PACS Indices: 67.30.-s
61.12.Fy
63.90.+t

DISCLAIMER

MOMENTUM DENSITY OF HCP AND LIQUID HELIUM-4 BY INELASTIC NEUTRON SCATTERING

BY

RUSSELL OTTO HILLEKE

B.S., Georgia Institute of Technology, 1973
M.S., University of Illinois, 1976

THESIS

Submitted in partial fulfillment of the requirements
for the degree of Doctor of Philosophy in Physics
in the Graduate College of the
University of Illinois at Urbana-Champaign, 1983

Urbana, Illinois

PACS Indices: 67.30.-s
61.12.Fy
63.90.+t

DISCLAIMER

MOMENTUM DENSITY OF HCP AND LIQUID HELIUM-4 BY INELASTIC NEUTRON SCATTERING

Russell Otto Hilleke, Ph.D.
Department of Physics
University of Illinois at Urbana-Champaign, 1983

A measurement of the momentum density in hcp and liquid ^{4}He by inelastic neutron scattering is reported. Using the Low Resolution Medium Energy Chopper Spectrometer at the Intense Pulsed Neutron Source at Argonne National Laboratory, momentum transfers in the range 12 to 22.5 $\mathring{A}^{-1}$ were attained. At these momentum transfers, the momentum density of the sample is related to the dynamic structure factor by the impulse approximation.

The measured momentum distribution is Gaussian and the kinetic energy is larger than proposed by existing theories.

Data were taken on two solid samples, the first was a 19.45 cm^3/mole hcp solid, the second was 18.20 cm^3/mole; both solid samples were maintained at 1.70 K during data collection. Data were also taken on a liquid sample with a molar volume of 18.20 cm^3/mole at 4.00 K. At 1.70 K the two solid samples are essentially in their ground states so that the measurement is of the ground state momentum density. The liquid sample was included to see if the difference between the liquid and solid momentum density at the same molar volume was observable.

ACKNOWLEDGMENTS

I sincerely thank my advisor, Professor Ralph O. Simmons, for his patience, guidance and support throughout the course of this work. Thank you, Dr. Praveen Chaddah, for help with all phases of the experiment from its inception to the final data analysis. I thank Dr. David L. Price and Dr. Sunil K. Sinha for the benefit of their vast experience in neutron scattering. Thanks to Dr. Steve Marx for his help with the temperature control and measurement electronics. I appreciate the help of Dr. Dick Fraass, Dr. Paul Granfors, Dr. Paul Sokol, Steve Ehrlich, John Thorpe and Matt Kim.

The running of a facility like the Intense Pulsed Neutron Source requires the cooperation of a large group of very talented individuals; I appreciate the efforts of everyone associated with IPNS who helped make this such a successful experiment. Thank you, Dave Leach and Don Bohringer, for your help in setting up the equipment. Thank you, Bob Kleb, for your help in stopping the vacuum leaks. Thanks to George Ostrowski for keeping the chopper running properly. To Charles Potts and the accelerator operators, thank you for the neutrons.

Thank you, Dr. Paula Whitlock, for providing results from unpublished calculations and details about

published calculations. I hope you don't mind the liberties I've taken with your results in Chapter 6.

Most importantly I would like to thank my parents for their love, support and encouragement through the years. Thanks also to my brothers and sisters, nephews and niece for their interest and encouragement.

This research was supported by the U.S. Department of Energy through the contract DOE-DE-AC01-76ER01198.

TABLE OF CONTENTS

LIST OF SYMBOLS

Symbol	Meaning
$\frac{d^2\sigma}{d\Omega dE}$	= inelastic neutron scattering cross-section per unit solid angle per unit energy
σ	= neutron scattering cross-section in barns
b	= scattering length
$S(\phi,E)$	= scattering function for data collected at a fixed angle
$S(\vec{Q},E)$	= dynamic structure factor
σ_ϕ	= width (standard deviation) of $S(\phi,E)$
σ_Q	= width (standard deviation) of $S(\vec{Q},E)$
σ_R	= width (standard deviation) of spectrometer's resolution
ϕ	= angle between incident and final neutron momentum
m	= neutron mass
M	= ^{4}He atomic mass
$\hbar\vec{k}_i$	= initial neutron momentum
$\hbar\vec{k}_f$	= final neutron momentum
$\vec{Q}$	= momentum transfer = $\vec{k}_i - \vec{k}_f$
E_i	= initial neutron kinetic energy = $\frac{\hbar^2 k_i^2}{2M}$
E_f	= final neutron kinetic energy = $\frac{\hbar^2 k_f^2}{2M}$
E	= energy transfer = $E_i - E_f$
ϵ	= energy coefficient in Lennard-Jones potential = 10.22 K

σ_L = hard core diameter in Lennard-Jones potential = 2.556 Å

ρ = density in units of atoms per volume

E_1 = kinetic energy of helium atom before the collision

$\hbar\vec{p}_1$ or $\hbar\vec{p}$ = momentum of helium atom before the collision

$n(\vec{p})$ = momentum density of ^{4}He atoms

1. INTRODUCTION

The years 1982 and 1983 are the fiftieth anniversary of the discovery of the neutron by James Chadwick[1] and the seventy-fifth anniversary of the first liquefaction of helium by Kamerlingh Onnes.[2] It seems an appropriate time to study the scattering of neutrons from the condensed phases of helium. This historical coincidence also gives one the opportunity to introduce the subject of solid helium by saying something other than:

A. Background

Because of their relatively simple atomic structure, the noble gases have attracted much theoretical and experimental interest. That these elements occur in the gaseous phase at room temperature and atmospheric pressure is an indication of their weak interatomic attraction. The filled electron shells, which are characteristic of the noble gases, insure that the interaction between atoms is isotropic and that they solidify in a monatomic basis. This monatomic nature in the solid phase further simplifies their physical nature by eliminating internal vibrational and rotational degrees of freedom.

The long-range interaction between two noble gas atoms is due to the mutually induced multipole moments in their electron charge distributions. The leading term in

this attractive potential (the dipole-dipole term) is proportional to r^{-6}, where r is the interatomic distance.[3] As the atoms approach one another, their electron clouds overlap and the resultant repulsion, arising from the Pauli principle, is approximately described by an exponential or a large power of r.[4] The potential most commonly used to describe the overall interaction is the Lennard-Jones potential which is written in the form

$$V(r) = 4\varepsilon[(\frac{\sigma_L}{r})^{12} - (\frac{\sigma_L}{r})^6] \qquad (1)$$

where σ_L, often called the hard-core diameter, measures the spatial scale of the interaction and ε measures its strength. Gas phase experimental data on helium give the values $\sigma_L = 2.556$ Å and $\varepsilon = 10.22$ K for these parameters.[5] Some recent calculations[6] have found the HFDHE2 potential[7] to give better results for calculations on solid helium. This potential has eight parameters fitted from experiment.

Solid helium has been called a quantum solid[8] because the zero point kinetic energy of a helium atom in the solid is comparable to the (negative) potential energy due to its neighbors. In fact, the zero point kinetic energy is greater than the potential energy and the solid phase does not exist unless external pressure is applied. Figure 1, the low temperature phase diagram for ^{4}He, illustrates a variety of interesting phenomena that occur in the liquid and solid phases. Among the important

features in this figure are: 1) helium remains a liquid all the way to zero temperature at low pressures, 2) ^{4}He requires a pressure of at least 2.5 MPa to solidify, 3) the largest portion of the low pressure phase diagram for solid ^{4}He is taken up by the hcp phase (close packed, 12 nearest neighbors), 4) a bcc phase (not close packed, 8 nearest neighbors) exists over a very small range of pressure and temperature, and 5) ^{4}He becomes a superfluid at about 2. K. Important features that do not appear in Figure 1 are: 1) above 100 MPa and 15 K there is a fcc phase (close packed, 12 nearest neighbors), and 2) there exists a critical point at 5.20 K and 0.23 MPa. The numerals 1 through 3 in the figure indicate the pressure and temperature of the three samples on which data were taken in this experiment. In contrast to ^{4}He, the heavier noble gases solidify in fcc structures at temperatures that range from 24 K for Neon[11] to 202 K for Radon.[12]

The aforementioned large zero point energy of solid helium means that the RMS deviation ($\langle u^2 \rangle^{1/2}$) of an atom from its lattice site is large, as large as 1/3 of the nearest neighbor distance in ^{3}He.[13] These large excursions of the atoms from their lattice sites have three important consequences:[14] 1) Neighboring atoms in the lattice encounter one another away from their respective lattice sites at distances comparable with the hard core diameter of the interatomic potential. Because of this,

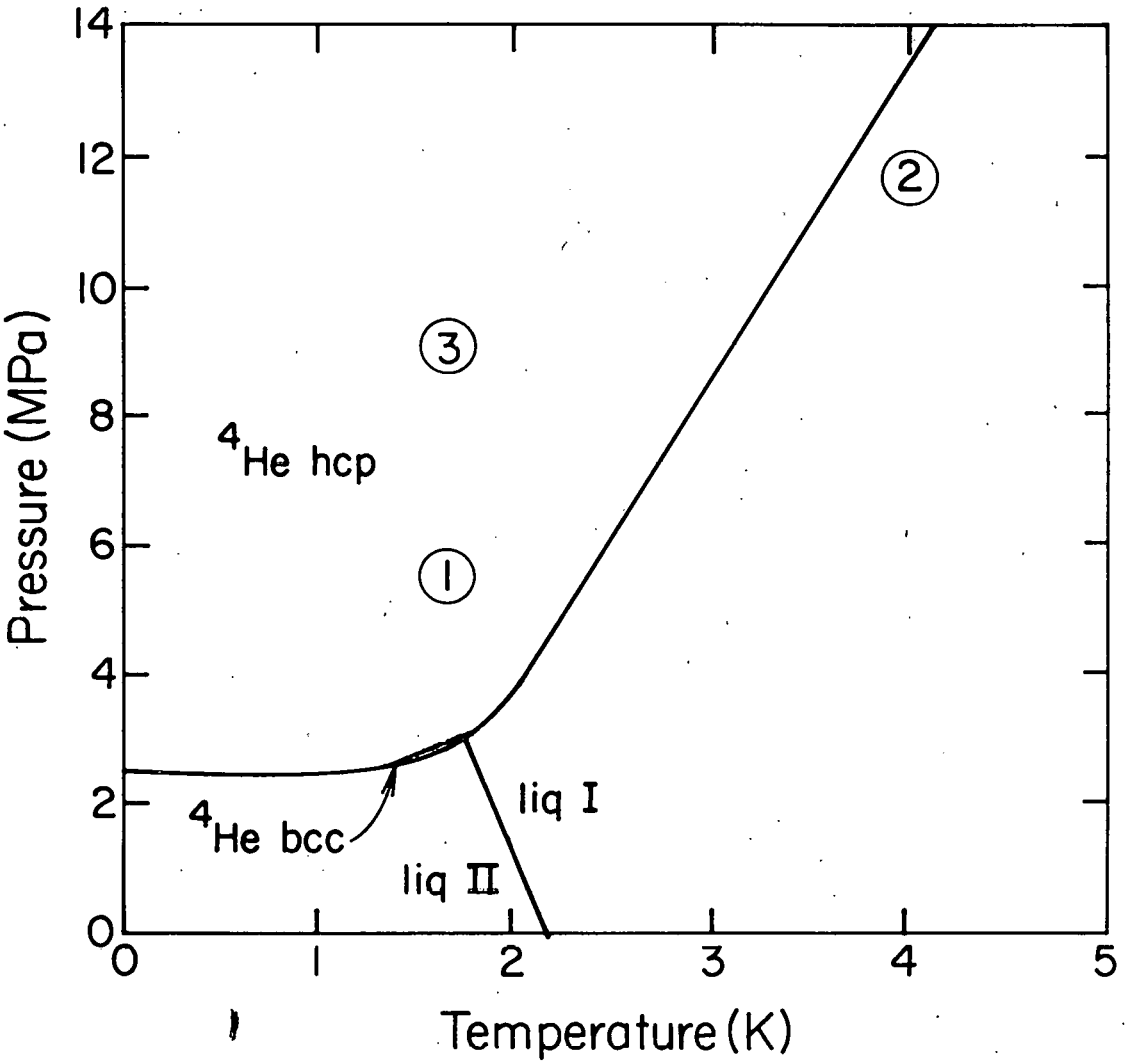

Figure 1. P-T phase diagram of ^{4}He. The temperature and pressure of the three samples are indicated and correspond to: 1) 19.45 cm^3/mole hcp ^{4}He, 2) 18.20 cm^3/mole liquid ^{4}He, and 3) 18.20 cm^3/mole hcp ^{4}He. These curves are compiled from data in references 9 and 10.

the motion of neighboring atoms is strongly correlated. In contrast, an atom in a "classical" solid sees its neighbors as localized and distant. 2) The small parameter of classical lattice dynamics, $(\langle u^2 \rangle^{1/2})/R_o$ (R_o is the near neighbor distance), is not small. Thus the harmonic approximation breaks down in the case of solid helium. This was demonstrated by de Wette and Nijboer[15] who found that the phonon frequencies for a solid with an interatomic potential and density appropriate for helium to be imaginary at all wavelengths. 3) The wave functions of neighboring atoms have substantial overlap. This leads to a significant probability for the atoms to tunnel around one another and thus exchange lattice sites. These exchange effects give rise to excitations that are important in determining the properties of solid helium.

B. Solid Helium Theories

A 1976 review article by H. R. Glyde[13] discusses the difficulties one faces in calculating the properties of solid helium and the various methods developed by theorists to carry out such calculations. An early cell model calculation by Bernardes[16] was in good agreement with experiment for various properties (compressibility, Gruneisen parameter, volume vs. pressure relation, and heat of sublimation) of the heavier noble gas solids but gave poor results for helium. A Hartree calculation using the Lennard-Jones interaction potential by Nosanow and

Shaw[17] showed that for the heavier noble gas solids the many-atom wave function could be written as a product of single-atom Gaussian functions:

$$\phi(\vec{r}) = C \exp\left(-\frac{1}{2} Ar^2\right) \tag{2}$$

where A is a variational parameter that determines the width of the wave function (higher A implies a narrower wave function). The values they found for the ground state energy of the heavier noble gas solids compared very well with experiment but their model gave poor results for helium. For helium they found that the wave function should look more like a cosine function appropriate for a square well potential. They concluded that the short range correlations are important in helium and that the effects of the potential's hard core should be more explicitly included in the calculation. Nosanow included these effects in a later paper[8] by using a Jastrow type function[18] in the many-atom wave function

$$\psi(\vec{r}, \ldots \vec{r}_N) = \prod_{i=1}^{N} \phi(\vec{r}_i - \vec{R}_i) \prod_{1 \le j < k \le N} f(r_{jk}) \tag{3}$$

where the Jastrow function was taken to be of the form

$$f(r) = \exp\left\{-K\left[\left(\frac{\sigma_L}{r}\right)^{12} - \left(\frac{\sigma_L}{r}\right)^{6}\right]\right\} \tag{4}$$

and K is a variational parameter. The resultant cluster expansion, in which one and two body terms were kept, gave

improved ground state energies and values for the compressibility and pressure that agreed well with experiment. This work was very important in the development of the theory of solid helium because it was the first internally consistent calculation that produced good agreement with experiment. Hetherington et al. showed that the three body terms were small for bcc ^{3}He.[19] An alternate method for treating the problem of particle correlations due to a hard-core potential is the T matrix method developed by Bruechner[20] for describing correlations of nucleons. This method was first applied to the problem of solid helium by Iwamoto and Namaizawa[21] and developed further by several authors.[22,23,24] Finally, Monte Carlo calculations[25,26] have been carried out on solid and liquid helium using a variety of potentials.[27] These calculations give good results for a variety of experimentally observable properties.

Many of these papers report either values of the Gaussian parameter A (Equation (2)), the total energy of the solid, or single-atom kinetic energies. The values they find for these quantities vary significantly. This led Praveen Chaddah, one of our collaborators and an expert on Compton scattering, to conclude that the neutron analog of Compton scattering should be sufficiently sensitive to test which of these calculations gives the best value for the kinetic energy. We soon realized that comparing the

calculated values of A is not proper; that the many-atom wave functions are written differently implies that the wave function is not fully characterized by the value of A. For this reason, we must compare our results with a theory that either writes the many-atom wave function as a product of single-atom wave functions or that calculates an observable of the system such as kinetic energy. Comparison will be made between these experimental results and the theoretical calculation of Whitlock et al.[25] because the Green's Function Monte Carlo method treats model calculations exactly, subject only to sampling error, and because they calculate a variety of observable properties in addition to the kinetic energy.

C. Inelastic Scattering Experiments

Compton scattering[28] is an experimental method used to determine the electron momentum density of a system by inelastic scattering of relatively high energy photons. The experimental method we describe here consists of (relatively) high energy inelastic neutron scattering to determine the atomic momentum density of condensed matter. Solid helium turns out to be an excellent system to study, not only because its momentum density is unknown, but also because its low mass insures that the neutrons scattered from the sample are easy to separate from the background scattering.

Knowledge of the momentum density is useful in determining properties other than the kinetic energy contribution to the system's total energy. The single-atom position-space wave function is related to the momentum density via the Fourier transform. Vacancy formation and motion are extremely sensitive to the width of the single-atom position-space wave function. In the case of solid helium, vacancies turn out to be important excitations in determining the properties of the solid.[29]

Neutron scattering provides a uniquely useful probe for the investigation of the properties of condensed matter. Neutrons with kinetic energies in the range 5 to about 100 meV are termed thermal neutrons; those with higher energy, and shorter wavelength, are called epithermal neutrons. Thermal neutrons have several properties that make them particularly useful in the study of properties of condensed matter.[30] With wavelengths in the range 1. to 4. Å, thermal neutrons have wavelengths that are well matched to atomic spacings in solids making neutron diffraction useful for the study of crystal structure. The kinetic energy range of thermal neutrons is of the same order as that of many excitations in condensed matter (phonons, magnons, rotons, etc.). Consequently, when a neutron is scattered inelastically by the creation or annihilation of an excitation, the change in energy of the

neutron is a large fraction of its initial energy, making the energy transfer easily observable.

Neutrons, being uncharged, can penetrate deeply into the sample to probe bulk properties of the solid. Neutrons are scattered by nuclear forces which depend on the isotope that comprises the scatterer. Since the scattering cross-sections of atoms with nearly equal atomic number differ considerably, even for isotopes of the same element, these atoms (e.g. ^{12}C, ^{14}N, and ^{16}O) can be distinguished more readily than with x-rays. Likewise, atoms such as hydrogen which are virtually invisible to x-rays, are strong neutron scatterers. Finally, the neutron's magnetic moment provides a means to study the density and arrangement of unpaired electrons, nuclear magnetic ordering, and the energies of magnetic excitations.

The neutron, acting as a microscopic probe, can be thought of as having a resolution on the order of its wavelength. If this wavelength is comparable to the interparticle spacing, the neutron scatters from the crystal lattice and one gets information about collective excitations in the solid. If the wavelength is very much smaller than the interparticle spacing, the scattering takes place from individual atoms and one obtains information about single-atom motion. In the short wavelength limit, one can take the following view of the scattering event: the helium atom is oscillating in its potential well colliding

with its nearest neighbors as it does so. If the neutron has sufficient kinetic energy, the interaction between the atom and the neutron can occur while the atom is between collisions with its neighbors. The frequency with which the atom oscillates is just a characteristic energy of the atom divided by Planck's constant.[31] So if the neutron energy is very much greater than a typical excitation energy in the system, the scattering is expected to give information about the dynamics of single atoms in the system. As is usually the case, such classical arguments are useful in understanding the physics behind the experiment but one can easily take such arguments too seriously. The approximations we make will result in predictions about the data which we can test to establish the validity of the approximations.

The experiment reported here consists of scattering relatively high energy neutrons from hcp ^{4}He. If sufficient momentum transfer is attained, the momentum distribution of the atoms in the solid can be extracted from the scattered neutron spectrum. The theory that describes this method will be discussed in detail in Chapter 2.

2. THEORY

A. Dynamic Structure Factor

For inelastic scattering of neutrons, the partial differential cross-section is related to the dynamic structure factor via

$$\frac{d^2\sigma}{d\Omega dE} = b^2 \frac{k_f}{k_i} S(\vec{Q},E) \tag{5}$$

where the usual definitions of the quantities apply (see List of Symbols). Van Hove showed that the dynamic structure factor, $S(\vec{Q},E)$, which is the time and space Fourier transform of the atom-atom correlation function, contains all the structural and dynamic information about the scattering system.[32] The fact that the dynamic structure factor is a function only of the energy and momentum transfer is important since it greatly reduces the amount of data necessary to describe the function.

Heuristically one can derive an expression for the dynamic structure factor based on the view of the scattering event discussed in the introduction. Recall that the classical view we took was that the collision between the neutron and the helium atom occurs instantaneously while the atom is between collisions with its neighbors and that we could therefore treat the atom as being free. If one

envisions a collision between a neutron (with kinetic energy E_i and wavevector $\vec{k}_i$) and a helium atom (with kinetic energy E_1 and wavevector $\vec{p}_1$), one can write down expressions for conservation of momentum and energy during the neutron-atom collision. Using E_2 and $\vec{p}_2$ as the energy and wavevector for the helium atom after the collision and E_f and $\vec{k}_f$ as the neutron's final energy and wavevector, these equations are

$$\vec{k}_i + \vec{p}_1 = \vec{k}_f + \vec{p}_2 \tag{6}$$

and

$$E_i + E_1 = E_f + E_2. \tag{7}$$

The relationship between the momentum and the energy of the helium atom is

$$E_1 = \frac{\hbar^2 p_1^2}{2M} \tag{8}$$

with like expressions for the other energy-momentum pairs. Combining these with the definitions of momentum transfer, $\vec{Q}$, and energy transfer E,

$$\vec{Q} = \vec{k}_i - \vec{k}_f \tag{9}$$

and

$$E = E_i - E_f \tag{10}$$

one finds

$$E - \frac{\hbar^2 Q^2}{2M} - \frac{\hbar^2 \vec{Q}\cdot\vec{p}_1}{M} = 0 \ . \qquad (11)$$

Thus Equation (11) expresses energy and momentum conservation for the collision; that is, we expect no scattering unless this equation is satisfied. We therefore want to put this expression inside a delta function in our expression for the dynamic structure factor. Finally, the probability of a scattering event having a given value of E and $\vec{Q}$ should be proportional to the probability of finding a helium atom with momentum, $\hbar\vec{p}_1$, that will satisfy Equation (11). Putting all this together and integrating over all values of the helium atom momentum, we find

$$S(\vec{Q},E) = \int n(\vec{p}_1)\ \delta(E - \frac{\hbar^2 Q^2}{2M} - \frac{\hbar^2 \vec{Q}\cdot\vec{p}_1}{M})\ d^3p_1 . \qquad (12)$$

This is referred to as the impulse approximation. The justification for the impulse approximation will be discussed in greater depth later in this chapter. An important point to note about Equation (12) is that the initial helium momentum, $\hbar\vec{p}_1$, is dotted into $\vec{Q}$ inside the delta function. Thus the quantity we deduce, since we measure E and $\vec{Q}$, is the component of $\vec{p}_1$ parallel to $\vec{Q}$.

If the single-atom wave function for helium atoms in the solid or liquid can be written as an isotropic Gaussian in the form of Equation (2), then the momentum wave function is

$$\chi\ (\vec{p}) = C\ \exp(-p^2/2A) \tag{13}$$

and the momentum density, which is the square of the momentum space wave function, is

$$n(\vec{p}) = (\pi A)^{-3/2}\ \exp(-p^2/A)\ . \tag{14}$$

If this equation is inserted into Equation (12), we find that the dynamic structure factor reduces to

$$S(\vec{Q},E) = C\ \exp(-q^2/A) \tag{15}$$

where

$$q = \frac{M}{\hbar^2 Q}\ [E - \frac{\hbar^2 Q^2}{2M}]\ . \tag{16}$$

From the above equations, we see that the peak of $S(\vec{Q},E)$ occurs when q is equal to zero, that is, when

$$E = E_r = \frac{\hbar^2 Q^2}{2M} \tag{17}$$

where we define the recoil energy, E_r, as the average energy lost by the neutrons in a given data peak. The recoil energy is the energy that would be lost by a neutron in an elastic (meaning kinetic energy conserving) collision between a neutron and a ^{4}He atom initially at rest. Combining Equations (15), (16), and (17) we find

$$S(\vec{Q},E) = C\ \exp[-\frac{(E-E_r)^2}{\hbar^4 Q^2 A/M^2}]\ . \tag{18}$$

This is an important equation and one should notice several points about it. At a given momentum transfer, $S(\vec{Q},E)$ is Gaussian and is centered at an energy transfer of E_r (see Equation (17)) and has a variance equal to

$$\sigma_Q^2 = \frac{\hbar^4 Q^2 A}{2M^2} \quad . \tag{19}$$

Further, the Gaussian parameter, A, that occurs in the single-particle wave function and the momentum density (Equation (14)) is the same A that occurs in Equation (19). So the center of the peak is determined by the mass of the scattering atom while the width of the peak is determined by the momentum density. By fitting our experimentally determined $S(\vec{Q},E)$ to Equation (18), we can extract the Gaussian parameter, A.

Equations (17) and (19) provide us with necessary (though some argue not sufficient) conditions for the validity of the impulse approximation. If we plot the peak value of E versus Q^2 for each data peak, the points should lie on a straight line whose intercept is zero and whose slope depends only on constants and the ^{4}He atomic mass. Further, if we plot σ_Q versus Q for each peak, the points should fall on a straight line whose intercept is zero and whose slope depends on constants, the ^{4}He atomic mass, and the Gaussian parameter A. So we can extract A from the slope of this straight line plot.

If we assume a momentum density given by Equation (14), we can calculate the average kinetic energy per atom; it is

$$\langle KE \rangle = \frac{3}{4} \hbar^2 \frac{A}{M} . \qquad (20)$$

This is an equation that is useful in comparing our results with theories, which often quote ground state kinetic energies rather than momentum densities.

B. Time-of-Flight Techniques

Pulsed neutron sources are well suited for time-of-flight experimental methods.[33] Time-of-flight methods involve determining the energy of a neutron by measuring the time it takes the neutron to traverse a known distance. In a neutron spectroscopic experiment, one obtains information about the dynamics of the sample. Neutron spectroscopy involves measuring the energy and momentum transferred between the neutron and the sample during each scattering event. The energy and momentum transfer are related to the energy and momentum of the excitation that is created or destroyed during the scattering event. Thus one must determine the energy and momentum of the neutron before and after the scattering event. This can be accomplished using the Low Resolution Medium Energy Chopper Spectrometer[34] (LRMECS) shown schematically in Figure 2. In this direct geometry (meaning the incident neutron

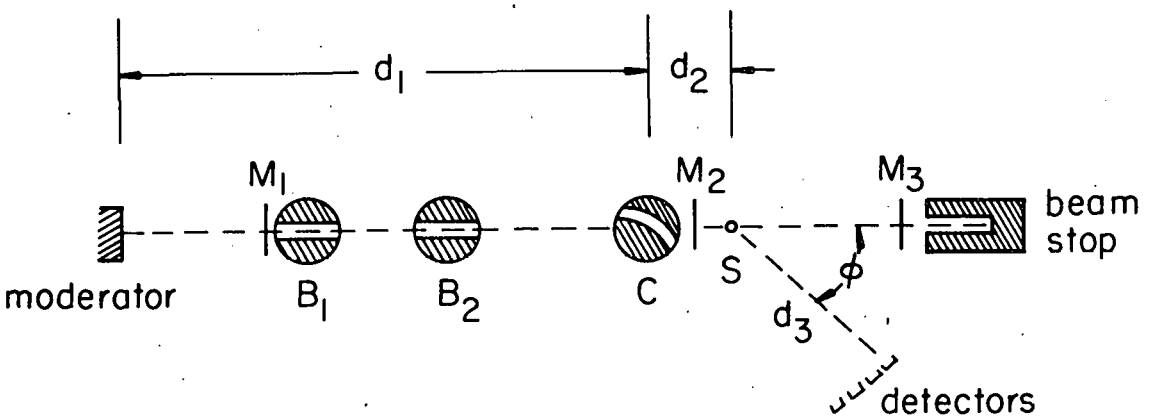

Figure 2. A schematic diagram of the Low Resolution Medium Energy Chopper Spectrometer (LRMECS) at IPNS-1. (C) The curved slit Fermi chopper that determines the energy of the neutrons incident on the sample. (S) The sample. (M_1) and (M_2) and (M_3) ^{3}He filled beam monitors that measure the neutron beam's flux and energy distribution. (d_1) Moderator-to-chopper flight path length. (d_2) Chopper-to-sample flight path length. (d_3) Sample-to-detector flight path length. (B_1) and (B_2) Beam scrapers phased to eliminate frame overlap problems.

energy is fixed) spectrometer, the neutron's incident energy is determined using a curved slit Fermi chopper; the final energy is determined from the time it takes the neutron to reach the detector.

To understand how LRMECS works, refer to Figure 2. A pulse of neutrons emerges from the moderator and spreads out as it moves down the beam line. This spreading occurs because the neutrons that are faster than average move toward the front of the pulse and the slower neutrons are left in the rear. The pulse then encounters the chopper which, acting like a camera shutter, is "open" for a short time interval during which neutrons at a certain position in the pulse (corresponding to a particular energy) are allowed through. Thus the energy of the neutrons incident on the sample is determined by phasing the chopper with the source.

The energy of a neutron that traverses a distance d in time interval t is given by

$$E = \frac{md^2}{2t^2} \tag{21}$$

and its wavevector is

$$k = \frac{md}{\hbar t} \quad , \tag{22}$$

For each neutron detected, we must be able to determine 1) t_1, the time it took the neutron to traverse the moderator-to-chopper distance, 2) the time the neutron

arrives at the detector, and 3) the angle through which the neutron was scattered. From these quantities and Equations (21) and (22), we can determine 1) the neutron's incident energy, 2) the neutron's final energy, 3) the neutron's incident momentum, 4) the neutron's final momentum, 5) the energy transfer, and 6) the momentum transfer. From these quantities and Equation (11), we can determine the initial momentum of the helium atom. The techniques used to determine these quantities will be discussed in the next chapter.

A time-of-flight diffractometer works in a similar manner to the spectrometer discussed above but requires only one determination of the neutron's energy. Imagine that the chopper has been removed from the spectrometer in Figure 2 (a useful picture since we made a diffractometer out of LRMECS by removing the chopper). A neutron pulse leaves the moderator and, as it zips down the beam line, the pulse once again broadens with the higher energy (shorter wavelength) neutrons at the front of the pulse and the lower energy (longer wavelength) neutrons at the rear. These neutrons are diffracted from the sample and the time they arrive at the detectors, a distance d_3 from the sample, is recorded. If a neutron travels the moderator-to-sample-to-detector distance $d = d_1 + d_2 + d_3$ in time interval t, its wavelength is

$$\lambda = \frac{ht}{md} \ . \qquad (23)$$

If the detector is positioned at a scattering angle, ϕ, a diffraction peak will occur if the Bragg condition

$$2a \sin(\phi/2) = n\lambda \qquad (24)$$

is satisfied. This analysis assumes that all neutrons are elastically scattered; if a neutron is inelastically scattered, it will be part of the thermal diffuse scattered background and can be subtracted out (see pages 293-295 of Reference 33).

There are two great advantages in using time-of-flight techniques: 1) data can be collected at many angles simultaneously, and 2) one can detect and analyze the entire spectrum of neutrons scattered by the sample. This is in contrast to a triple-axis-spectrometer for which 1) data are collected at only one scattering angle at any time, and 2) data are collected for only one value of the momentum transfer at any time. The first of these advantages is important because it allows one to collect data at several different momentum transfers simultaneously. In this experiment, data were simultaneously collected at eight scattering angles. The second advantage means that one analyzes the entire spectrum of neutrons that are scattered through a given angle. These advantages mean that the data collection rates at a pulsed source are typically higher than at a steady state source.

One of the advantages of a triple axis spectrometer is the ability to collect inelastic scattering data using a constant-$\vec{Q}$ geometry.[35] For a constant-$\vec{Q}$ scan, Equation (18) can be fit to the peak profile and $n(\vec{p})$ extracted. Since our data were collected with the scattering angle fixed, more data reduction must be done before $n(\vec{p})$ can be extracted. This arises from the fact that for data collected at constant scattering angle, both E and $\vec{Q}$ vary across the width of the peak. We denote the dynamic structure factor for constant angle scattering $S(\phi,E)$.

To understand the relationship between $S(\phi,E)$ and $S(\vec{Q},E)$ refer to Figure 3. This figure illustrates the relationship between the fractional energy transfer E/E_i, and the fractional momentum transfer, Q/k_i. Note that each solid line represents the energy transfer versus momentum transfer for a detector situated at a scattering angle ϕ. The scattering angles represented in the figure vary from 0° to 120° in steps of 10°. Our data were taken at scattering angles from 47.7° to 115.5°. Each such curve can be pictured as having a finite width since each detector group will subtend a finite angle when viewed from the center of the sample (our detector groups had an angular width of 4.66° in the scattering plane and 10.47° perpendicular to the scattering plane). In our data analysis, the finite size of the detector groups has been included in the calculation of the spectrometer resolution.

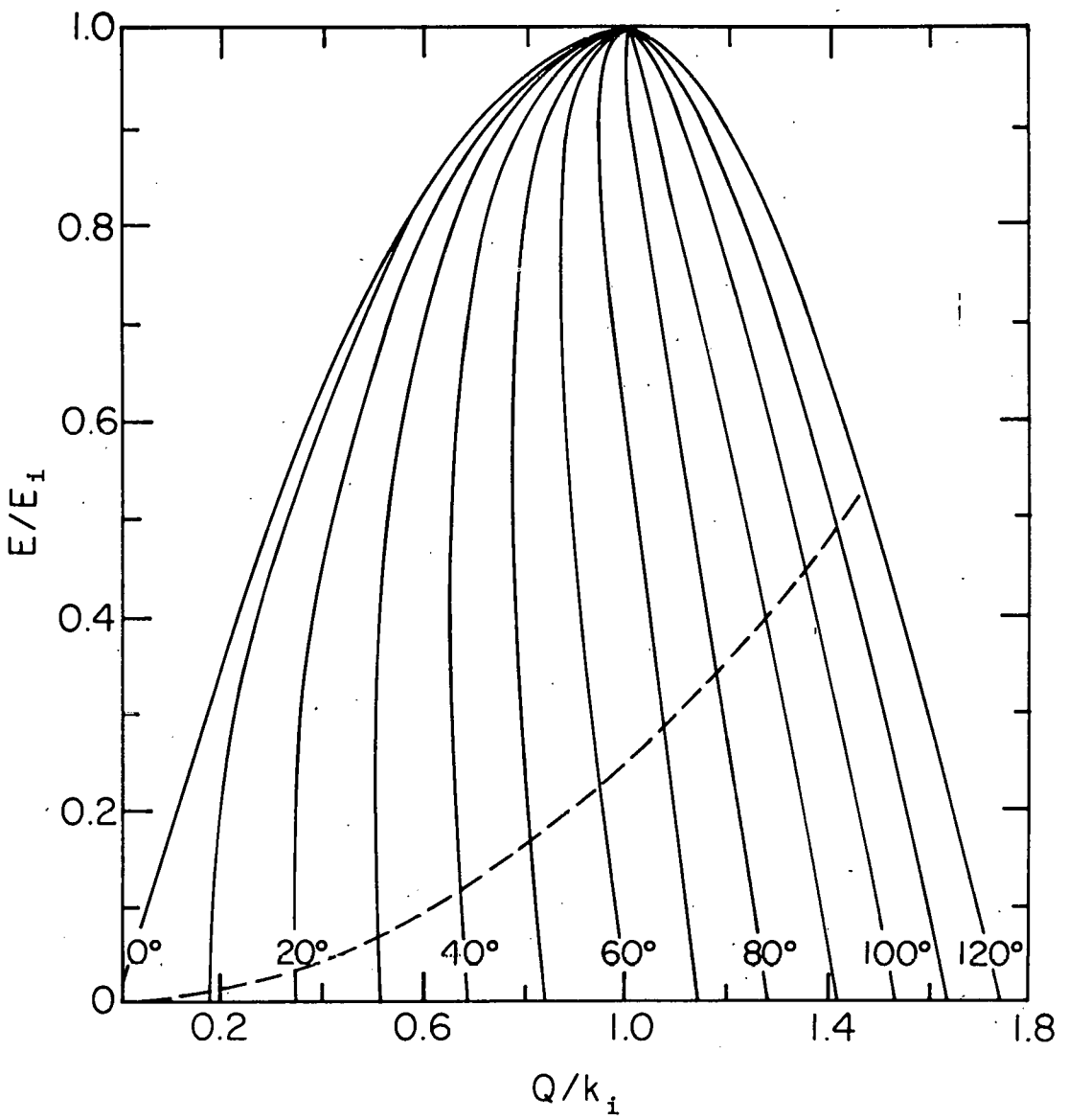

Figure 3. Fractional energy transfer versus fractional momentum transfer for data collected by detectors fixed at scattering angles varying from 0° to 120°. E is the energy transfer and E_i is the neutron's incident energy. Q is the momentum transfer and k_i is the neutron's incident momentum. The dashed curve is a plot of the E versus Q relationship for neutrons scattered from free ^{4}He atoms.

The dashed curve in Figure 3 represents the expected relationship between E and Q if the impulse approximation is strictly obeyed, that is, the relationship expressed in Equation (17). One can envision the dynamic structure factor in three dimensions as a ridge whose peak follows the dashed curve at momentum transfers sufficiently high that the impulse approximation is valid. At lower momentum transfer, there is more structure which consists of multi-phonon peaks, single phonon peaks, and peaks arising from the creation and annihilation of other excitations. With this picture in mind, $S(\vec{Q},E)$ is just the profile of this ridge sliced by a plane perpendicular to the Q/k_i axis (on which Q is constant). $S(\phi,E)$ is the profile of this ridge sliced by a plane that follows the corresponding constant angle curve. Thus a scheme must be found that relates the scattering data collected at constant angle to the required constant-Q profiles.

A computer program, "INTERP"[36], exists on the IPNS-1 VAX11/780 system that accomplishes this transformation. This program stores all the $S(\phi,E)$ profiles and interpolates peak profiles at constant $\vec{Q}$, i.e. $S(\vec{Q},E)$. This analysis has been carried out for our data and the results are presented in Chapter 5.

Another method exists to extract constant-$\vec{Q}$ information from constant-ϕ data. If the fixed angle scattering function, $S(\phi,E)$, is Gaussian, then $S(\vec{Q},E)$ is also Gaussian with a variance, σ_Q^2, given by

$$\sigma_Q^2 = (1 - C_\phi)^2 \, \sigma_\phi^2 \tag{25}$$

where

$$C_\phi = \frac{m}{M} \left[\frac{k_i}{k_f} \cos \phi - 1\right] \tag{26}$$

and Q is the average momentum transfer observed at the scattering angle ϕ. Equations (25) and (26) were derived by D. L. Price.[37]

C. Impulse Approximation

A complication to the impulse approximation arises because the initial and final states of the ^{4}He atom are modified by the presence of the crystal potential. In the impulse approximation one assumes that the scattering atoms may be treated as free rather than bound. The binding is included only in that it produces a spread in the initial momenta. The validity of the impulse approximation has been thoroughly investigated for the case of electron momentum density measurements by Compton scattering in the interactering electron gas[38] and in hydrogenic electron states.[39] Eisenberger and Platzman have extended their rigorous calculation for the Compton profile for hydrogenic electron states to the two electrons in a helium atom.[40] The experimental results one finds using the impulse approximation agree very well with the calculated electron momentum density. They conclude that the impulse approximation is very accurate for weakly bound electrons

and that the first correction term is proportional to $(E_B/E_R)^2$ where E_B is the electron binding energy and E_R is the energy transfer to the electron. If we draw an analogy between our experiment and Compton scattering, we can take the vacancy formation energy as a measure of the binding energy of the helium atom. Since the vacancy formation energy for our stample is about 1 meV,[41] recoil energies in the range 100 meV and above would make the correction negligible.

Since the recoiling ^{4}He atom suffers interactions in its final state, Hohenberg and Platzman[31] suggested treating it as a quasiparticle and replacing the energy-momentum conservation delta function with a Lorentzian. The dynamic structure factor is then

$$S(\vec{Q},E) = \int n(\vec{p}) \frac{d^3p}{(E - \frac{\hbar^2Q^2}{2M} - \frac{\hbar^2\vec{Q}\cdot\vec{p}}{M})^2 + (\text{Im } \varepsilon_k)^2} \quad (27)$$

where

$$\text{Im } \varepsilon_k = \frac{\hbar\sqrt{E}}{M} \rho \sigma_{He}(E) \quad (28)$$

is the inverse of the quasiparticle lifetime. Here ρ is the ^{4}He density and σ_{He} is the ^{4}He - ^{4}He scattering cross section. Since $\sigma_{He}(E)$ is approximately constant for E between 100 meV and 100 eV, the width of this Lorentzian intrinsic resolution caused by the final state interactions is thus proportional to Q for all the sets of data, as also for the entire higher range of E experimentally accessible.

The width of the Gaussian profile that we are measuring in this experiment is also proportional to Q (see Equation (19)). Rodriguez et al.[42] have evaluated the final state interactions for liquid ^{4}He using a Lennard-Jones potential for the interactions as an intrinsic resolution.

$$S(\vec{Q},E) = \int n(\vec{p})\ R(\vec{Q},E - \frac{\hbar^2 Q^2}{2M} - \frac{\hbar^2 \vec{Q}\cdot\vec{p}}{M}) d^3p \qquad (29)$$

and find that the resolution, $R(\vec{Q},E)$, is narrower than what would be given by the Lorentzian of Equation (27). Also, though the resolution obtained has some structure, it would be better approximated by a Gaussian than a Lorentzian. This is important because a Gaussian intrinsic resolution gives a much smaller broadening when convoluted with a Gaussian momentum density than a Lorentzian resolution. Using the results reported by Rodriguez, we calculate that such a correlation leads to a decrease in our value for A of 1%. We therefore feel that we can neglect final state corrections.

There is one potential problem in depending on the impulse approximation. Weinstein and Negele recently reported the results of a calculation, using time-ordered perturbation theory, of the relation between the dynamic structure factor and the momentum density of a system.[43] They find that the relation is as given in Equation (12) for systems interacting via smooth two-body potentials. However, for an interaction potential with a strong

short-range repulsive core, things are not so simple. They present the results for a hard-sphere Bose gas and conclude that final state interactions remain significant even at arbitrarily large momentum transfer. They find that correct scaling properties of the data (Equation (19)), the shift in the peak location (Equation (17)), and the symmetry of the peaks (Equation (18)) cannot be taken as conclusive evidence for the validity of the impulse approximation. Their paper includes a graph that shows a rather distressing difference between the measured structure factor at infinite momentum transfer and the structure factor obtained from the impulse approximation. But this graph shows only the lowest portion of the tails of the structure factor (about two orders of magnitude below the top of the peak). The thesis from which this paper was extracted[44] contains a plot of almost all of the peak. At the peak half maximum, there seems to be no difference between the large momentum peak and the peak given by the impulse approximation. So if one is only interested in the width of the peak measured by σ_Q, one should be safe in extracting this from data taken at sufficiently high momentum transfer. Weinstein and Negele state that the dimensionless parameter $Q\sigma_L$ (Q is the momentum transfer, σ_L is the hard-core diameter of the interaction potential) is a useful parameter to determine if the high-momentum limit has been reached. They state that the infinite

momentum limit is essentially reached when $Q\sigma_L = 45$. Since our data extend up to $Q\sigma_L = 58$, we have at least reached that limit. But how can we know that our data analysis is valid since it depends on the impulse approximation? The best test would be to measure the momentum density of something that can be calculated, possibly as a function of temperature, and see if the impulse approximation gives the calculated value. This is essentially what was done in analyzing the resolution function by measuring the scattering from vanadium. This measurement will be described in Chapter 3.

Equation (18) was derived from only two assumptions: 1) the momentum density is Gaussian, and 2) the impulse approximation is strictly valid. Any deviation of the measured $S(\vec{Q},E)$ from Gaussian line shape would be due to one or both of these assumptions being inaccurate.

Concerning the first assumption, most of the theories written to describe solid helium find that a Gaussian single-particle wave function of the form suggested by Nosanow[8] (Equation (2)) gives the best results. P. A. Whitlock has been kind enough to provide us with the results of a calculation of $n(\vec{p})$ carried out on fcc ^{4}He with a Lennard-Jones potential and a molar volume of 19.12 cm^3/mole.[27] This calculation indicates that $n(\vec{p})$ is very nearly Gaussian over the top 99% of the curve. Below this, there is a very interesting deviation from

Gaussian behavior. Unfortunately, it is in the extreme tails of the $n(\vec{p})$ function that the impulse approximation apparently breaks down according to Weinstein and Negele.[43] So the momentum density is apparently Gaussian, at least to the accuracy we can observe in this experiment.

3. EXPERIMENTAL TECHNIQUES

The experimental apparatus can be quite naturally divided into two parts: A) the cryostat system (Figure 4) and B) the spectrometer system (Figure 2). The cryostat was constructed and tested in Urbana then shipped to the neutron scattering facility at Argonne National Lab. The Low Resolution Medium Energy Chopper Spectrometer[34] (LRMECS) is one of the neutron scattering instruments at Argonne's Intense Pulsed Neutron Source (IPNS-1). The operation of a chopper spectrometer at a pulsed source was explained in Chapter 2; the practical details will be discussed below.

A. Cryostat System

The cryostat system is divided into four subsystems: 1) the helium and nitrogen reservoirs, 2) the refrigeration system, 3) the temperature control and measurement system, and 4) the sample cell and high pressure system.

A schematic diagram of the cryostat constructed for this experiment is shown in Figure 4; it uses the liquid nitrogen and liquid helium reservoirs from the cryostat described by D. S. Kupperman.[45] A 5.0 liter liquid helium dewar surrounded by a 12.0 liter liquid nitrogen reservoir, purchased from the Superior Air Products Co.,

Figure 4. A cross-sectional view of the cryostat used in the present work: (a) 5.0 liter liquid helium reservoir. (b) 12.0 liter nitrogen reservoir. (c) Aluminum support plate. (d) Perforated stainless steel cylinder supporting the lower nitrogen reservoir. (e) 8.0 liter liquid nitrogen reservoir. (f) Epoxy-fiberglas double cylinder connecting the lower nitrogen reservoir to the liquid helium reservoir in a fixed tail configuration. (g) Stainless steel bellows to relieve tension caused by contraction of the helium reservoir. (h) Support braces to support weight of 4 K flange. (i) Nylon pot-sample cell support posts. (j) Pot. (k) Aluminum sample cell. (l) Liquid helium temperature radiation tail (aluminum). (m) Aluminum sample cell support post. (n) Liquid nitrogen temperature radiation tail (aluminum). (o) Room temperature hat (an integral part of the spectrometer).

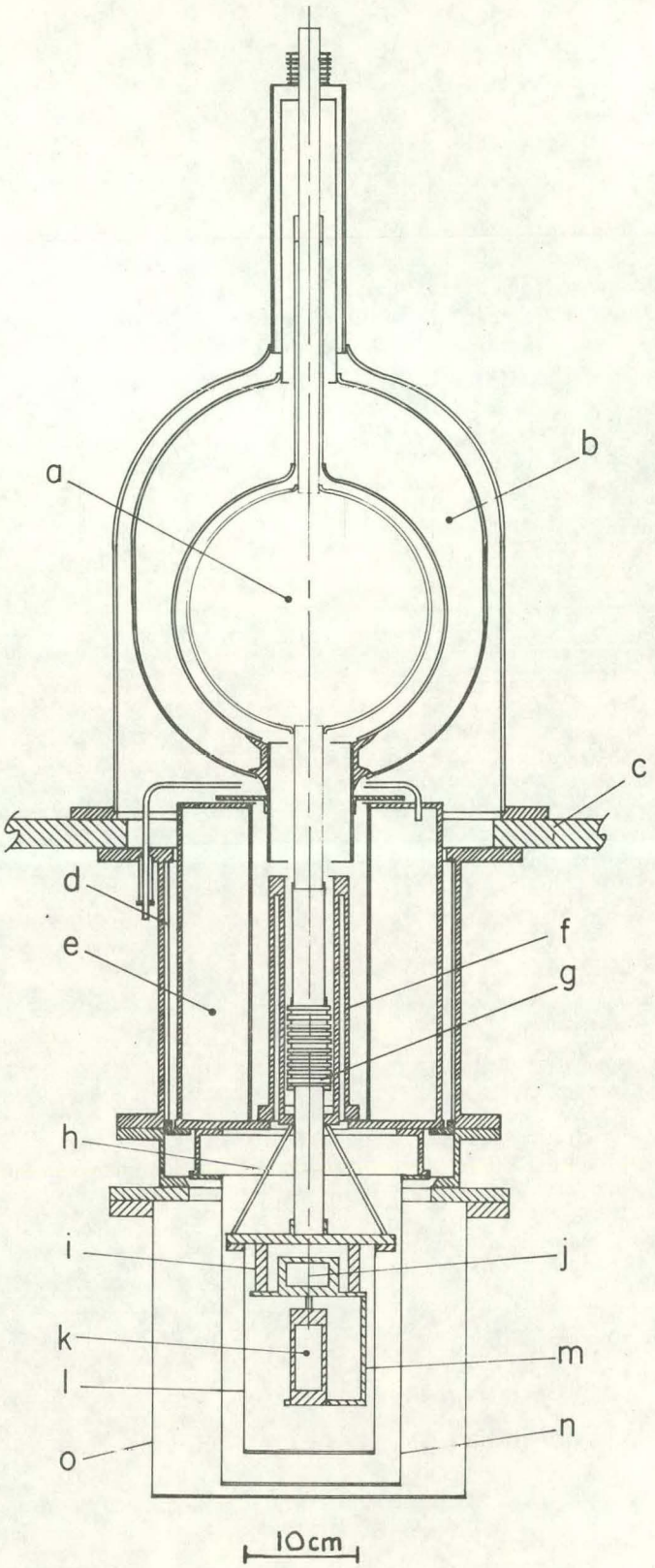
a
b
c
d
e
f
g
h
i
j
k
l
m
n
o
10cm

was modified by the addition of a 8.0 liter liquid nitrogen dewar surrounding a rigid tail assembly. The refrigeration system consists of a continuously fed ^{4}He pot similar to that described by DeLong et al.[46] The pumped pot was capable of maintaining the sample cell at 1.7 K indefinitely. The sample cell was supported by a copper support on top and an aluminum support on the bottom; both supports were bolted rigidly to the pot. A liquid helium temperature shield and a liquid nitrogen temperature shield, both made of type 6061 aluminum, surround the sample cell/pot assembly. The room temperature tail that surrounds the nitrogen temperature tail is an integral part of the neutron spectrometer. A brass outer tail was used while the cryostat was being constructed and tested in Urbana.

Because the temperature was never to go below 1.50 K, standard direct current techniques were sufficient for temperature measurement. Two germanium thermometers, model GR-200B-500 manufactured by Lake Shore Cryotronics, were connected in four terminal configuration to a Kelvin bridge. One of the germanium thermometers was calibrated by the manufacturer to the Provisional Temperature Scale of 1976 (EPT-76). The second thermometer was calibrated by comparing it with the first using the temperature measurement bridge constructed for this experiment.

The temperature measurement bridge consisted of a current supply, a potentiometer, a standard resistor, and

a null detector. Current to the thermometer is supplied by a dc current supply which is adjustable to nine discrete currents in the range 1 μA to 1 mA. The current one uses is determined by the thermometer manufacturer's recommendations, and varies with the temperature of the thermometer. The thermometer is in series with a Leeds and Northrop type 4030-B 100 ohm standard resistor and the voltage drop across the thermometer is compared to the voltage drop across the standard resistor with a Honeywell Model 3781 potentiometer, the bridge balance condition being determined using a Keithley model 155 null detector.

The temperature control system was constructed using the design of Lazarus and Seward.[47] In this circuit, a 47 ohm Allen-Bradley carbon composition resistor, made especially for thermometry, forms one arm of an AC bridge. The lead resistance of the thermometer is canceled by use of a balanced three wire connection from the bridge to the sensor. The bridge is driven at 25 Hz and the error signal is amplified, fed into a phase sensitive detector (along with a reference signal) and an overall negative feedback signal results that is applied to a Manganin wire heater wrapped around the sample cell support. The temperature controller is capable of keeping the temperature constant to better than 1 mdeg for several days, if the controller is kept in an electrically quiet environment. The electrical system associated with the

proton accelerator and switching system at IPNS-1 produced so much electrical noise that the temperature control system never operated optimally. Consequently, the controller was used during data collection on the liquid sample (at 4.00 K) but was not used during the data collection on the two solid samples (both at 1.70 K). Even without electronic temperature control the temperature remained constant within ± 10 mdeg, the quoted uncertainty in our temperature.

The high pressure ^{4}He needed to grow the samples was provided by a cylinder of ultra-pure ^{4}He from Union Carbide.[48] The pressure of the gas in the sample fill line was measured by a Heise CMM-269 (0-2000 psia) gauge which is certified to an accuracy of ± 2 psi. The calibration of the gauge was checked with a type 2750 dead-weight tester manufactured by Barnet Instruments. The high pressure tubing outside the cryostat is 0.16 cm o.d X 0.07 cm i.d. stainless steel, inside the cryostat it is 0.08 cm o.d. X 0.04 cm i.d. cupronickel. The last 7 cm of the sample fill line, where the fill line enters the sample cell, was of 0.04 cm o.d. X 0.025 cm i.d. cupronickel; this assures that once solid helium is grown to plug the fill line, it will not slip.

The sample cell is cylindrical and was constructed from type 6061 aluminum. The external dimensions are 3.2 cm diameter by 8.4 cm long, the sample volume being

2.7 cm diameter by 5.7 cm long. The sample cell and radiation tails are made of aluminum because it has such a small neutron scattering cross-section and such a large thermal conductivity. Stainless steel sample cells have been used when a single crystal was desired; the low thermal conductivity of stainless steel makes it easier to maintain a thermal gradient across the cell which promotes single crystal growth. Because the theories calculate an isotropic momentum density for solid helium, we wanted to measure the momentum density averaged over all crystal directions. We chose an aluminum sample cell because its high thermal conductivity promotes the growth of a powder sample.

The sample cell was filled by pressurizing the cell with ultra-high purity helium gas and allowing the gas to condense as the sample cell cooled (the cell warmed from about 4 K to about 8 K when it was pressurized). Prior to growing the first solid sample, the cell was pressurized to 5.97 MPa (866 psi) at 4 K; it was allowed to cool while its temperature and pressure were monitored. The sample reached the solid-liquid phase boundary at about 5.72 MPa and 2.50 K. As the sample cooled, the pressure dropped in such a way as to follow the phase boundary until the sample solidified. The solidification of the sample was signaled by a sudden drop in the temperature at essentially constant pressure, that is, the

sample deviated from the liquid-solid phase boundary. The temperature was then stabilized just below the melting temperature and the pressure of the solid was determined. Since the fill line heater was still on, no solid had grown in the fill line and the pressure of the sample was equal to the externally measured pressure. A similar procedure was followed in growing the second solid sample.

The molar volume of the sample can be most accurately determined, with our apparatus, from the pressure at which the solid forms. Because the phase boundary in this region is well known,[10] we can determine the molar volume and its uncertainty from the melting pressure and its uncertainty.

B. The Spectrometer System

The IPNS-1 neutron source is a pulsed proton spallation system that uses the buildings, control electronics, and accelerator system that were built for the Zero Gradient Synchrotron (ZGS) that was decommissioned in 1981 (the electronics and accelerators were rebuilt and augmented). Spallation (from the verb spall meaning to splinter or chip) is a process in which neutrons are produced when high energy protons are incident on a heavy metal target (Ta, W, Pb, and U have been used); the protons rip through the target nuclei leaving behind a trail of particles (including neutrons) and excited nuclei. When 400 MeV protons are incident on a uranium target,

each proton produces about 8.5 neutrons having a broad energy spectrum that covers the energy range from millivolts up to the energy of the incident proton.

The proton accelerator system originally served as an injector of the ZGS. It consists of a source of negatively charged hydrogen ions, a 750 keV Cockcroft-Walton preaccelerator, a 50 MeV linac, and a 500 MeV Rapid Cycling Synchrotron; the synchrotron was providing 400 MeV protons at the time this experiment was performed. Negatively charged hydrogen ions are injected into the synchrotron where the two electrons are removed by a foil stripper. Injecting hydrogen ions allows one to overcome space charge and beam focusing problems that limit the beam current. At the proper time, 10 μsec long proton pulses are extracted, steered down a beam line, and directed to a Zircaloy-clad uranium target. There are actually two targets: 1) a radiation effects target whose moderators and reflectors allow high energy neutrons to be incident on the sample and 2) a neutron scattering target whose moderators provide neutrons at energies appropriate for diffraction and spectroscopic experiments on condensed matter. A switching magnet determines which target the proton beam is incident upon. The proton accelerator system is operated and maintained by C. W. Potts and the Accelerator Operations Group.

During this experiment, the average proton current on the target was 8.16 μA at 30 Hz. The liquid hydrogen

and liquid methane moderators were not yet in place so a polyethelene moderator was used during this experiment. The neutron pulses drift down the 7.5 meter beam line and are collimated by a 5 cm wide by 10 cm tall rectangular hole in a piece of borated polyethelene shielding just in front of the chopper (refer to Figure 2 for references to different parts of the spectrometer). The neutrons of the correct energy pass through a curved slit in the chopper, the curvature of which was chosen to maximize the transmission of 500 meV neutrons when the chopper is spinning at its designed speed of 270 Hz. After the chopper, the beam is further reduced to 5 cm by 5 cm by 0.64 cm thick Boral mask just inside the room temperature hat in front of the sample.

The energy of the neutrons incident on the sample is determined by phasing the chopper with respect to the source. It is a very difficult problem to get a chopper properly phased to a spallation source. The problem was solved by allowing the chopper to determine when the extraction magnet takes a pulse of protons from the synchrotron. The electronics that sense the phase of the chopper and send the extraction command to the magnet were maintained by G. E. Ostrowski. These electronics determine the nominal energy of the neutrons incident on the sample; the actual value of the neutron's energy is determined from the data collected by beam monitors M2 and M3. The

beam monitors are low efficiency ^{3}He filled detectors placed in the beam path to monitor the flux and energy of the neutrons. The data collected by M2 and M3 are the number of neutrons detected versus flight time and consist of one peak in each monitor. The difference between the flight times given by the centers of these peaks is the time it took a neutron of average energy to traverse the distance between the two monitors. Knowing the distance between the monitors, one can calculate the neutron's kinetic energy. For this experiment, the incident neutrons had a kinetic energy of 505. meV. The beam monitors also measure the total number of neutrons incident on the sample. In the analysis of the data, one must normalize the empty cell data to the sample data so that these data sets correspond to the same number of incident neutrons and can then be properly subtracted. This normalization is carried out by simply multiplying the empty cell data by the ratio of the monitor counts from the sample and empty cell data sets.

There are 142 detectors positioned in an arc 2.5 meters from the sample covering the scattering angles -10° and 120°. The detectors have a diameter of 2.5 cm and have lengths of 11.25 cm, 22.5 cm and 45 cm with the shorter ones at the smaller scattering angles. The detectors are filled with 6 atmospheres of ^{3}He and work by detecting the proton that is emitted with a ^{3}He atom

absorbs a neutron. The neutron absorption cross-section for ^{3}He is 2500 barns for 100 meV neutrons.

We found that for scattering angles smaller than 47.7° the helium data peak is not unambiguously resolved from the aluminum cell peak, we therefore only evaluate the data collected by detectors at mean scattering angles greater than 47.7°. There are eight detector groups each containing eight detectors at mean scattering angles from 47.7° to 115.5°. Table 1 contains a list of calculated parameters that characterize the scattering for the eight detector groups. The first column gives the scattering angle of the center of each detector group. Columns two and three contain the momentum transfer and energy transfer at which the corresponding data peak will be centered if 505 meV neutrons scatter from ^{4}He nuclei obeying the impulse approximation assumptions. Column four contains the factors that relate the width of $S(\phi,E)$ to the width of $S(\vec{Q},E)$ (see Equation (25)). The last column contains the standard deviation of the resolution function of the spectrometer for scattering of 505 meV neutrons from ^{4}He at the given scattering angle.[37]

A rather subtle problem is determining when a neutron pulse leaves the moderator. A pick-up coil senses the arrival of a proton pulse on the spallation target. After a fixed time delay, the clock, which measures the flight time of the neutrons, is started. For this reason,

Table 1. Calculated parameters for the present experiment and spectrometer configuration. The first column contains the scattering angles for the centers of the eight detector groups. The second column contains the values of the momentum transfer at which one expects the corresponding data peaks to be centered. The third column contains the values of the energy transfer one expects the data peaks to be centered about. The next column contains the parameters that relate the widths of $S(\phi,E)$ and $S(\vec{Q},E)$ (see Eqn. (25)). The last column contains the values of the resolution of the spectrometer for this experiment.

ϕ (deg)	$\bar{Q}$ ($\AA^{-1}$)	$\bar{E}_r$ (meV)	$1-C_\phi$	σ_R (meV)
47.7	12.18	77.4	1.068	16.12
57.3	14.22	105.6	1.099	14.98
66.9	16.08	135.0	1.136	14.04
77.7	17.93	167.8	1.186	13.15
87.3	19.37	195.7	1.237	12.43
96.9	20.60	221.5	1.292	11.80
105.9	21.59	243.3	1.348	11.28
115.5	22.48	263.7	1.408	10.82

the raw data (Figures 5 through 28) have an arbitrary t=0 origin. One can determine the effective time at which the neutrons left the moderator from the flight time about which the elastic vanadium data peak is centered in the data collected by the detector at the smallest scattering angle (1.2°). That this is an elastic peak is an excellent assumption.

A final problem one encounters with chopper spectrometers is the problem of "frame overlap." This occurs when the fast neutrons from one pulse overtake the slow neutrons from the previous pulse. One considers the problem of frame overlap when choosing the frequency at which the neutron source will operate. Having chosen the source frequency, one can eliminate frame overlap with beam scrapers (B1 and B2 in Figure 2). The beam scrapers are high-transmissions coarse-resolution choppers that eliminate neutrons with energies that otherwise would contaminate the neutrons that are selected by the chopper. At the time this experiment was performed, beam scrapers had not been installed on LRMECS.

Because the observed data profile is a convolution of the dynamic structure factor and the spectrometer's resolution, an accurate determination of the resolution is essential to the data analysis. The nominal resolution of LRMECS is 5% for energy transfer and 2% for momentum transfer. Referring to Equation (12), one sees that in order

to determine the distribution of the quantity $\vec{p}$ (the helium atom's momentum), we measure a combination of momentum and energy transfer, thus we are interested in how accurately LRMECS can measure the combination of energy and momentum transfer that ultimately gives one the distribution of momentum of the helium atoms, $n(\vec{p})$.

The energy resolution of a chopper spectrometer depends on a number of factors. These include: 1) the time width of the neutron pulse when it is produced, 2) the time interval during which the chopper is "open," 3) the width of the time channels into which the neutron arrival times are sorted, 4) the uncertainty in the incident path length, 5) the uncertainty in the scattered path length. The momentum resolution depends on all the quantities enumerated above plus: 1) the angular divergence of the beam in the scattering plane, 3) the angular divergence of the beam perpendicular to the scattering plane, and 3) the uncertainty in the scattering angle.

Because the contributions to the energy and momentum resolution are dependent on the incident neutron energy, the scattering angle, the sample material, and the sample configuration, calculation of the instrumental resolution requires a fairly lengthy computer calculation. Such a calculation has been done for our experiment by D. L. Price and S. K. Sinha.[37] The resultant resolution function, which is Gaussian as a result of approximations made in the calculation, is given in Table 1.

C. Scattering from Vanadium

Vanadium is an extremely important substance to neutron scattering because its scattering is almost purely incoherent. Other substances (e.g. $Mn_{.42}$-$Co_{.58}$) have been produced that are perfect incoherent scatterers;[49] but vanadium, being less expensive and easier to produce, is more widely used. In a spectroscopic experiment, observing the scattered spectrum from vanadium has two important applications: 1) to normalize the scattering of a sample under study, and 2) to determine the resolution of the spectrometer.

In a neutron diffraction experiment, vanadium has the above two applications plus a third: if the sample is in a container, that container should be made of vanadium. This assures that the scattered spectrum is not complicated with Bragg peaks from the sample cell. Spectroscopic experiments, on the other hand, usually employ aluminum sample cells because the total cross-section is small. In this experiment, the sample cell was made of aluminum because the main purpose was to observe the inelastic scattering spectrum. The aluminum sample cell created problems when we observed the diffraction pattern from the sample; aluminum Bragg peaks conceal most of the helium Bragg peaks. We could nevertheless extract sufficient information from the diffraction measurement.

When one studies the differential scattering cross-section of a system, vanadium is used as a standard scatterer against which the sample can be compared. It can be shown that the coherent cross-section is proportional to the square of the scattering length averaged over the nuclei that compose the scatterer.[30] As it turns out, the weighted scattering lengths of the two spin states of the one naturally occurring vanadium isotope, ^{51}V, are nearly equal and opposite. Consequently, the incoherent cross-section for vanadium is 4.79 barns while its coherent cross-section is 0.019 barns.

Having a near zero coherent cross-section implies the scattering from vanadium is particularly simple. The absence of Bragg peaks means that the angular dependence of the scattering is just that due to the thermal motion of the atoms; that is, the static structure factor is simply the Debye-Waller factor[36]

$$S(\vec{Q}) = c \quad \exp(-2W(Q)). \tag{30}$$

Because vanadium has such a simple structure factor and it serves as a standard scatterer, its scattering function is well known from extensive measurements. The proper way to normalize the scattering from a sample under study is to compare the scattering from the sample to the vanadium elastic peak derived from data taken on the same neutron scattering instrument. In Chapter 5, the scattering from

our sample is normalized to the scattering data taken on vanadium (Equation (31)).

The second important use of vanadium is to determine experimentally the resolution of the spectrometer. One determines the resolution of the spectrometer from the width of the vanadium elastic peak. Even though the scattering is elastic, the peak is broadened by the instrument's resolution. It is important to determine the spectrometer's resolution because the observed structure factor is the convolution of the sample's actual structure factor and the spectrometer's resolution. We must therefore determine the resolution and subtract its effects from the observed data; this will be done in Chapter 5.

The resolution of LRMECS has been calculated for the values of E and Q at the peak centers for each detector group and is reported in Table 1. Note that the calculation of the spectrometer's resolution assumes the scattering is from free atoms with a mass of 4.00 amu. In measuring a spectrometer's resolution, one would then assume that the scattering was elastic (E=0), this is equivalent to assuming that the scatterer (vanadium) had infinite mass. When the widths of the observed vanadium peaks were compared to the convolution of the known vanadium structure factor and the calculated resolution (recalculated with the assumption that the scattering from vanadium was elastic), they did not agree. The resolution

had to be recalculated assuming that the vanadium atoms were free and had a mass of 50.94 amu. Having done this, the observed widths agreed exactly with the resolution/structure factor widths. This implied that 1) the neutrons were interacting with single vanadium atoms, 2) single-atom motion was responsible for the widths of the vanadium peaks and therefore 3) our measurement represents a measurement of the vanadium momentum density. This result was totally unexpected and quite exciting. At the energy and momentum transfer one can attain with LRMECS, we were able to measure the momentum density of vanadium, a metal whose atoms are almost 13 times as massive as helium atoms and whose binding energy is 10^4 times as great. Both the lower mass and lower binding energy make a $n(\vec{p})$ measurement on helium even more practicable.

4. DATA

Ten sets of data were taken, six sets of spectroscopic data and four sets of diffraction data. The spectroscopic data consist of inelastic scattering data on: 1) 19.45 cm^3/mole hcp ^4He, 2) 18.20 cm^3/mole normal liquid ^4He, 3) 18.20 cm^3/mole hcp ^4He, 4) empty sample cell, 5) vanadium foil, and 6) spectrometer background. The diffraction data were taken to search for preferred orientation and determine the extent to which the sample was polycrystalline. For these data sets the diffractometer was made by simply removing the chopper from the spectrometer; computer software was borrowed from one of the IPNS-1 powder diffractometers. The four sets of diffractometer data consist of elastic scattering data on: 1) the same 18.20 cm^3/mole hcp ^4He sample mentioned above, 2) vanadium foil, 3) empty sample cell, and 4) diffractometer background. These data sets are described below.

A. 19.45 cm^3/mole HCP ^4He

The first sample solidified at 5.41±.01 MPa (785±2 psi); this corresponds to a molar volume of 19.45±.01 cm^3/mole.[10] The uncertainty in the molar volume is dominated by the uncertainty in the pressure measurement. The sample solidified and was allowed to

cool to about 1.9 K. At this point a temperature instability, probably associated with superfluid film flow in the pot pumping line, became evident. This instability made temperature control difficult, so the temperature controller was turned off and the sample was allowed to cool to the lowest temperature attainable with the pot system. The temperature oscillated around 1.9 K with a (approximately) sinusoidal time dependence having an amplitude of about 0.2 deg and period of about 500 seconds. Data were taken on this sample for eight hours before the source was shut down for two days. During beam shut-down, the temperature stabilized at 1.7 ± .01 K. The temperature uncertainty is given by how much the temperature drifted during data collection not by the precision with which it could be determined. The data collected before the temperature stabilized were discarded and a new data collection cycle was begun. Data were collected, during 41.8 clock hours, from 4.32 million pulses which, at a rate of 30 pulses per second, is 39.96 hours beam time.

The raw data, neutrons per 2 μsec channel versus time of flight, are displayed in Figures 5 through 12. In these figures, the solid line represents the data collected with the sample cell empty and the circles represent data collected with the sample in the cell. The number of neutrons that are detected at a given angle per two microsecond time interval are plotted along the vertical axis;

the horizontal axis represents the time of flight of the neutron. The most important characteristics of the raw data are discussed below.

B. 18.20 cm^3/mole Liquid ^4He

An eight hour beam shut-down permitted melting of the first sample and changing of the sample density. The goal was to take spectroscopic data on a liquid and a solid sample at the same density to see if the momentum densities differed significantly. The density was chosen for the second sample by considering the pressure to which the sample cell had been tested and the change in sample density necessary to give a statistically significant change in the estimated experimental results.

The 18.20 cm^3/mole normal liquid sample was prepared by repeatedly pressurizing the cold cell with helium gas and allowing the sample to condense. When the sample pressure had reached 11.72 ± 0.03 MPa (1700 ± 5 psi) the temperature was stabilized at 4.000 ± 0.002 K and data were collected during 60.07 clock hours for a measured 41.15 hours beam time. The sample density, 18.20 ± 0.01 cm^3/mole, was determined from the pressure at which the helium solidified when the temperature was lowered to make the next hcp sample. Relatively large variation and hence specified uncertainty in the pressure of the liquid sample was due to lack of environmental temperature control in the experimental area. Secular changes in room

temperature caused pressure changes of several psi in the gas handling system. The cryostat temperature controller was nevertheless able to keep the temperature of the sample stabilized to better than ± .002 deg. The raw data taken on the liquid are shown in Figures 13 through 20.

C. 18.20 cm^3/mole HCP ^4He

To make the last sample, the sample cell was cooled leaving the same amount of helium in the sample cell/fill line system. The sample temperature and pressure followed the liquid-solid phase boundary until a solid was formed at 9.12 ± .01 MPa (1322 ± 2 psi), at which time the temperature dropped rapidly. This melting pressure corresponds to a molar volume of 18.20 ± 0.01 cm^3/mole.[10] The temperature controller once again was turned off and the temperature dropped as low as the pot system would allow. The temperature stabilized at 1.70 K and never drifted more than ± 0.005 deg; there were no oscillations in temperature as occurred when the first sample was grown. Data were taken for 38.50 hours beam time (42.57 clock hours). The eight data sets on the 18.20 cm^3/mole hcp sample are shown in Figures 21 through 28. The characteristics of these data sets, discussed below, are essentially the same as the same-angle data sets for the first two samples.

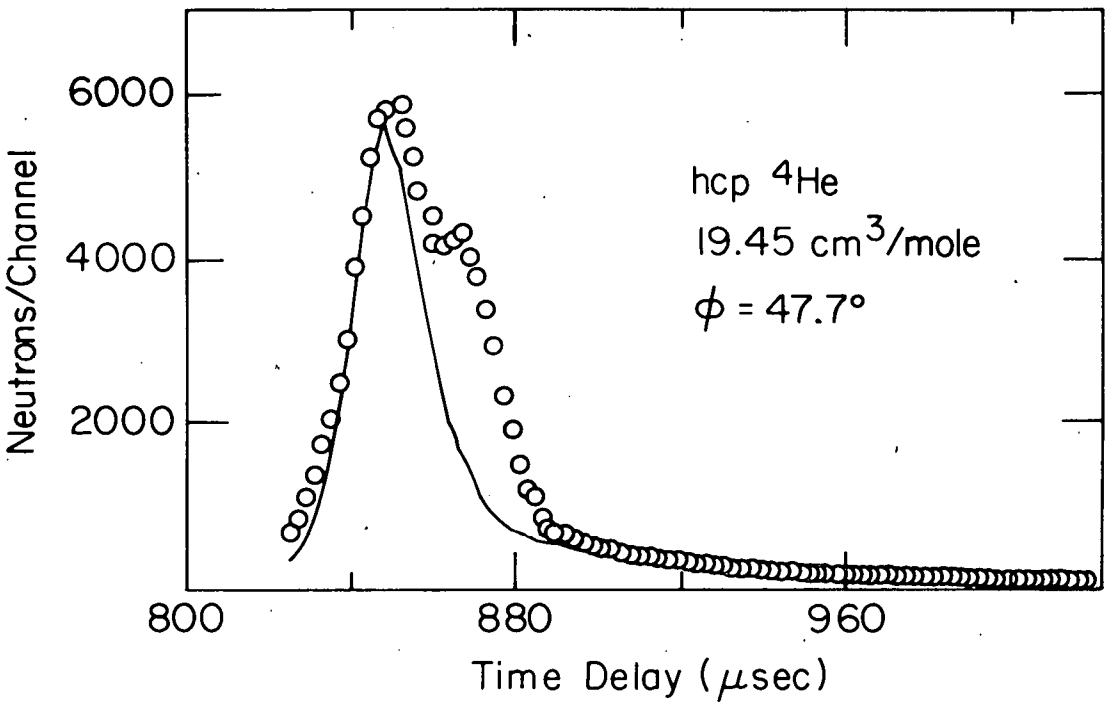

Figure 5. Total number of neutrons detected per 2 μsec channel versus flight time. These raw data were collected on the low density hcp sample by the detector group centered at a scattering angle of 47.7°. The line represents the data collected with the sample cell empty; the points represent the data collected with the helium sample in the cell.

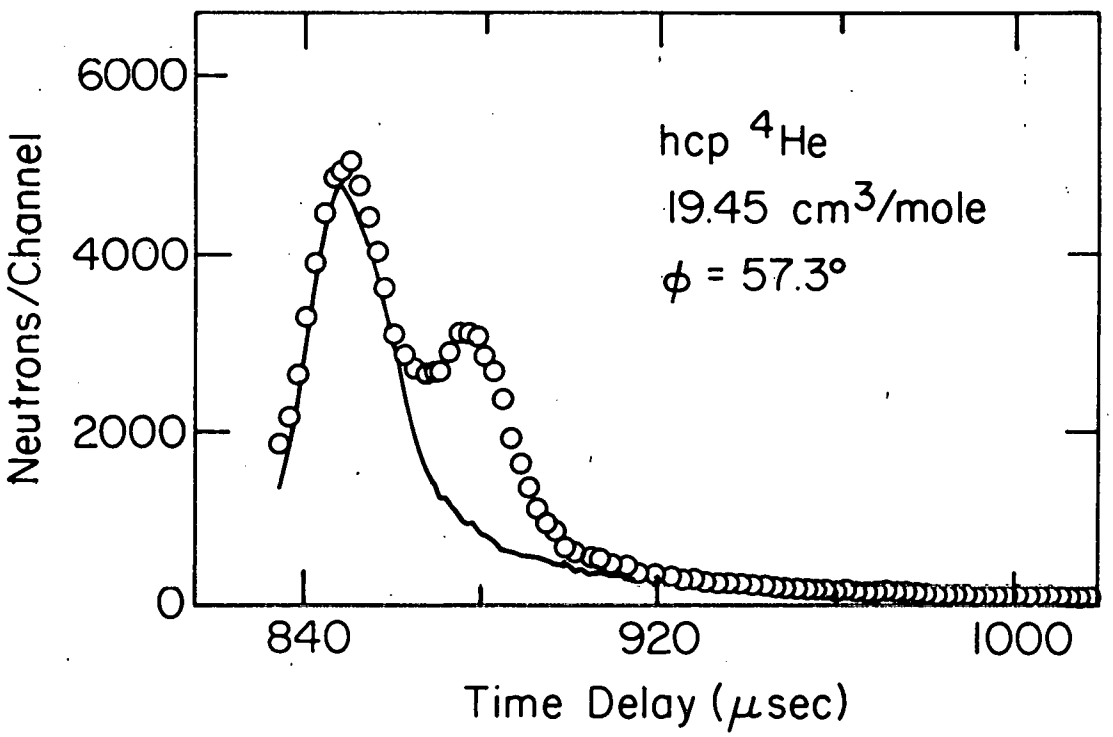

Figure 6. Total number of neutrons detected per 2 μsec channel versus flight time. These raw data were collected on the low density hcp sample by the detector group centered at a scattering angle of 57.3°.

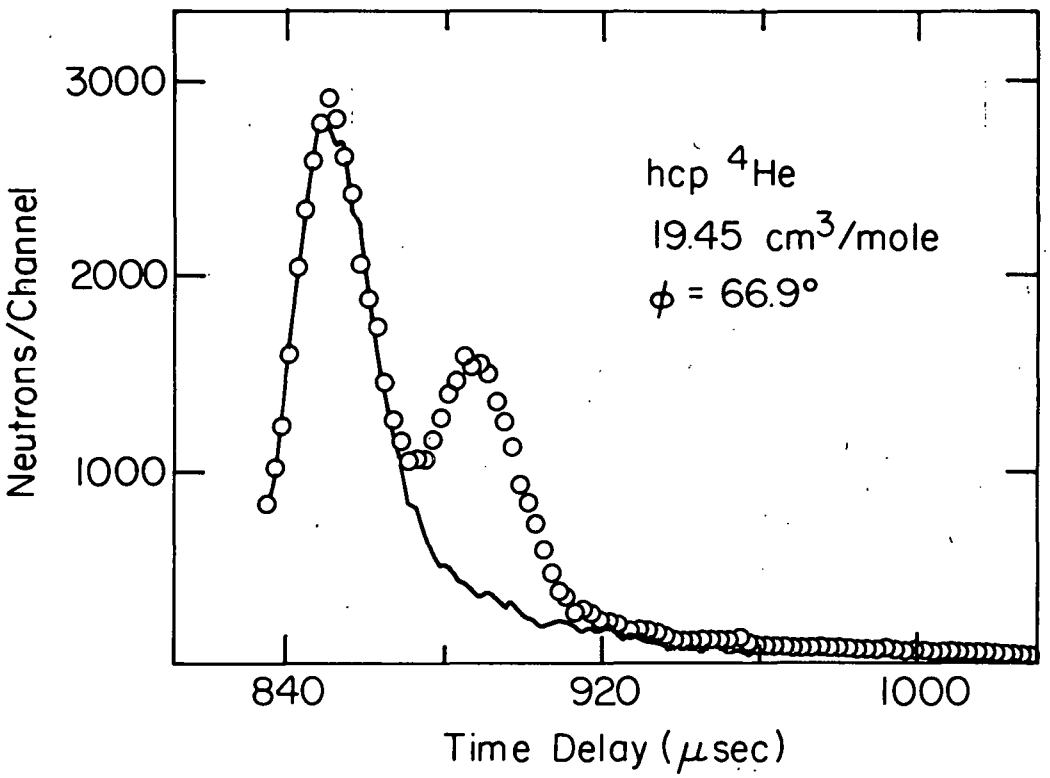

Figure 7. Total number of neutrons detected per 2 μsec channel versus flight time. These raw data were collected on the low density hcp sample by the detector group centered at a scattering angle of 66.9°.

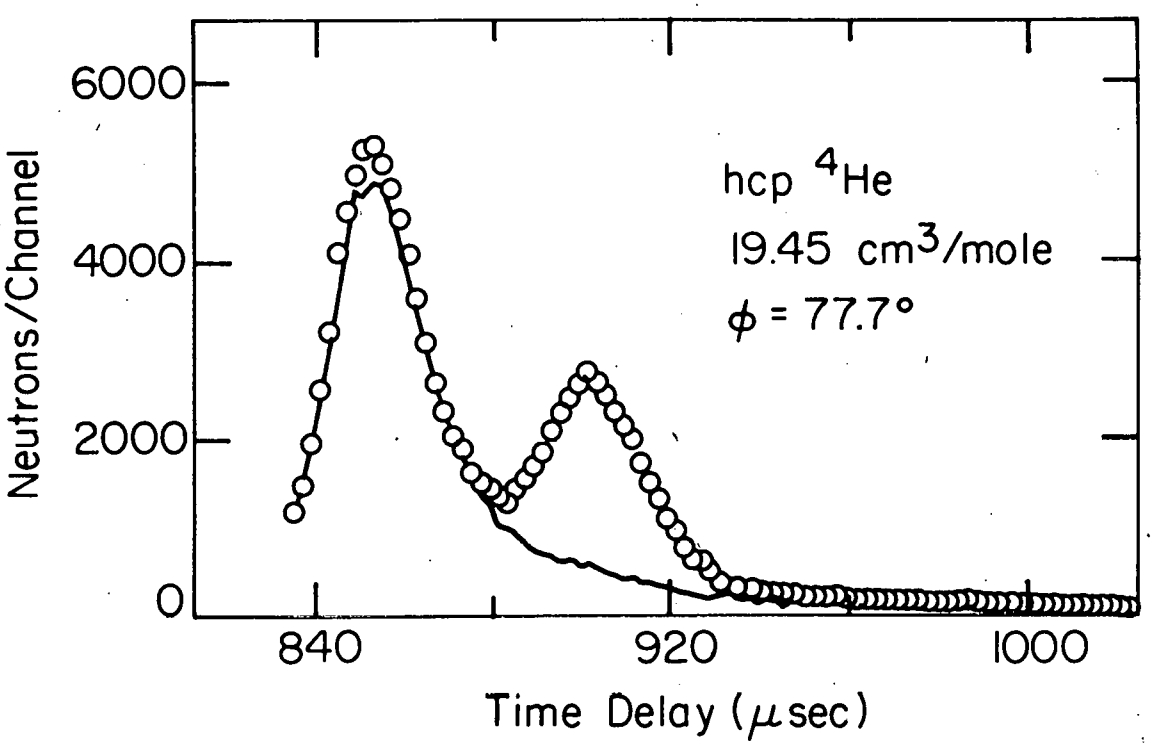

Figure 8. Total number of neutrons detected per 2 μsec channel versus flight time. These raw data were collected on the low density hcp sample by the detector group centered at a scattering angle of 77.7°.

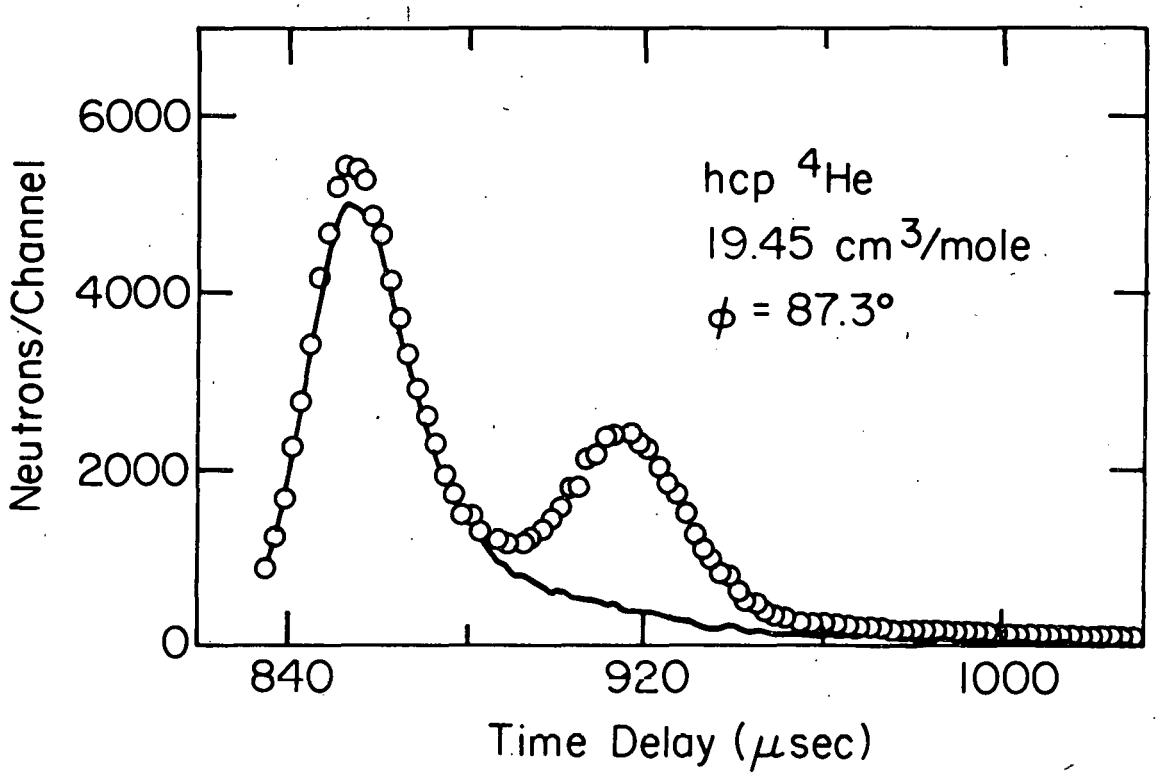

Figure 9. Total number of neutrons detected per 2 μsec channel versus flight time. These raw data were collected on the low density hcp sample by the detector group centered at a scattering angle of 87.3°.

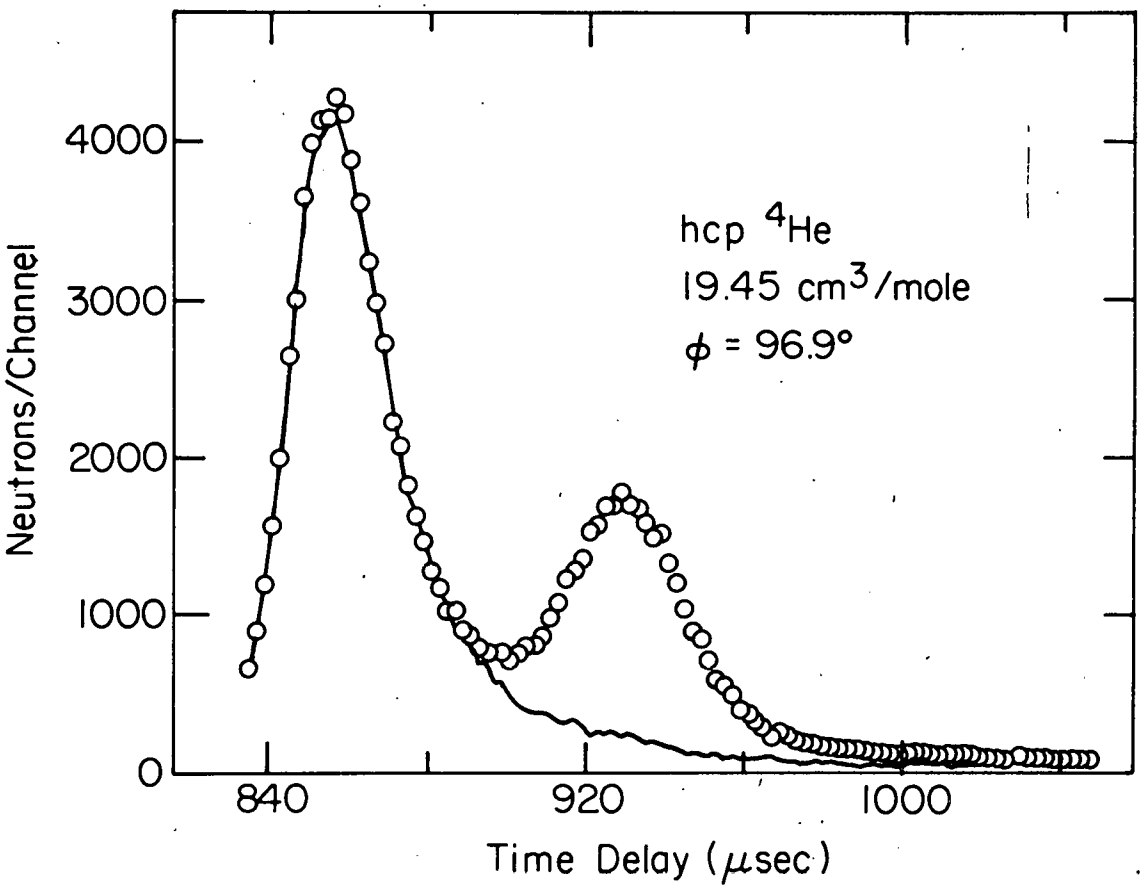

Figure 10. Total number of neutrons detected per 2 μsec channel versus flight time. These raw data were collected on the low density hcp sample by the detector group centered at a scattering angle of 96.9°.

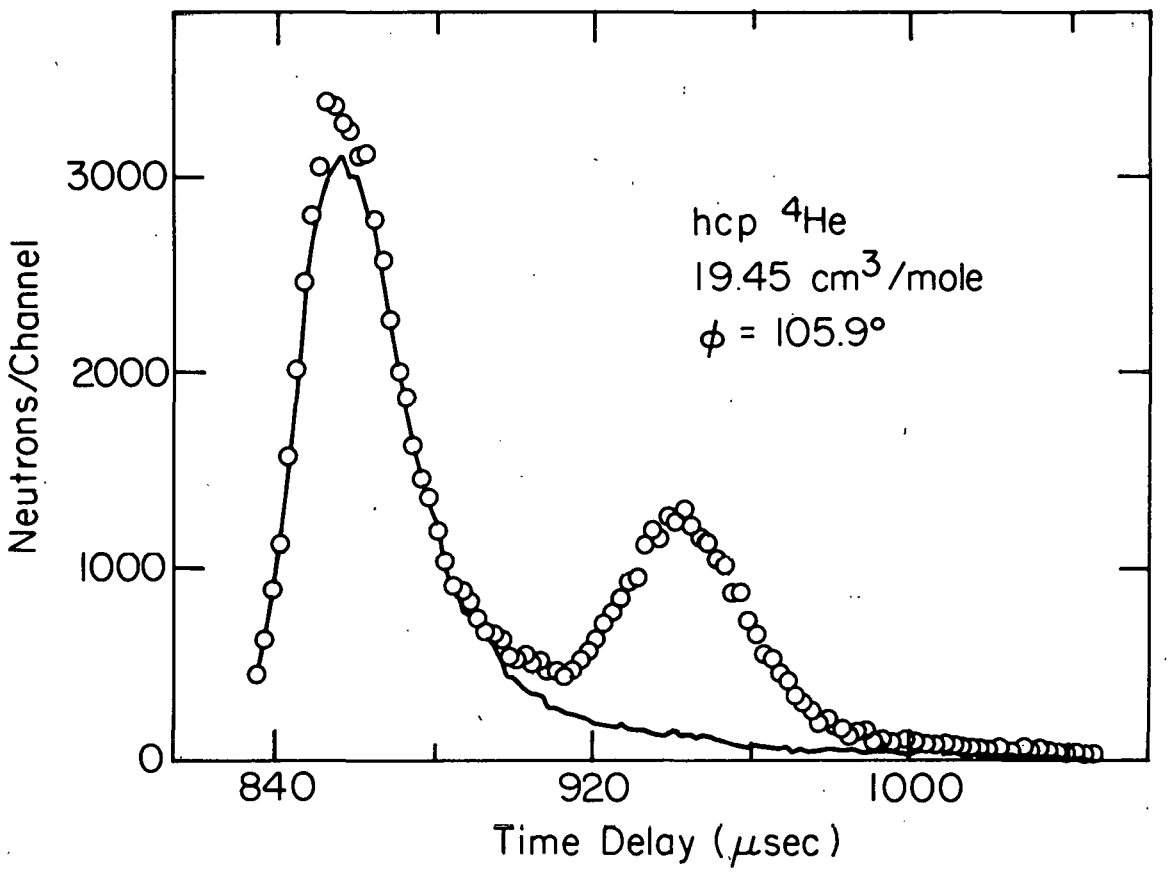

Figure 11. Total number of neutrons detected per 2 μsec channel versus flight time. These raw data were collected on the low density hcp sample by the detector group centered at a scattering angle of 105.9°.

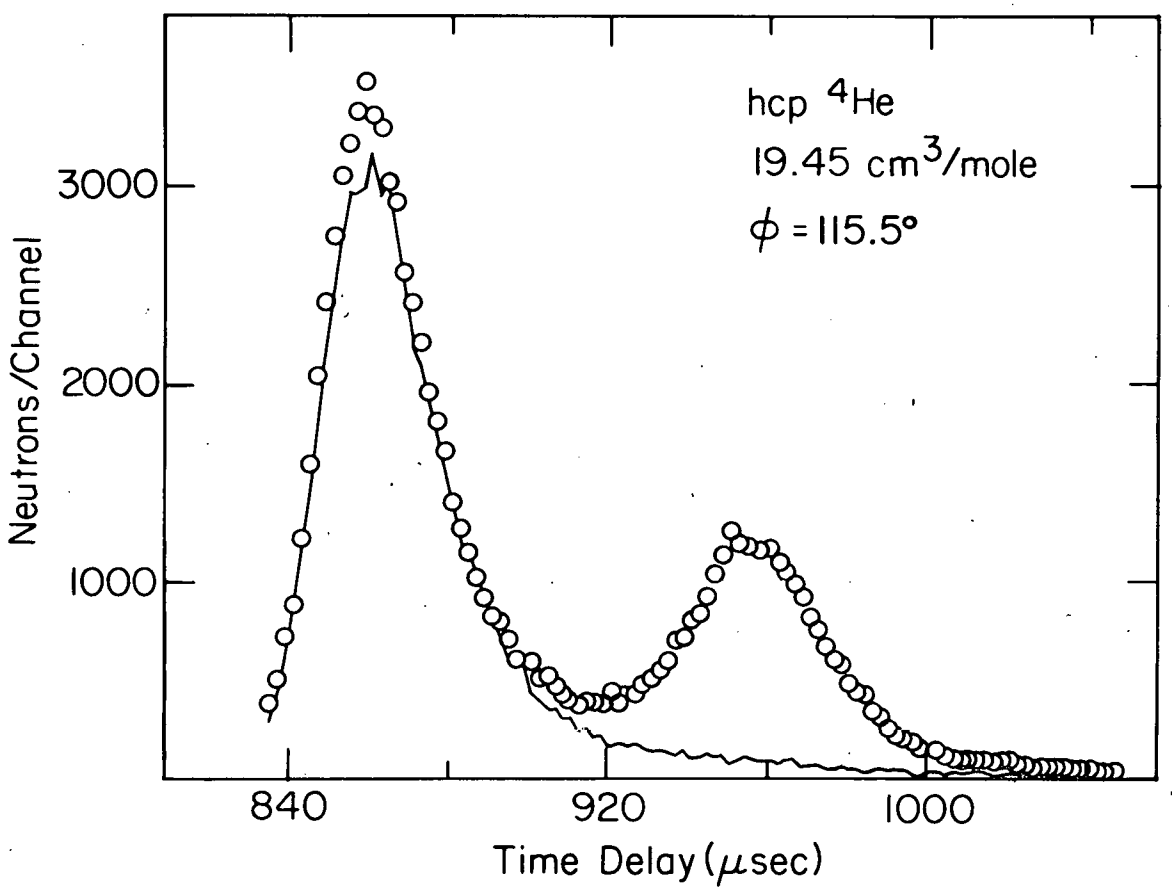

Figure 12. Total number of neutrons detected per 2 μsec channel versus flight time. These raw data were collected on the low density hcp sample by the detector group centered at a scattering angle of 115.5°.

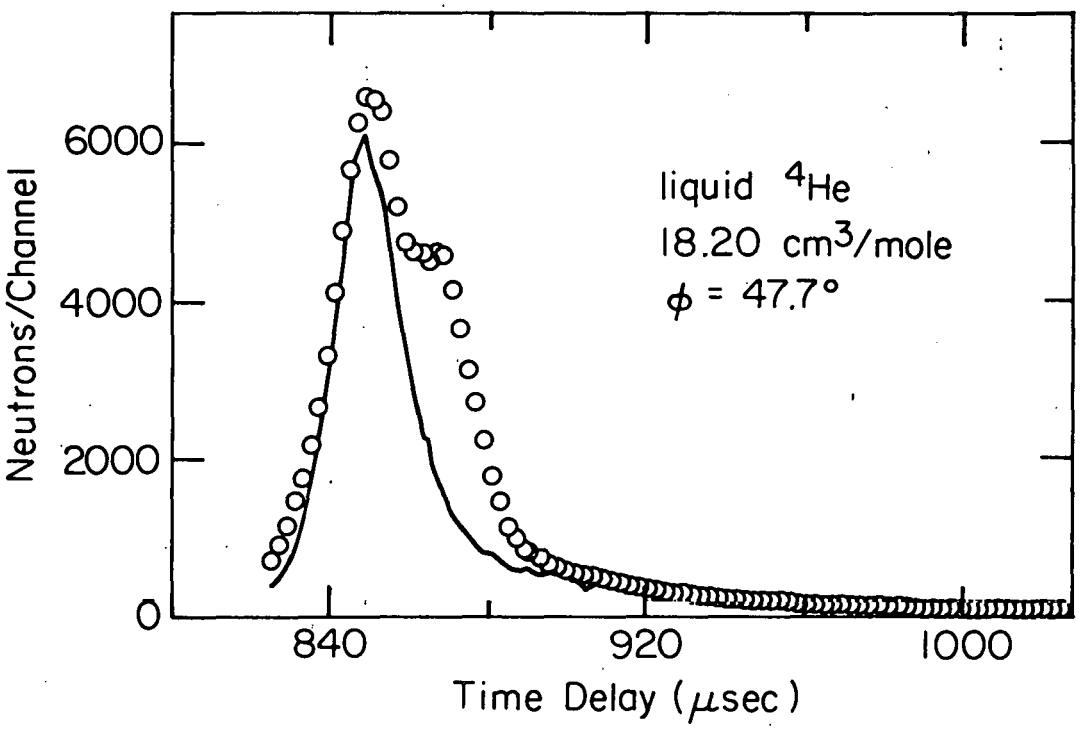

Figure 13. Total number of neutrons detected per 2 μsec channel versus flight time. These raw data were collected on the liquid sample by the detector group centered at a scattering angle of 47.7°. The line represents the data collected with the sample cell empty; the points represent the data collected with the helium sample in the cell.

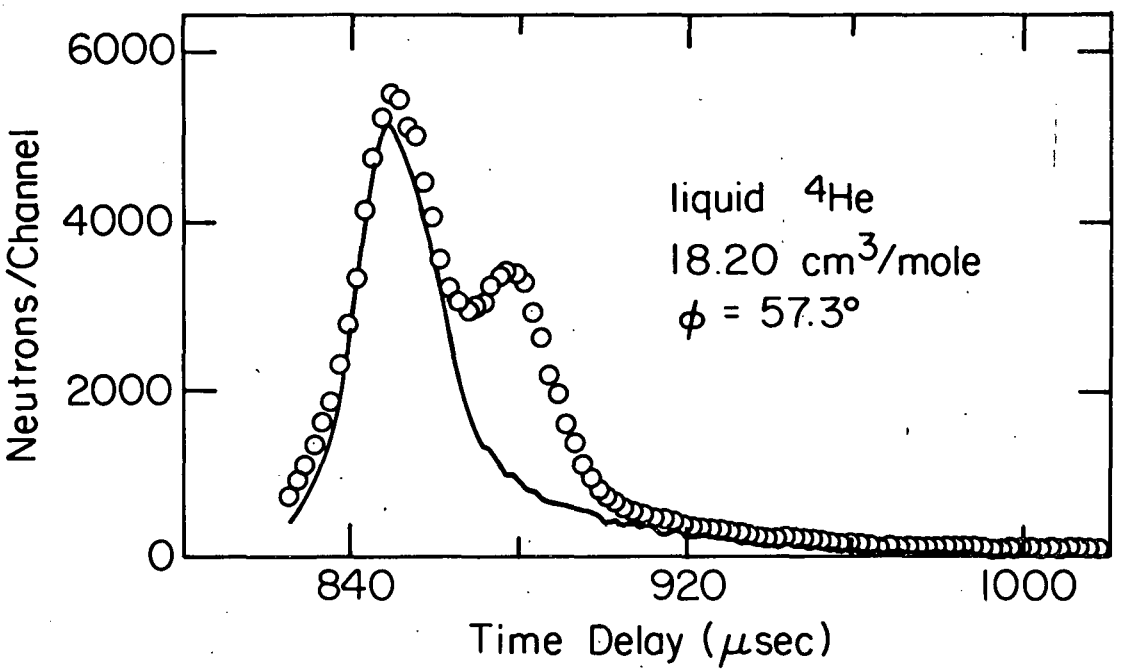

Figure 14. Total number of neutrons detected per 2 μsec channel versus flight time. These raw data were collected on the liquid sample by the detector group centered at a scattering angle of 57.3°.

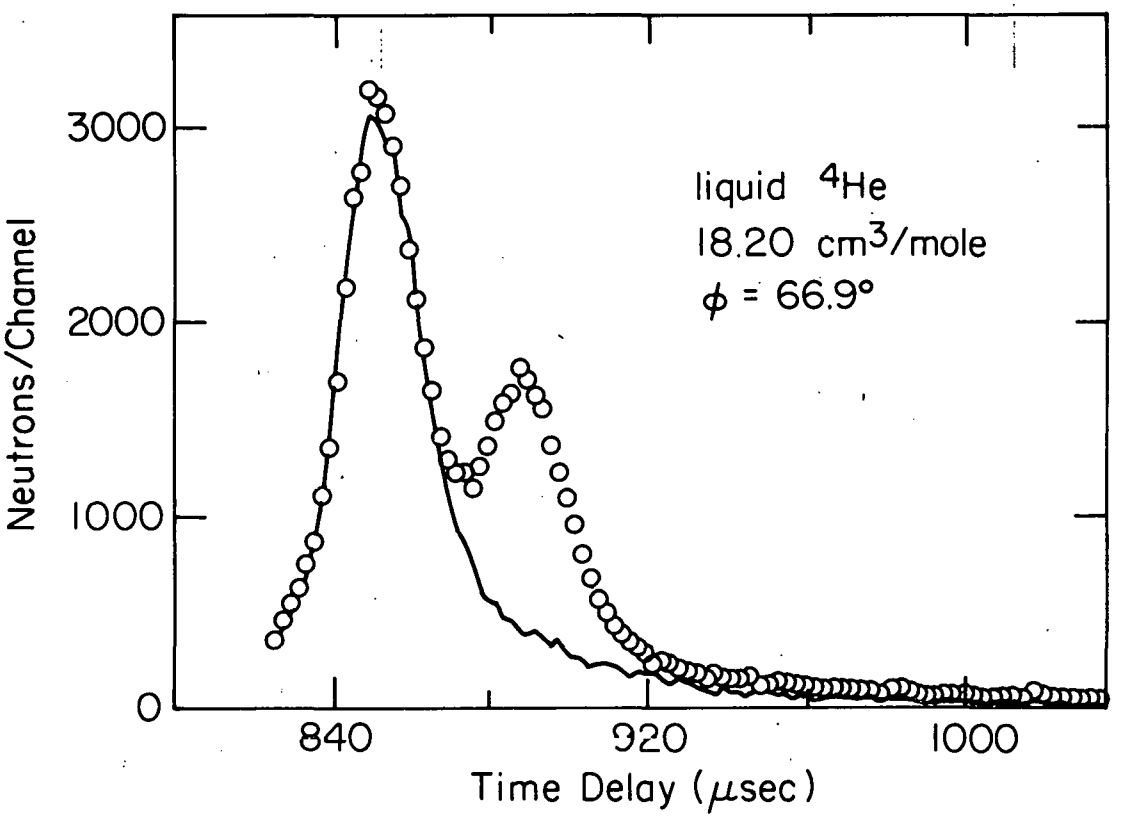

Figure 15. Total number of neutrons detected per 2 μsec channel versus flight time. These raw data were collected on the liquid sample by the detector group centered at a scattering angle of 66.9°.

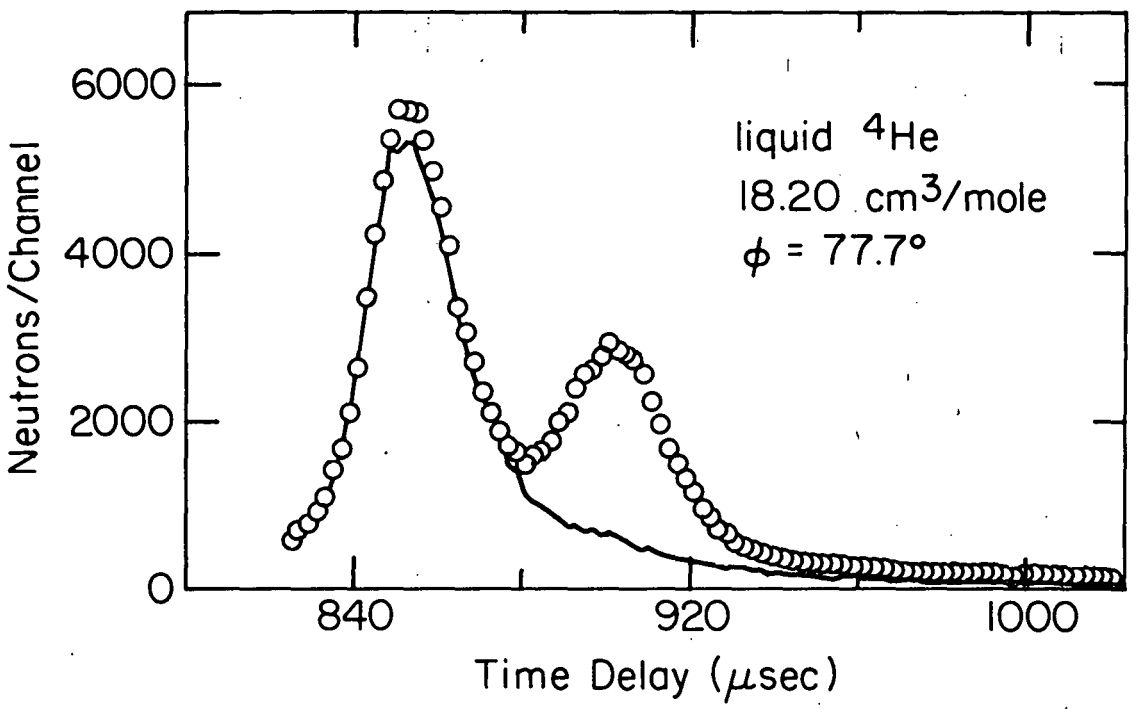

Figure 16. Total number of neutrons detected per 2 μsec channel versus flight time. These raw data were collected on the liquid sample by the detector group centered at a scattering angle of 77.7°.

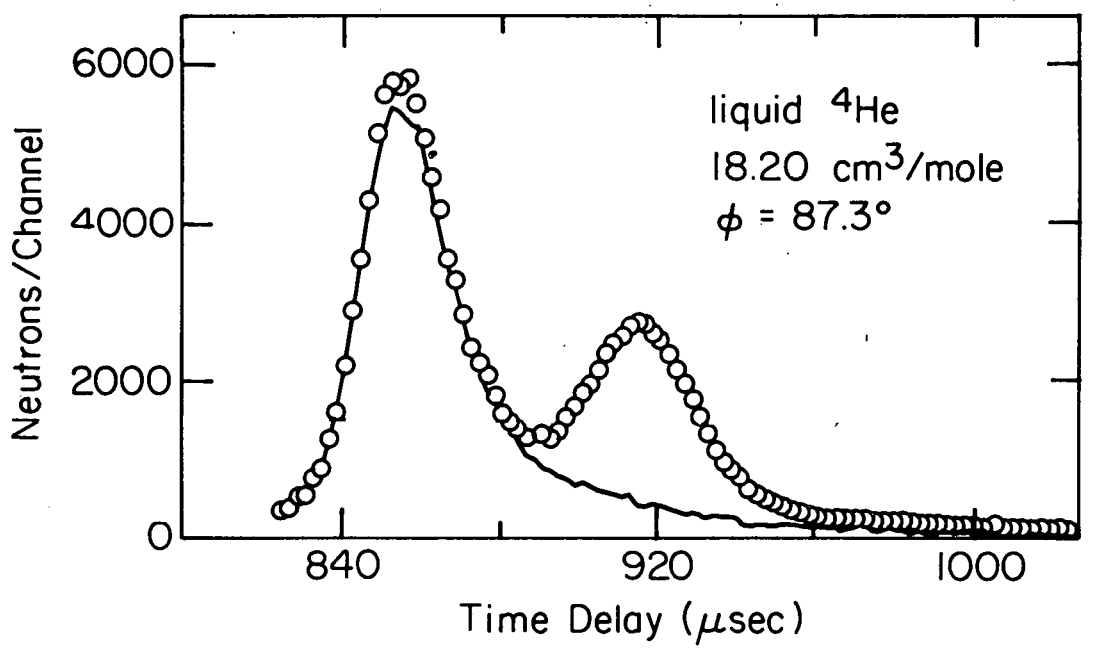

Figure 17. Total number of neutrons detected per 2 μsec channel versus flight time. These raw data were collected on the liquid sample by the detector group centered at a scattering angle of 87.3°.

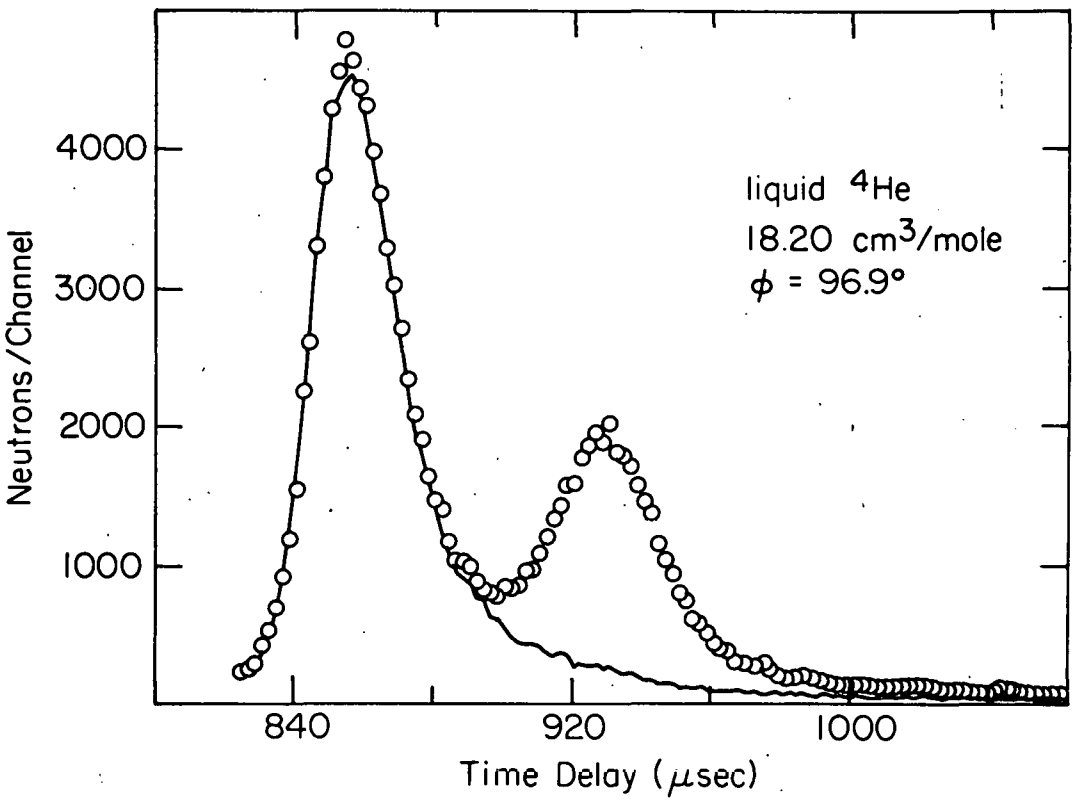

Figure 18. Total number of neutrons detected per 2 μsec channel versus flight time. These raw data were collected on the liquid sample by the detector group centered at a scattering angle of 96.9°.

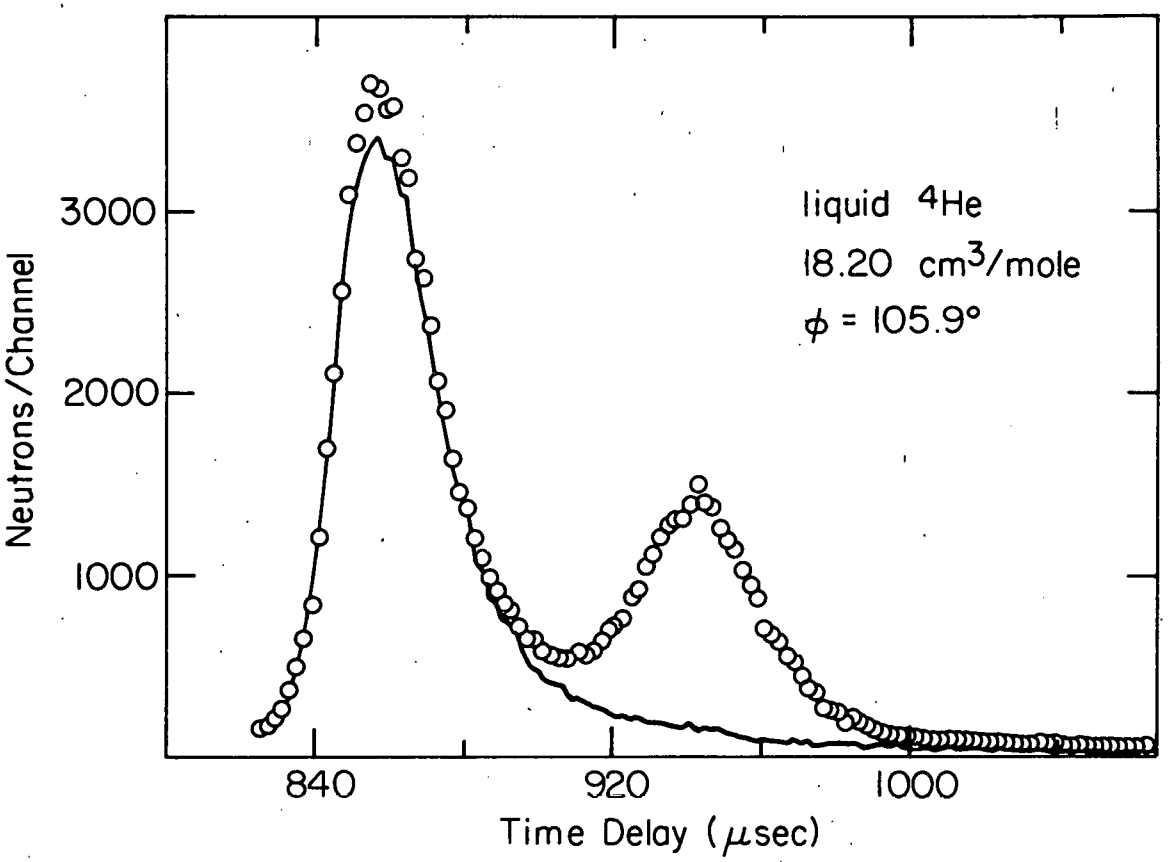

Figure 19. Total number of neutrons detected per 2 μsec channel versus flight time. These raw data were collected on the liquid sample by the detector group centered at a scattering angle of 105.9°.

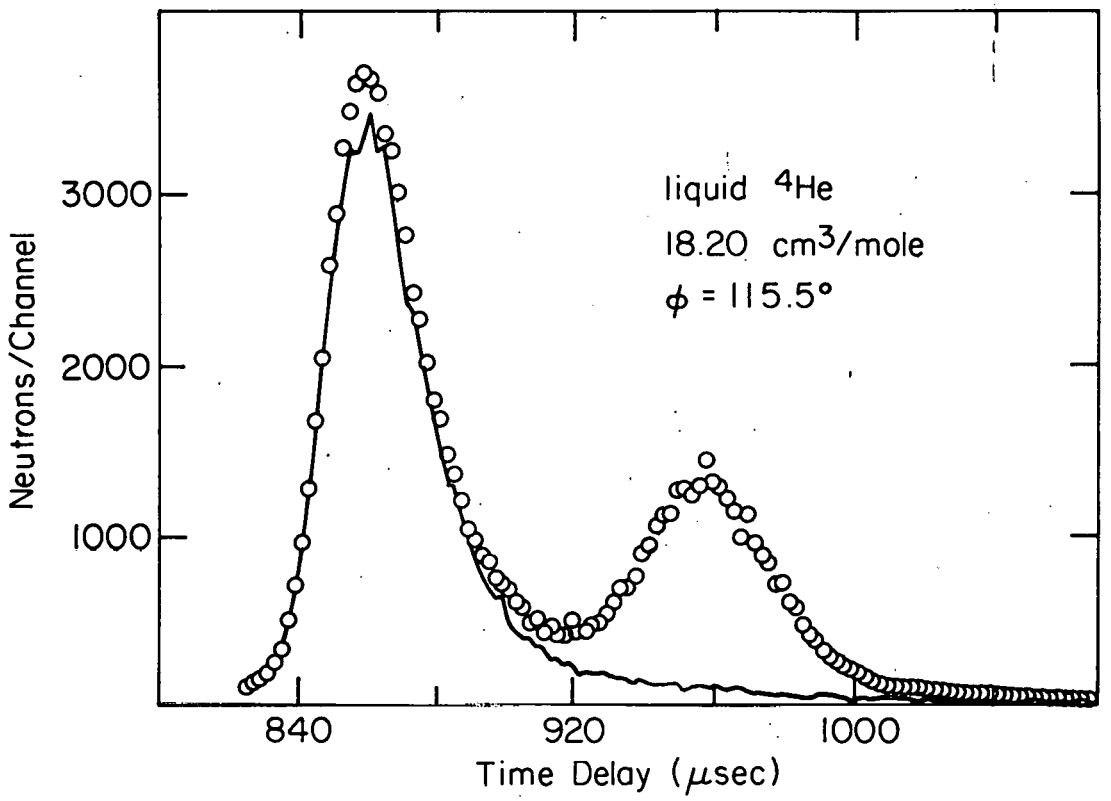

Figure 20. Total number of neutrons detected per 2 μsec channel versus flight time. These raw data were collected on the liquid sample by the detector group centered at a scattering angle of 115.5°.

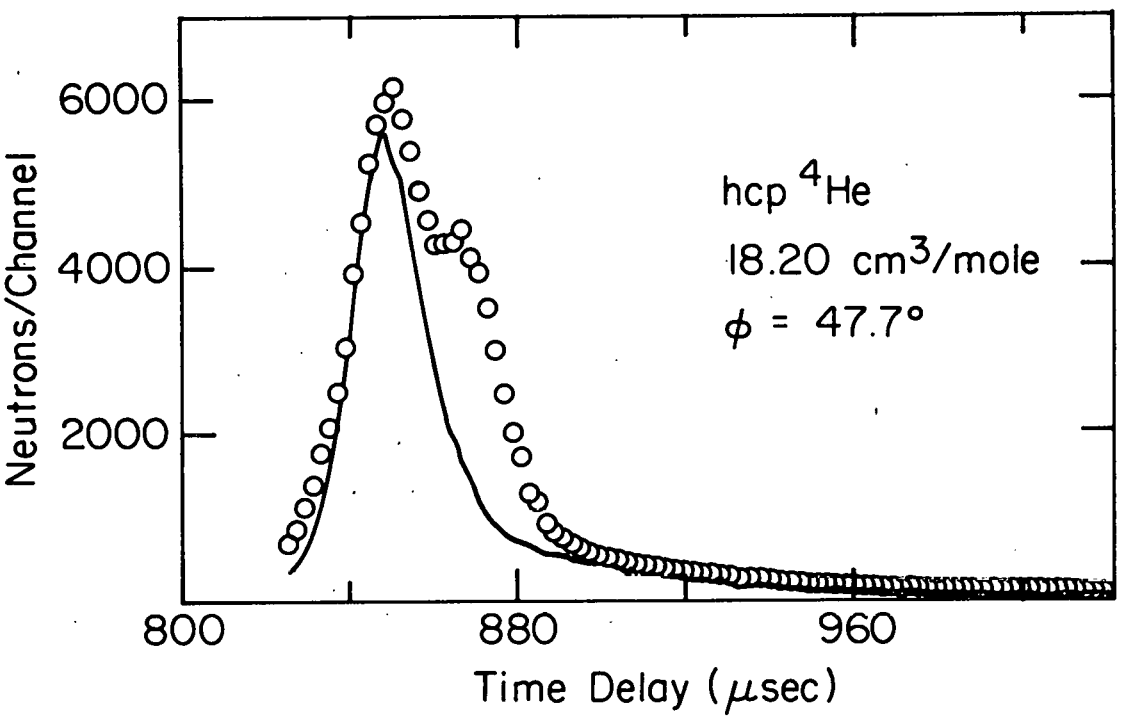

Figure 21. Total number of neutrons detected per 2 μsec channel versus flight time. These raw data were collected on the high density hcp sample by the detector group centered at a scattering angle of 47.7°. The line represents the data collected with the sample cell empty; the points represent the data collected with the helium sample in the cell.

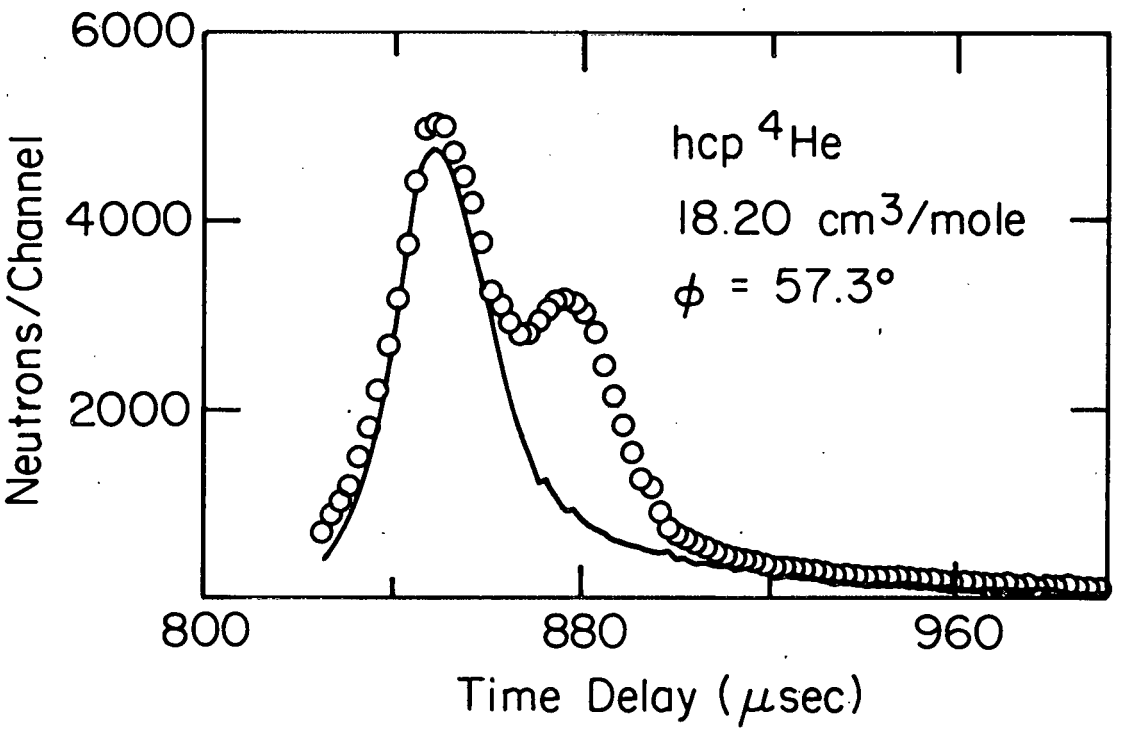

Figure 22. Total number of neutrons detected per 2 μsec channel versus flight time. These raw data were collected on the high density hcp sample by the detector group centered at a scattering angle of 57.3°.

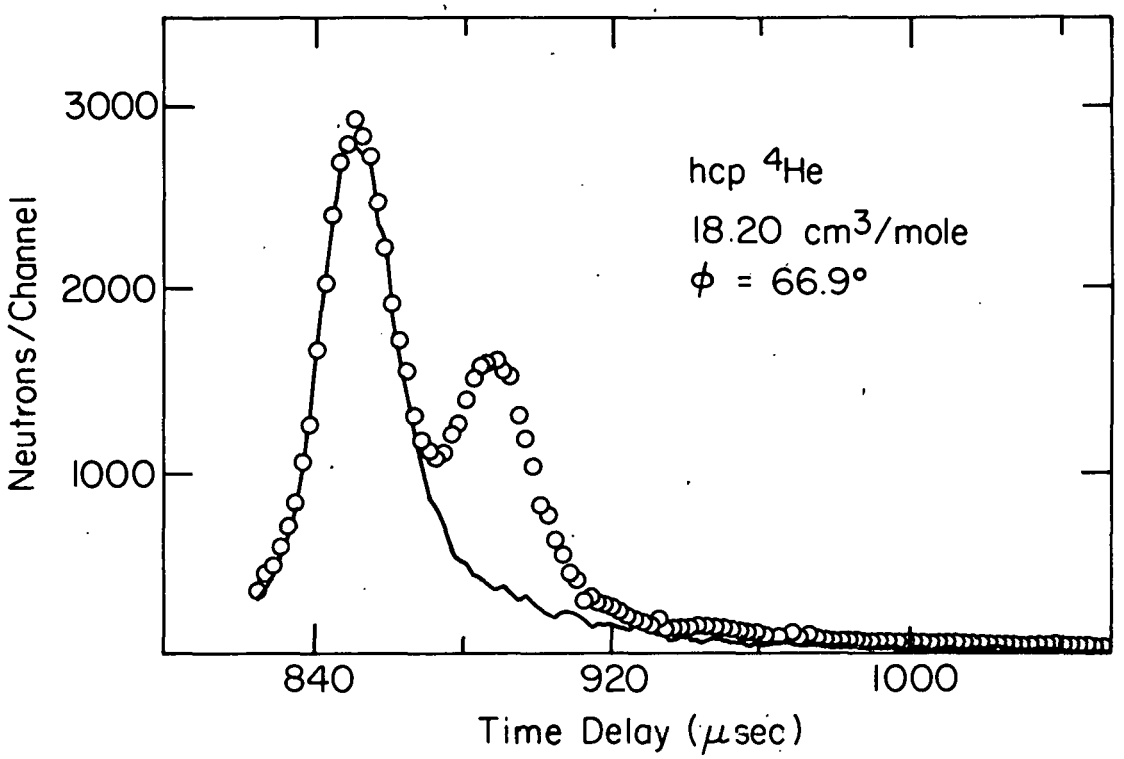

Figure 23. Total number of neutrons detected per 2 μsec channel versus flight time. These raw data were collected on the high density hcp sample by the detector group centered at a scattering angle of 66.9°.

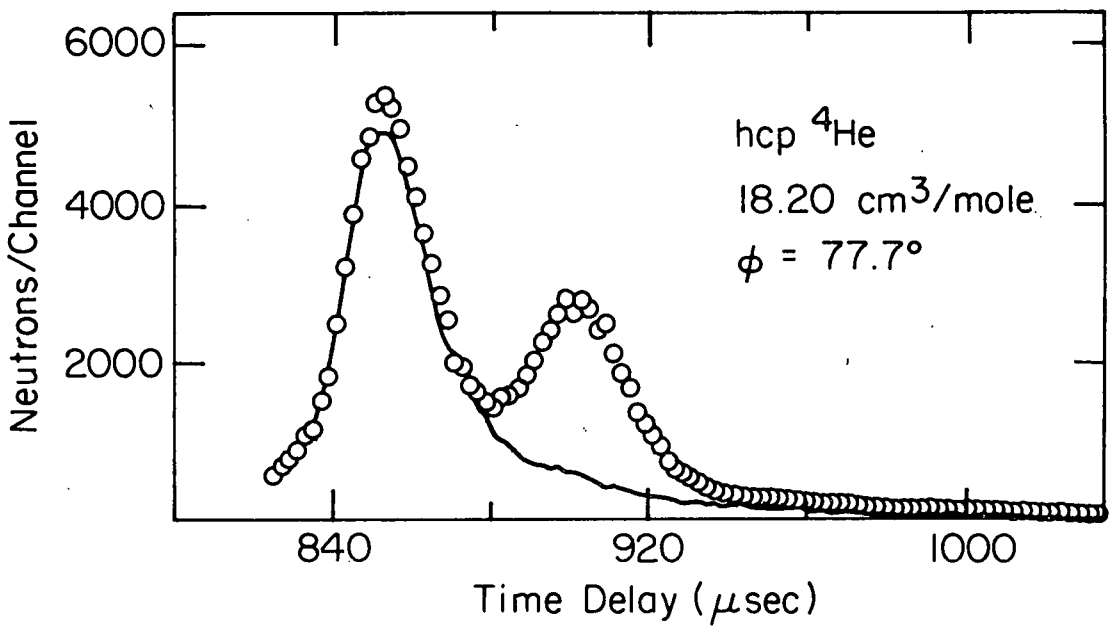

Figure 24. Total number of neutrons detected per 2 μsec channel versus flight time. These raw data were collected on the high density hcp sample by the detector group centered at a scattering angle of 77.7°.

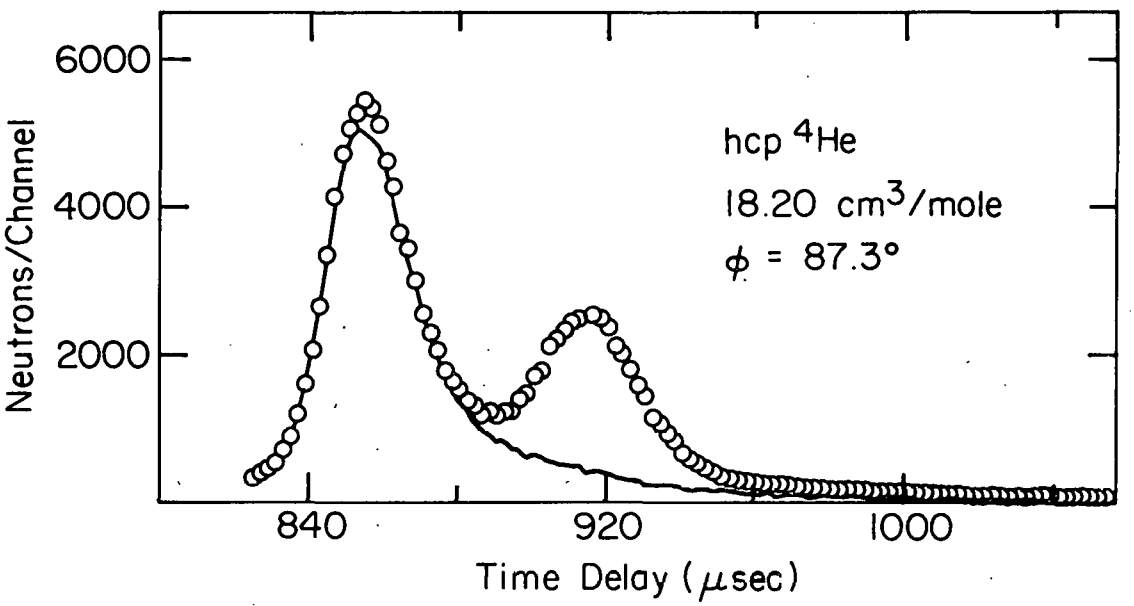

Figure 25. Total number of neutrons detected per 2 μsec channel versus flight time. These raw data were collected on the high density hcp sample by the detector group centered at a scattering angle of 87.3°.

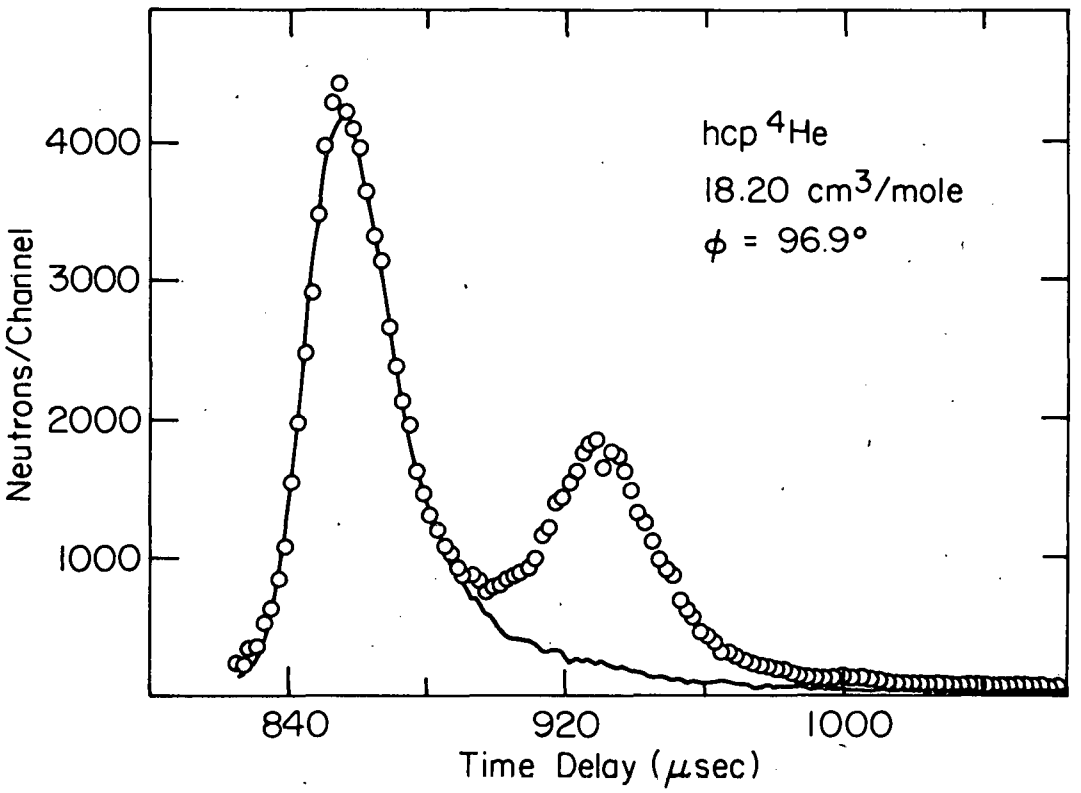

Figure 26. Total number of neutrons detected per 2 μsec channel versus flight time. These raw data were collected on the high density hcp sample by the detector group centered at a scattering angle of 96.9°.

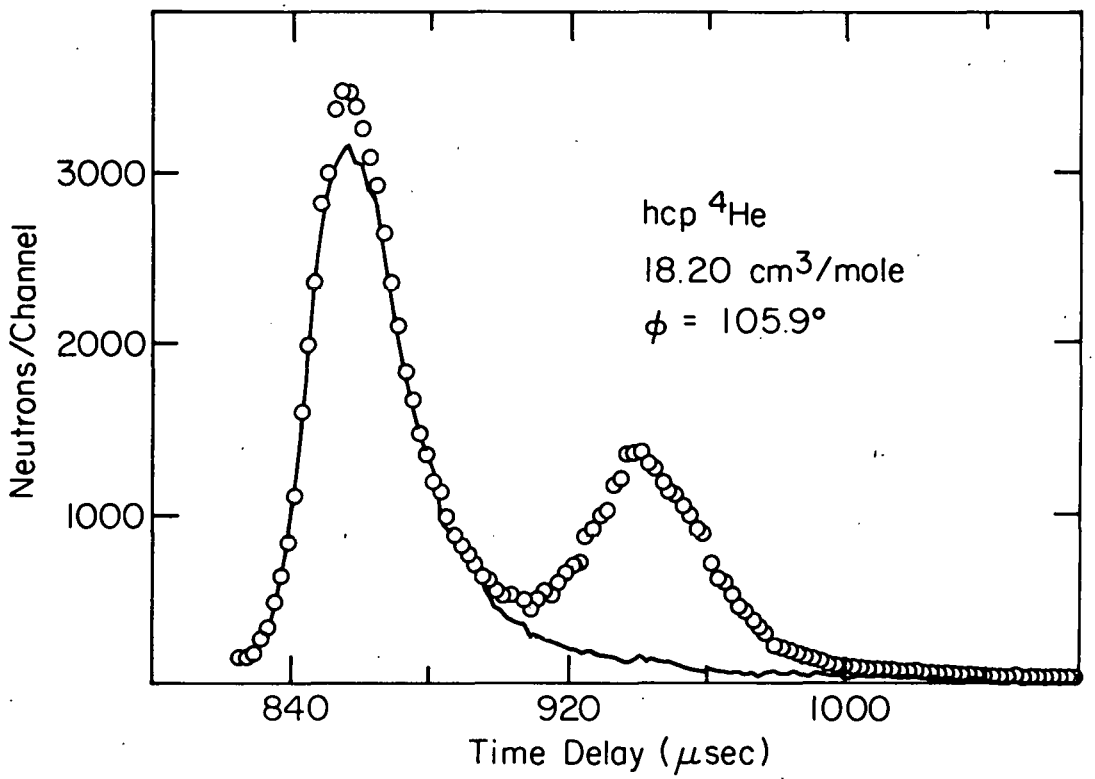

Figure 27. Total number of neutrons detected per 2 μsec channel versus flight time. These raw data were collected on the high density hcp sample by the detector group centered at a scattering angle of 105.9°.

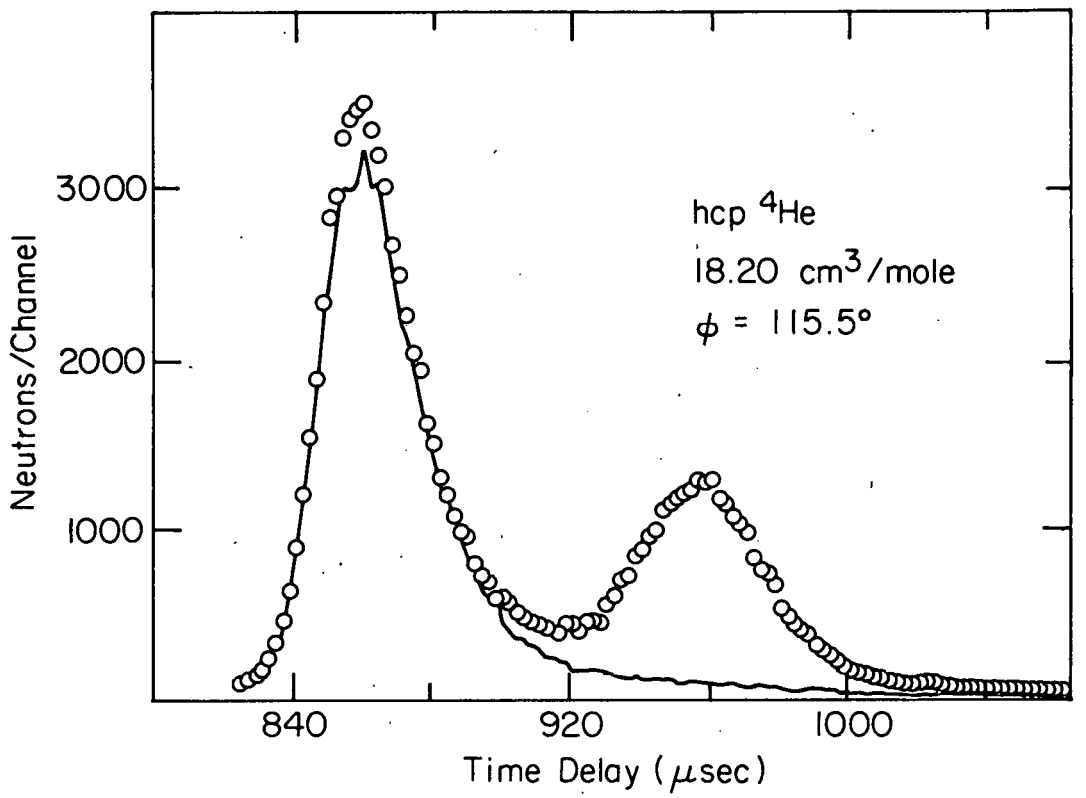

Figure 28. Total number of neutrons detected per 2 μsec channel versus flight time. These raw data were collected on the high density hcp sample by the detector group centered at a scattering angle of 115.5°.

D. Raw Data Characteristics

One will notice several important characteristics of the raw data. The most striking is that the center of the helium recoil peak moves to longer flight time (higher momentum transfer) as one progresses toward larger scattering angle. If the impulse approximation exactly describes the behavior of this scattering process, the peak center should be related to the momentum transfer by Equation (17). Our data fit this relation accurately (see Figure 58) with relatively small deviations explained in the next chapter.

The second characteristic is that the peaks broaden as the scattering angle increases. This is a consequence of plotting the data as a function of neutron flight time. If the data were plotted as a function of energy transfer, the broadening of the peak would be much less perceptible. Three processes conspire to keep σ_ϕ roughly independent of scattering angle: 1) the width of the constant-$\vec{Q}$ peaks, σ_Q, increases linearly with Q (see Equation (19)), 2) the conversion from constant angle data to constant-$\vec{Q}$ data is a function of scattering angle (see Equations (25) and (26)), and 3) the resolution of the spectrometer is a function of $\vec{Q}$ (see Table 1).

The final characteristic of the raw data is that the peak area, equal to the number of neutrons detected at each scattering angle, should be independent of

scattering angle. Since the neutron wavelength is four orders of magnitude larger than the size of the scattering nucleus, inelastic neutron scattering is mostly isotropic s-wave scattering. The observed number of neutrons in each of our peaks varies by no more than 5% as a function of angle. This variation is probably due to varying detector efficiency.

One will notice in Figures 5 through 28 that the data points lie above the background in the vicinity of the elastic peak. This may be due to multiply scattered neutrons. If a 505 meV neutron scatters from a ^{4}He atom initially at rest, through a scattering angle of 90°, the energy transfer will be 203 meV. If a 505 meV neutron scatters twice, each time with ^{4}He atoms initially at rest and each time through 45°, it will be detected and recorded as a neutron that had scattered through 90° and its energy transfer will be calculated as 130 meV. Finally, if a 505 meV neutron scatters from a ^{4}He atom then from an aluminum atom (or vice versa), both times through 45°, its energy transfer will be 79 meV. One will notice that in each case the energy transfer for two consecutive 45° scattering events is smaller than for one 90° scattering event; this result holds for all scattering angles. Thus a neutron that is doubly scattered so that it emerges at an angle ϕ to the unscattered beam will be observed as having suffered an energy loss that is smaller than

expected for a neutron that scatters once from a ^{4}He atom through a scattering angle ϕ. Obviously one must require that both events have scattering angles less than ϕ. On a plot of the raw data, these neutrons will be recorded in the vicinity of the elastic peak. Thus the elastic peak will be larger in the sample data set than in the background data set after normalization for the total neutron flux on the sample.

E. Empty Cell, Background and Vanadium Data

The empty cell data for correction purposes were taken with the sample cell near liquid helium temperature and the two radiation shields at their normal temperatures of liquid nitrogen and liquid helium.

Empty cell data were also taken as the cryostat cooled originally. The spectroscopic peaks for the warm sample cell are significantly broader than the corresponding peaks for the cold sample cell. This gave early confidence that the peak broadening is actually due to atomic motion and suggests that one can resolve the temperature-dependent single-atom kinetic energy. Unfortunately, these data cannot be analyzed to determine the temperature dependence of the momentum density of aluminum for two reasons. First, the warm sample cell data were taken as the cell cooled from room temperature to liquid nitrogen temperature. The cold cell data were taken as the cell

cooled from about 20 K to about 2 K. Thus the average temperature was not well specified during the collection of these two sets of data. Second, some of the scattering was caused by the nitrogen and helium temperature radiation shields. These aluminum tails were at temperatures different from the sample cell. Further, the configuration of these tails led to broadening of the peaks related to the diameter of the tails compared to the diameter of the sample cell. One could probably measure the momentum density and its temperature dependence in aluminum given a different sample configuration and more care in temperature control.

As discussed in Chapter 2, scattering from vanadium is used to check experimentally the calculated resolution of a spectrometer and to calibrate the scattered neutron intensity. A piece of vanadium foil at about 300 K was placed in the sample position and data were taken for 39.06 hours beam time. These data are shown in analyzed form in Figures 54 through 57.

To take the background data, everything was removed from the room temperature hat and it was evacuated. The background scattering is a measure of the neutron scattering from various parts of the spectrometer (chopper, collimators, room temperature hat, beam monitors, beam stop, the atmosphere in the unevacuated parts of the beam path). This scattering was very weak and seemed to consist mostly

of scattering from the room temperature hat. The background data are subtracted from the vanadium data leaving only the neutron spectrum scattered from the vanadium sample.

For optimum data statistics, the ratio of the sample to empty cell and vanadium to background run durations should be in proportion to the count rates.[33] This, along with restrictions due to spectrometer scheduling, determined how long data were collected on each sample.

F. Diffraction Data

After the spectroscopic data were taken on the second solid sample, the chopper was removed thus turning the instrument into a time-of-flight diffractometer. Data were collected during 16.5 clock hours for a measured 15.9 hours beam time. The data were once again recorded as counts versus neutron flight time; the computer software for data collection and analysis was a slightly modified version of the software used on the General Purpose Powder Diffractometer. This measurement was not planned when the cryostat was designed and in fact was first suggested by S. K. Sinha while we were taking data on the first solid sample. Because neither the cryostat nor the spectrometer were designed for diffraction experiments, Bragg peaks corresponding to only seven reflections could be seen. These were the (100), (002), (101), (102), (110), (103), and (200) reflections. The peaks which

correspond to planes having smaller spacing are lost among the aluminum peaks at small flight times. In fact, the (200) helium reflection lies on top of one of the aluminum peaks but is visible as the difference in heights of the sample and empty cell data.

The sample and empty cell data from the detector group at 57.3° are shown in Figure 29. This data set is shown because it includes six of the seven observable peaks. One will note that several of the large aluminum peaks consist of a large central peak with two smaller peaks on each side. These correspond to scattering from the sample cell (the central peak), the front and back surfaces of the helium tail (the two adjacent peaks), and the front and back surfaces of the nitrogen tail (the outer two peaks).

There is one important difference between powder diffraction with a pulsed source and a steady state source that is evident in Figure 29. With a steady state source, a continuous stream of monoenergetic neutrons is incident on the sample and the diffracted beam emerges in cones, each cone corresponding to scattering from a set of equivalent planes.[50] A detector at a scattering angle ϕ will record scattering from a set of planes only if the corresponding cone intersects the detector. With a pulsed source diffractometer, a range of neutron wavelengths is present in the incident beam and scattering from a given

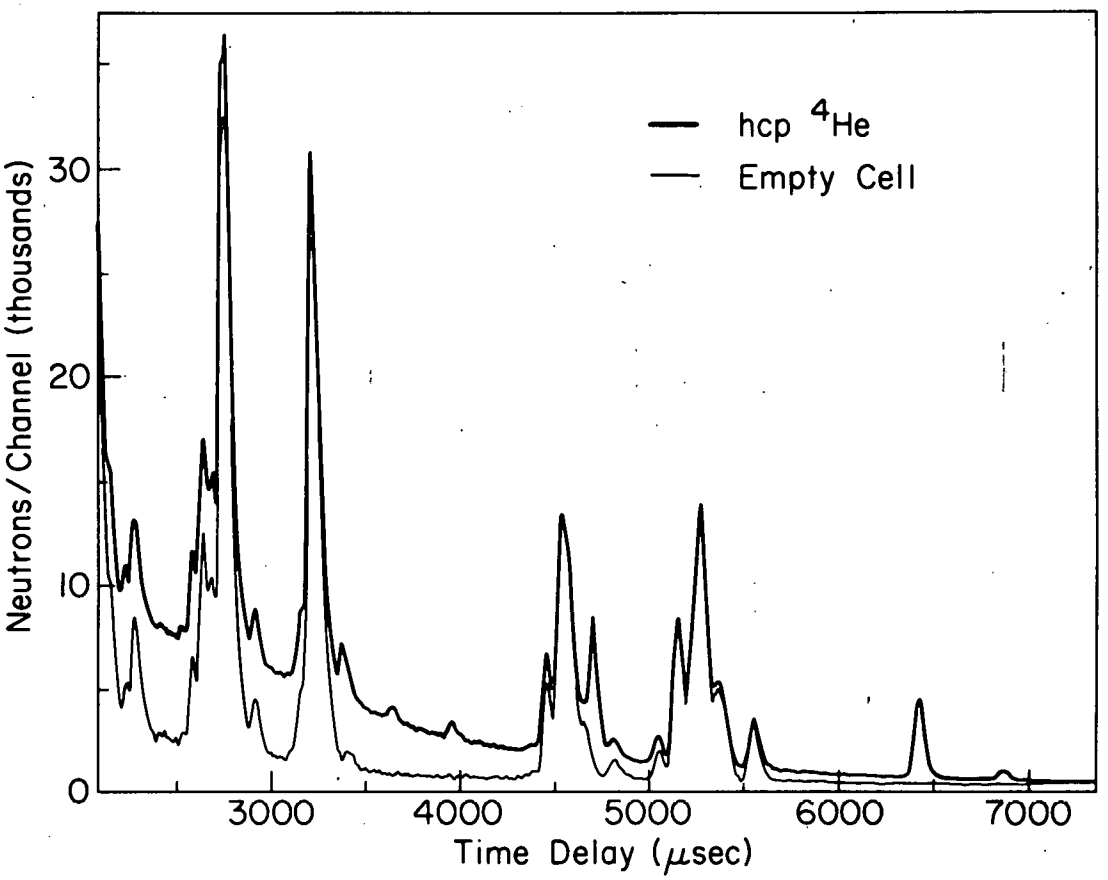

Figure 29. Time-of-flight diffraction data taken by the detector group centered at a scattering angle of 57.3°. The narrow line represents the empty cell data; the heavy line represents the data taken with the 18.20 cm^3/mole hcp ^{4}He sample in the cell. The large peaks, visible in both data sets, are due to coherent scattering from the aluminum sample cell and radiation shields. Six helium Bragg peaks are visible at this scattering angle: 1) the peak at 6850 μsec corresponds to a (100) reflection, 2) the peak at 6450 μsec corresponds to (002), 3) the peak at 4700 μsec corresponds to (102), 4) the peak at 3960 μsec corresponds to (110), 5) the peak at 3640 μsec corresponds to (103), and 6) the peak at 3430 μsec corresponds to (200). The (101) reflection (which would occur at 6050 μsec) is not evident in these data. Reflections corresponding to planes having smaller lattice spacing are lost among the aluminum peaks at smaller flight times.

set of planes will be observable by detectors at (essentially) all scattering angles. In the present case, the seven observable peaks would be present in each of the eight detector groups if the sample was a powder.

Diffraction data were taken on the empty sample cell for 5.42 hours and are displayed as background in Figure 29. Vanadium and background diffraction data were taken for 7.67 hours and 3.25 hours respectively, and are included in the data analysis discussed in the next chapter.

5. ANALYSIS

As discussed in the previous chapter, there were six sets of spectroscopic data taken. These consist of inelastic scattering from: 1) 19.45 cm^3/mole hcp ^4He, 2) 18.20 cm^3/mole liquid ^4He, 3) 18.20 cm^3/mole hcp ^4He, 4) empty sample cell, 5) vanadium foil, and 6) the spectrometer background.

A. Determination of $S(\phi,E)$

"CHOP" is a computer program on the VAX 11/780 computer at IPNS-1 that calculates the dynamic structure factor from the raw data.[34] The main factors in the conversion can be illustrated by this equation:

$$S(\phi,E) = C[I_S(\phi,t)-I_E(\phi,t)\frac{N_S}{N_E}SAF(\phi)]FF(\phi)\eta(E)\frac{t_3^3}{mL_3^2\delta t} \quad (31)$$

$I_S(\phi,t)$ and $I_E(\phi,t)$ are the observed neutron intensity scattered by the sample and by the empty cell for a given angle as a function of flight time. N_S and N_E are the number of neutrons incident on the sample and the empty cell as determined by the beam monitors. C represents various factors that convert scattered flux as a function of flight time into the scattering function.

The sample attenuation factor, $SAF(\phi)$, corrects the data for the attenuation of the neutron flux by the sample.

Because of this attenuation, the neutron flux incident on the back side of the sample cell is less than in the empty cell case; thus the scattering from the sample is not just the difference between the filled cell and empty cell data. The energy dependent detector efficiency, $\eta(E)$, is determined from the scattered spectrum of vanadium. The indelicately named fudge factor, $FF(\phi)$, is included to normalize the incoherent scattering from the sample to the (almost) perfectly incoherent scattering from vanadium, the standard to which one usually normalizes unknown scattering.

The last factor in Equation (31) is the nonlinear conversion from flight time to energy transfer as the independent variable. One will notice that the conversion is nonlinear meaning the peak in $I(\phi,t)$ does not have the same profile as $S(\phi,E)$. Furthermore, if the time intervals are all equal (δt = 2 μsec in Figures 5 through 28), the energy intervals will be smaller for higher energy transfer (notice the unequal spacing of points in Figures 30 through 53).

The $S(\phi,E)$ versus E data were fit to a Gaussian with a linear background of the form

$$S(\phi,E) = A_1 \exp\left[-\frac{(E - E_r)^2}{2\sigma_\phi^2}\right] + A_2 + A_3E \quad . \qquad (32)$$

Initially, we tried a fitting function with a quadratic term, A_4E^2. This was rejected because, though it gave a

slightly better fit (chi squared was fractionally smaller), the term had unphysical behavior at the highest and lowest energy data points used in the fit; that is, it curved wildly just beyond the region of data that was fit. We also tried a fitting function of the form in Equation (32) with $A_3 = 0$, i.e., with a constant background. This was rejected because several of the peaks have obviously sloped backgrounds and the constant background fit those peaks poorly (see, for example, Figures 35, 43, and 50).

The sloped background may be due to multiple scattering. Multiply scattered neutrons will appear as background in the inelastic scattering data. Since the neutron energy is much larger than any excitation energy in the system, the neutron is most likely to lose energy in every collision with the system. One would expect the background to have a positive slope ($A_3 > 0$), because, on average, a multiply scattered neutron has lost more energy than a singly scattered one. As the energy transfer increases, one would expect to observe more multiply scattered (i.e. background) neutrons. The problem is not so simple since one must allow for multiple scattering from the aluminum cell and the helium sample and take into account their configuration in the experiment. A project beyond the scope of this thesis is to carry out a Monte Carlo calculation that will properly account for these effects and explain, if possible, this background in more detail.

Such a calculation will also reveal more about the details of the resolution function which is necessary to explore the deviation of the tails of the peaks from the Gaussian behavior[25,27] (see discussion in Chapter 6). Such a calculation is planned.

Figures 30 through 53 show the three sets (eight figures for each of three samples) of the plots of the scattering function at fixed angle versus energy transfer. $S(\phi,E)$ is extracted from the raw time-of-flight data via Equation (31); these are displayed as the data points with associated error bars. The best fit Gaussian and background function of the form given by Equation (32) is shown in the figures as the line. The scattering function for the low density solid sample is shown in Figures 30 through 37, that for the liquid sample is shown in Figures 38 through 45, and that for the high density solid sample is shown in Figures 46 through 53. A complete data set for each sample consists of eight such peaks (corresponding to a peak at each of eight scattering angles). One should notice that the data show no systematic deviation from the Gaussian fits to $S(\phi,E)$.

There are five fit parameters in Equation (32): E_r, σ_ϕ, A_1, A_2, and A_3. The values found for E_r and σ_ϕ are listed in Tables 2 through 4. A_1, A_2, and A_3 have no intrinsic physical significance but their values are

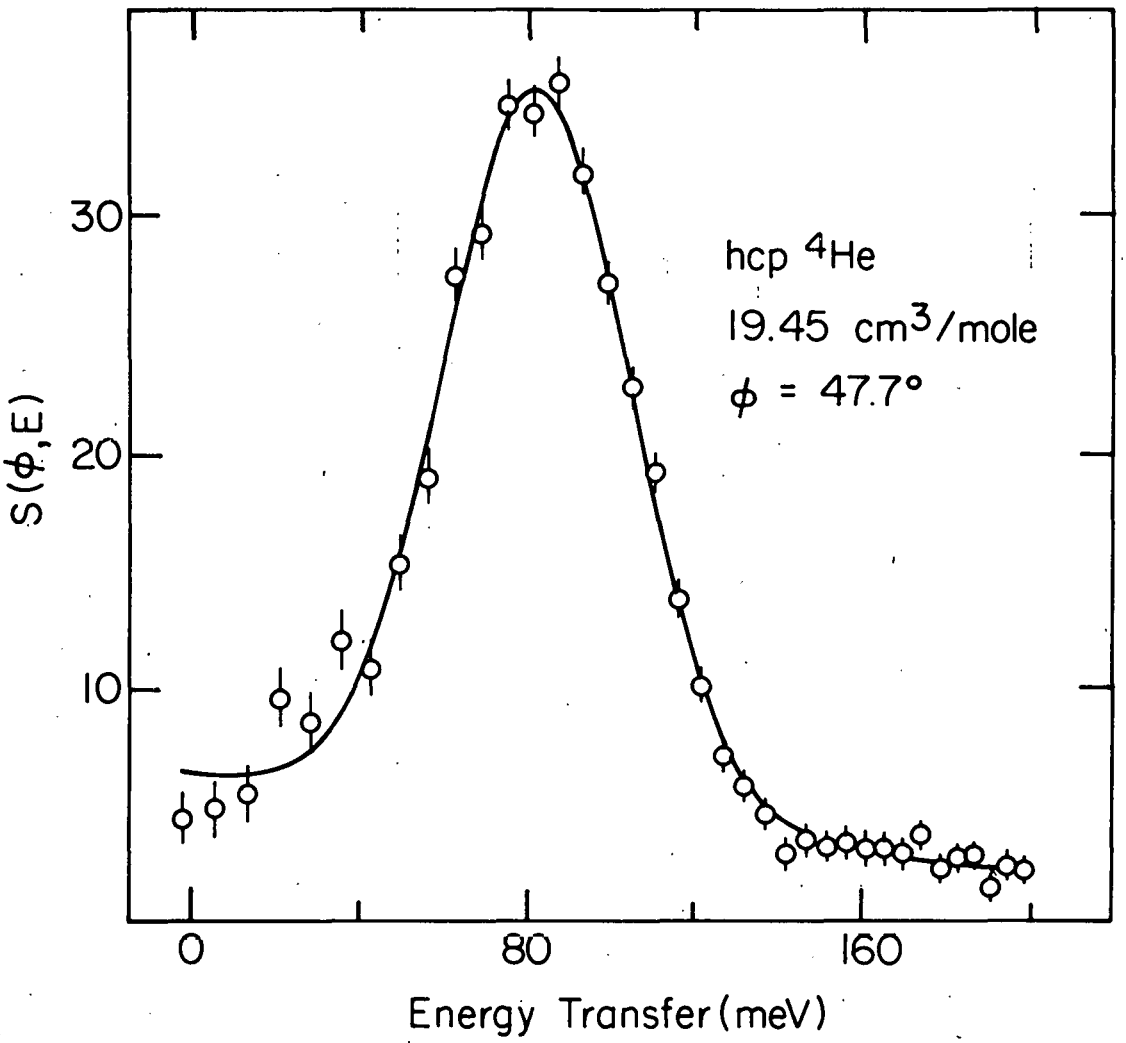

Figure 30. The scattering function derived from data taken at a fixed scattering angle. These data were taken on the low density hcp sample at a scattering angle of 47.7°. The curve is the best fit Gaussian of the form given by Eqn. (32). The spectrometer resolution has not been subtracted from these data.

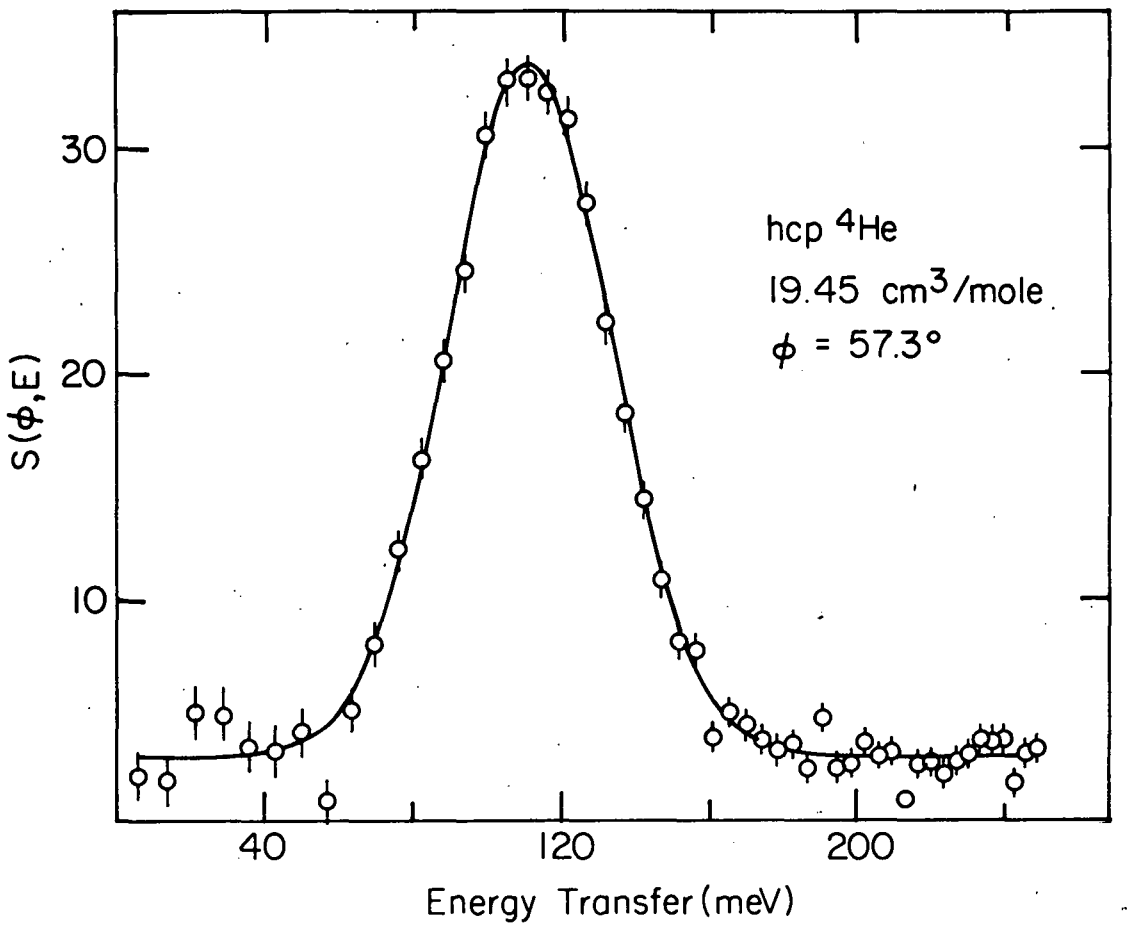

Figure 31. The scattering function derived from data taken at a fixed scattering angle. These data were taken on the low density hcp sample at a scattering angle of 57.3°. The curve is the best fit Gaussian of the form given by Eqn. (32).

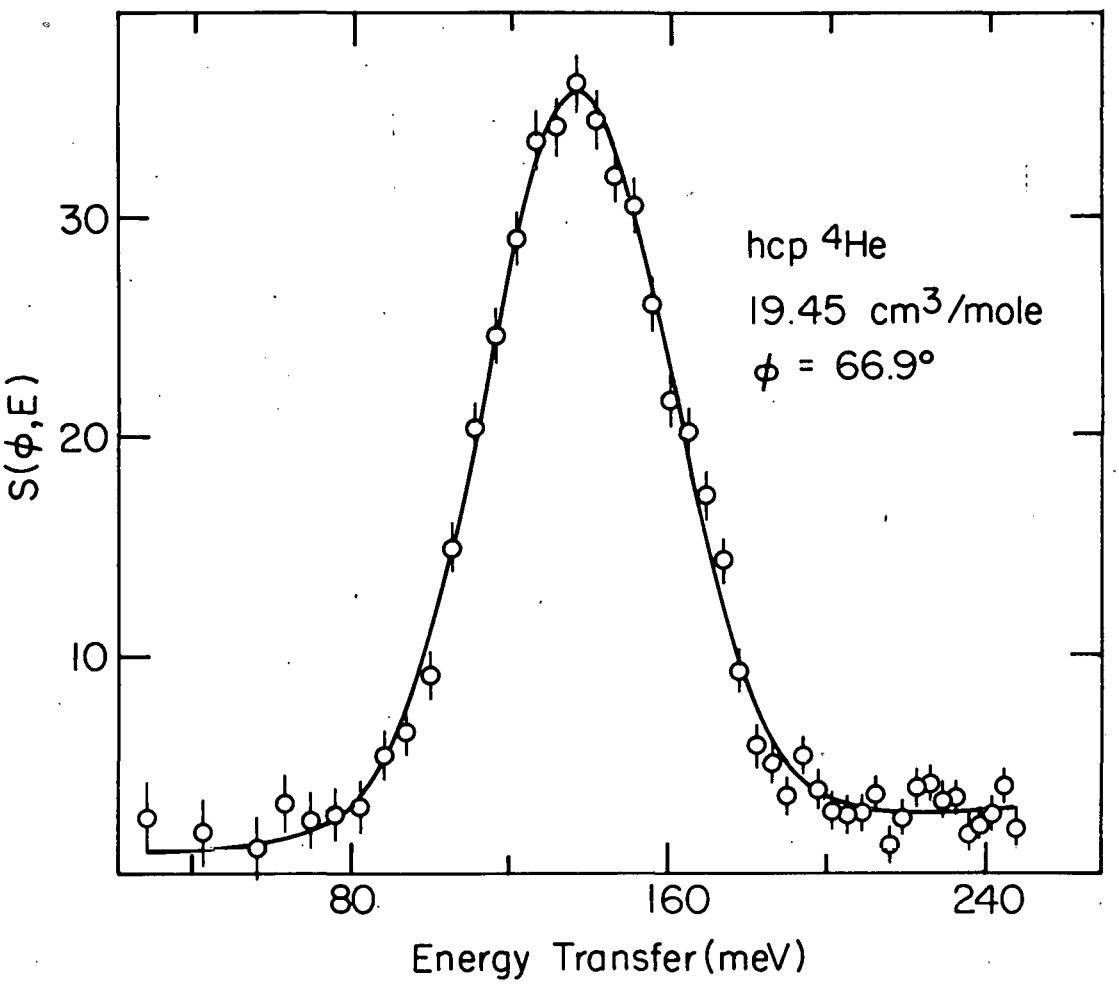

Figure 32. The scattering function derived from data taken at a fixed scattering angle. These data were taken on the low density hcp sample at a scattering angle of 66.9°.

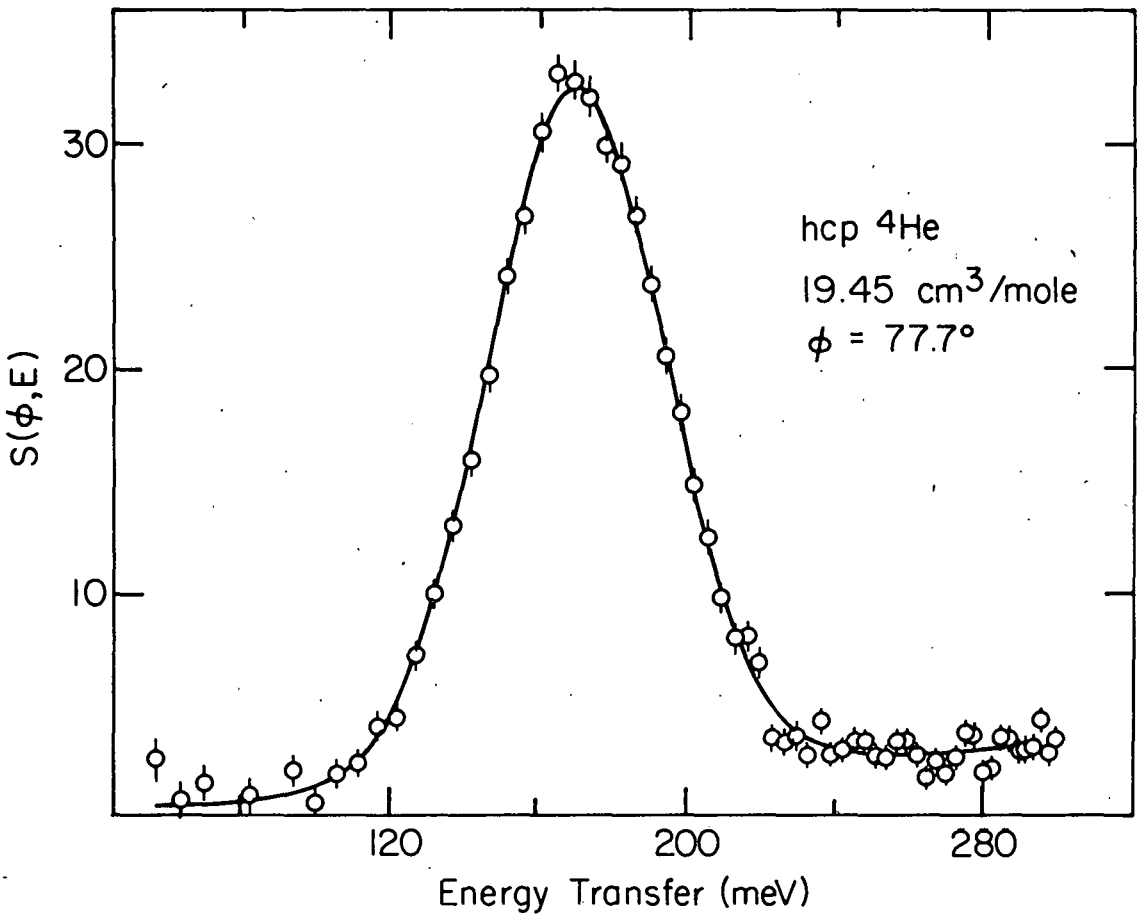

Figure 33. The scattering function derived from data taken at a fixed scattering angle. These data were taken on the low density hcp sample at a scattering angle of 77.7°.

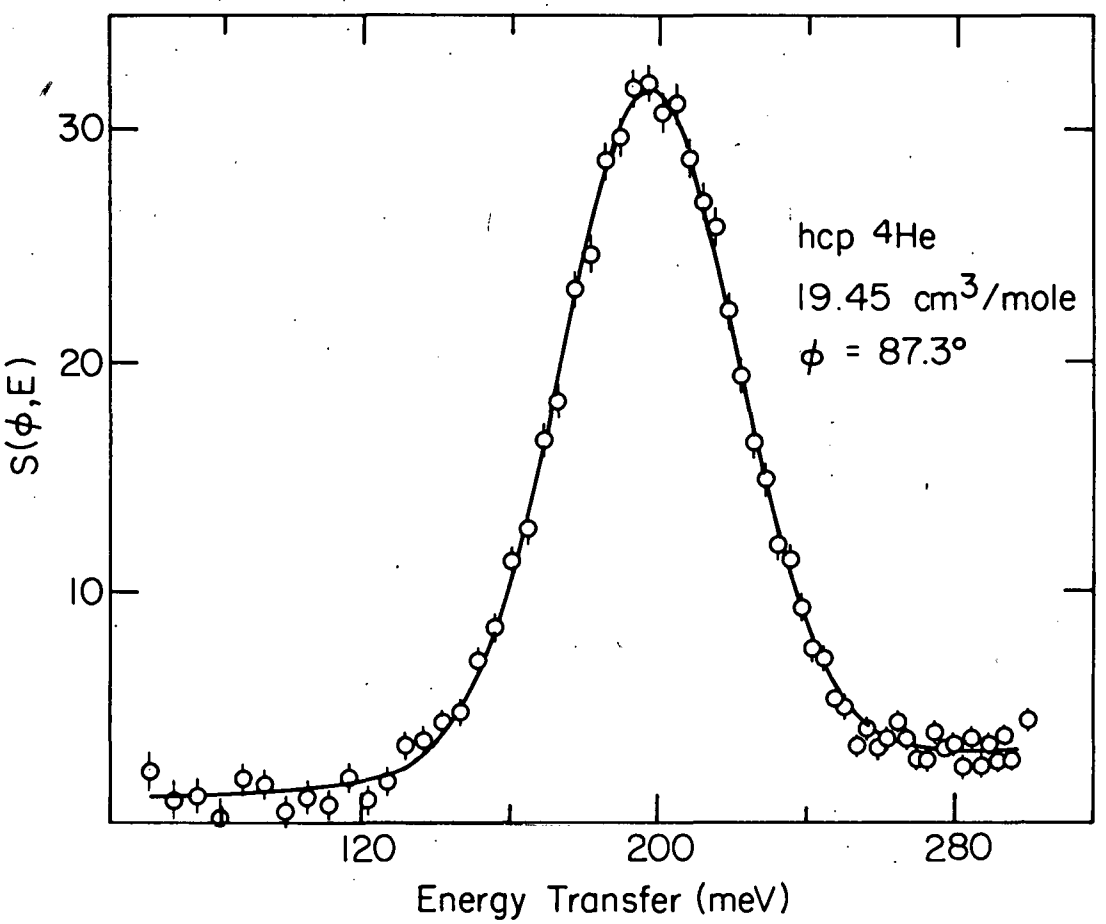

Figure 34. The scattering function derived from data taken at a fixed scattering angle. These data were taken on the low density hcp sample at a scattering angle of 87.3°.

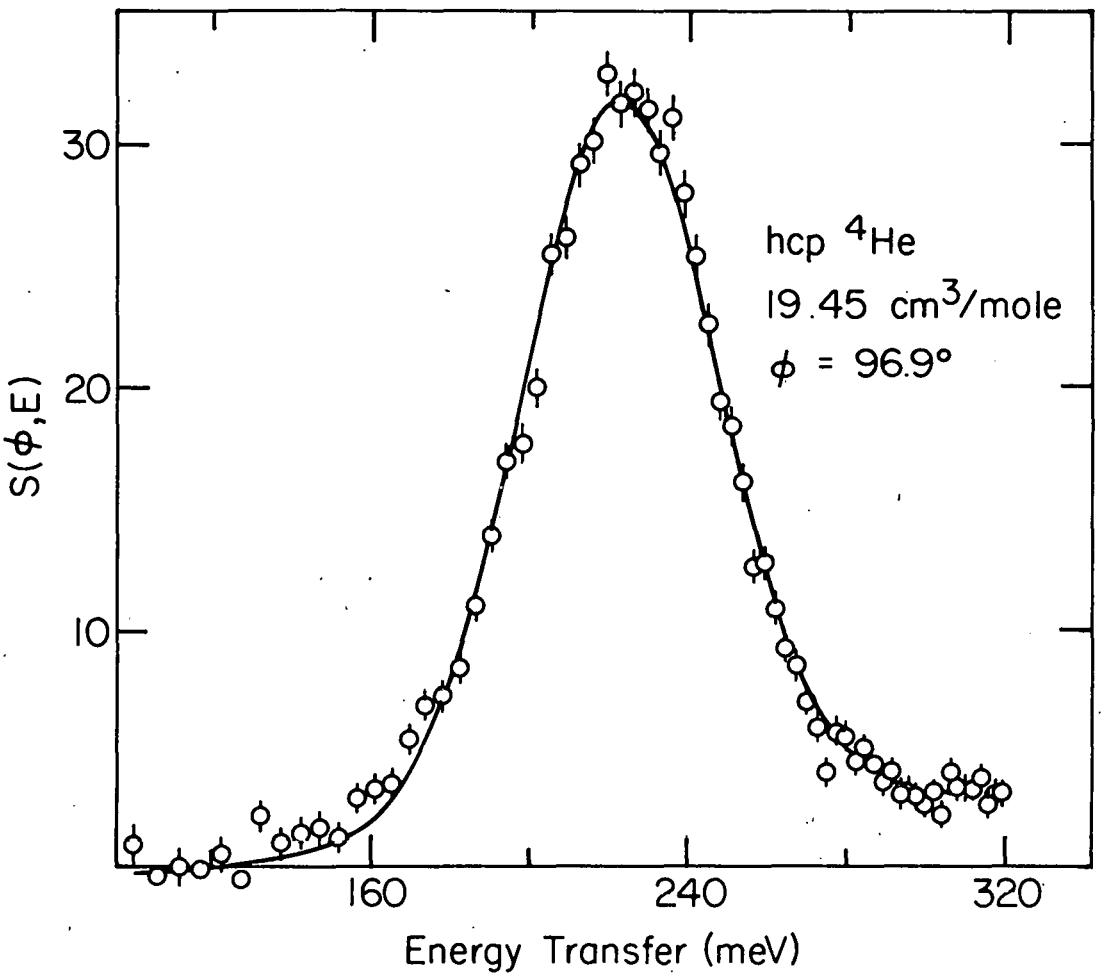

Figure 35. The scattering function derived from data taken at a fixed scattering angle. These data were taken on the low density hcp sample at a scattering angle of 96.9°.

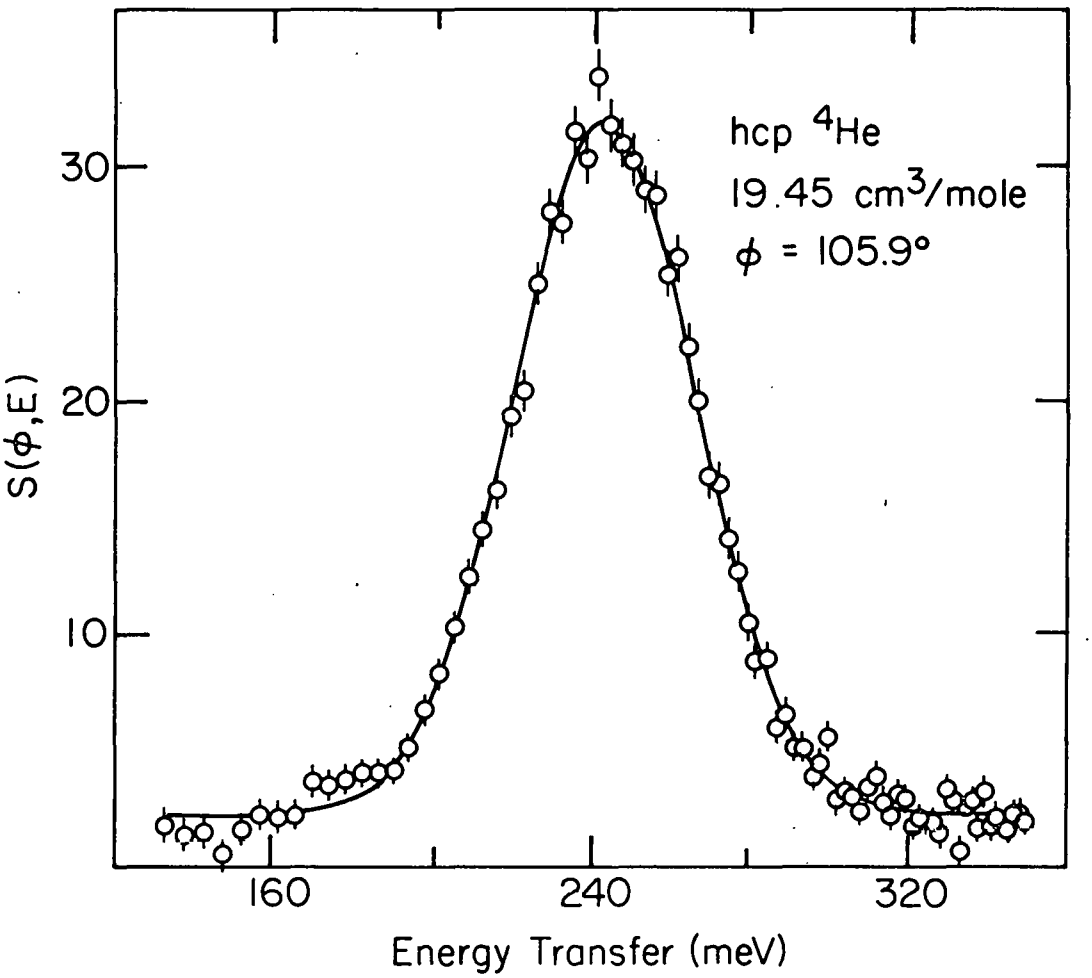

Figure 36. The scattering function derived from data taken at a fixed scattering angle. These data were taken on the low density hcp sample at a scattering angle of 105.9°.

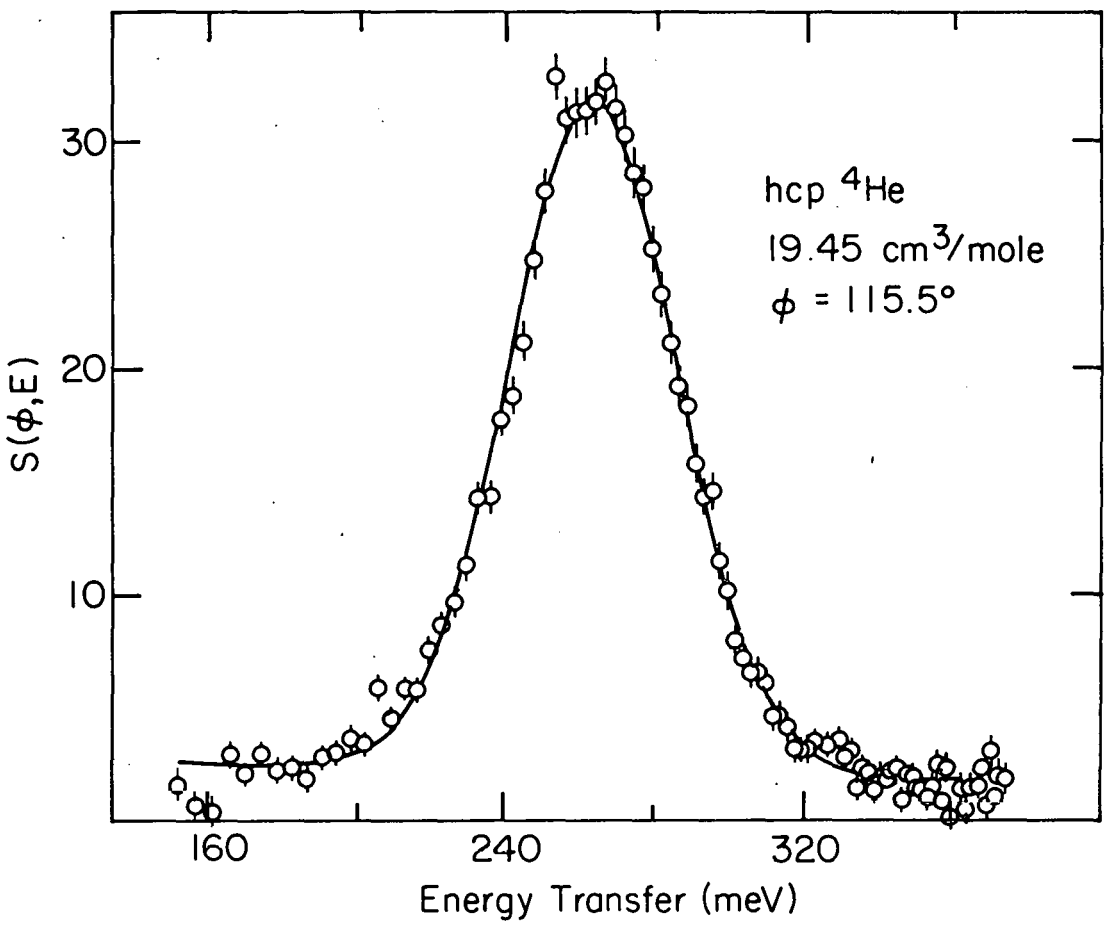

Figure 37. The scattering function derived from data taken at a fixed scattering angle. These data were taken on the low density hcp sample at a scattering angle of 115.5°.

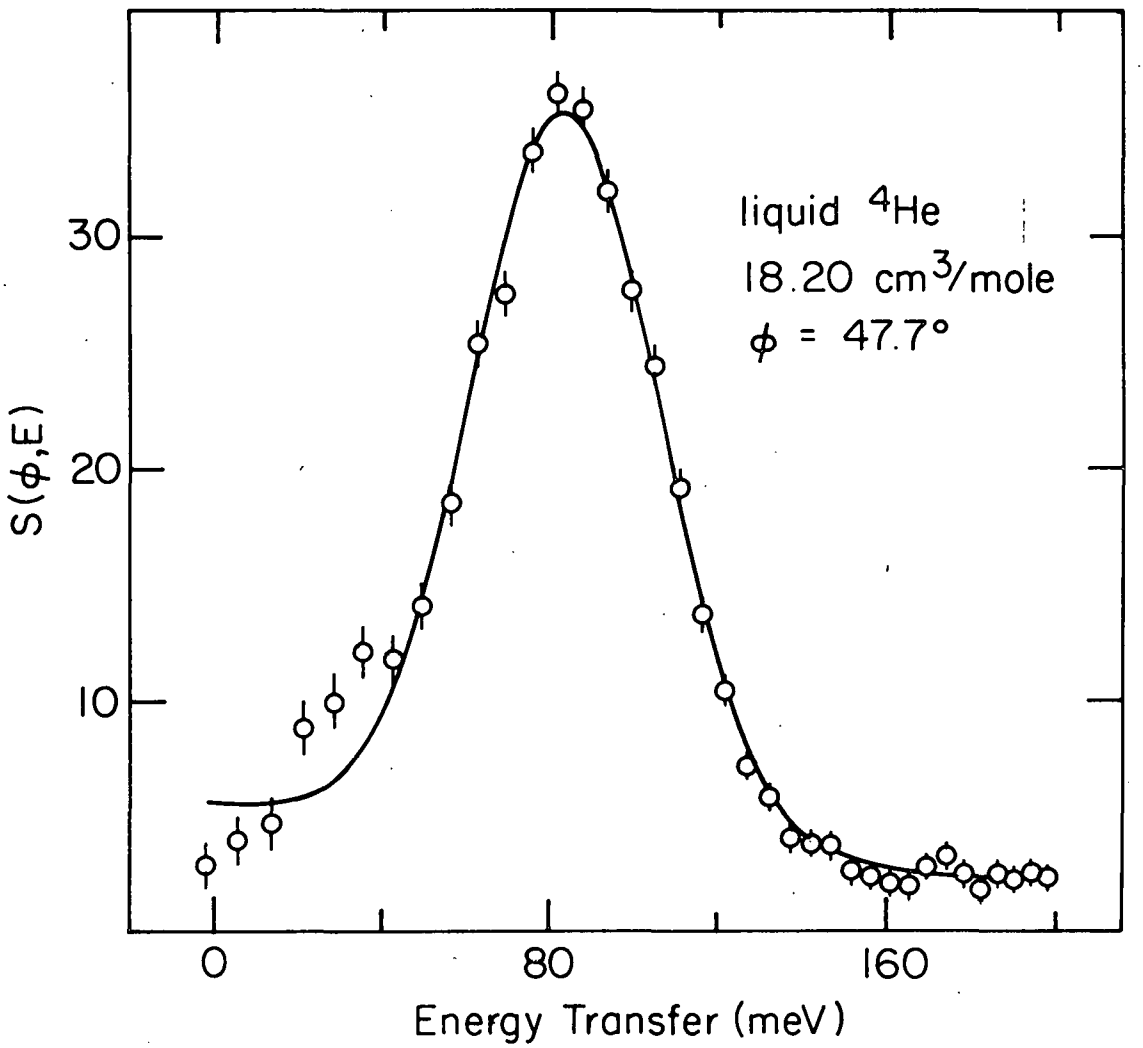

Figure 38. The scattering function derived from data taken at a fixed scattering angle. These data were taken on the liquid sample at a scattering angle of 47.7°. The curve is the best fit Gaussian of the form given by Eqn. (32). The spectrometer resolution has not been subtracted from these data.

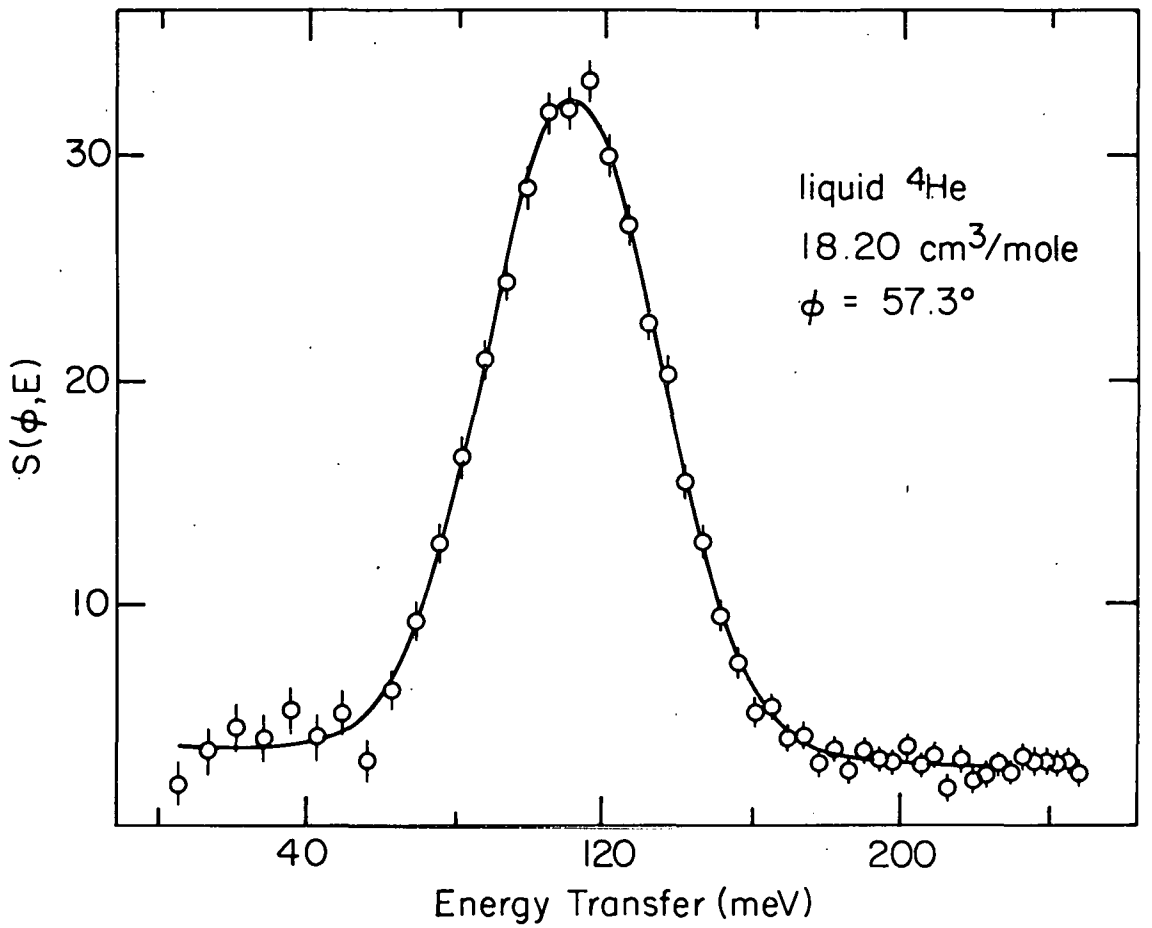

Figure 39. The scattering function derived from data taken at a fixed scattering angle. These data were taken on the liquid sample at a scattering angle of 57.3°. The curve is the best fit Gaussian of the form given by Eqn. (32).

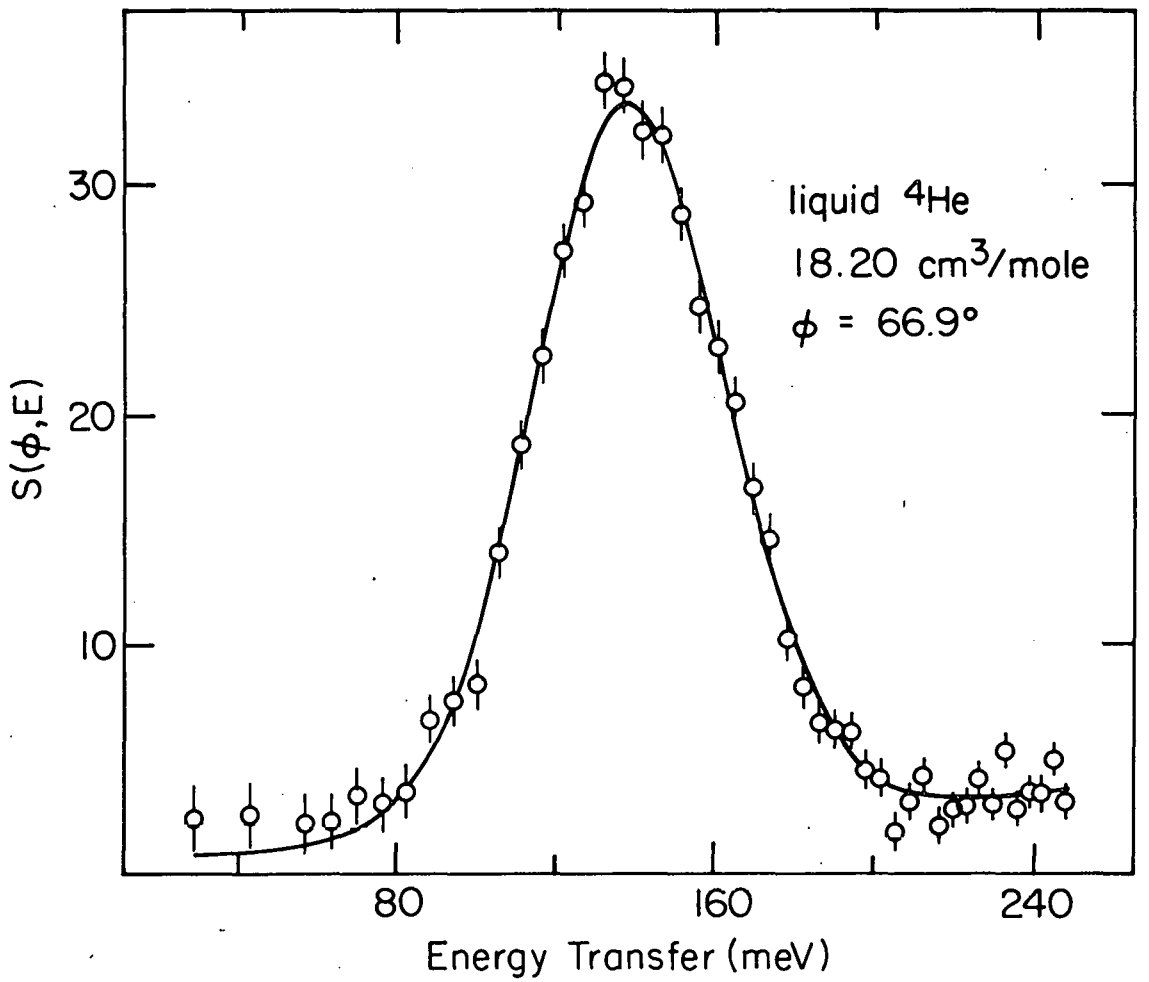

Figure 40. The scattering function derived from data taken at a fixed scattering angle. These data were taken on the liquid sample at a scattering angle of 66.9°.

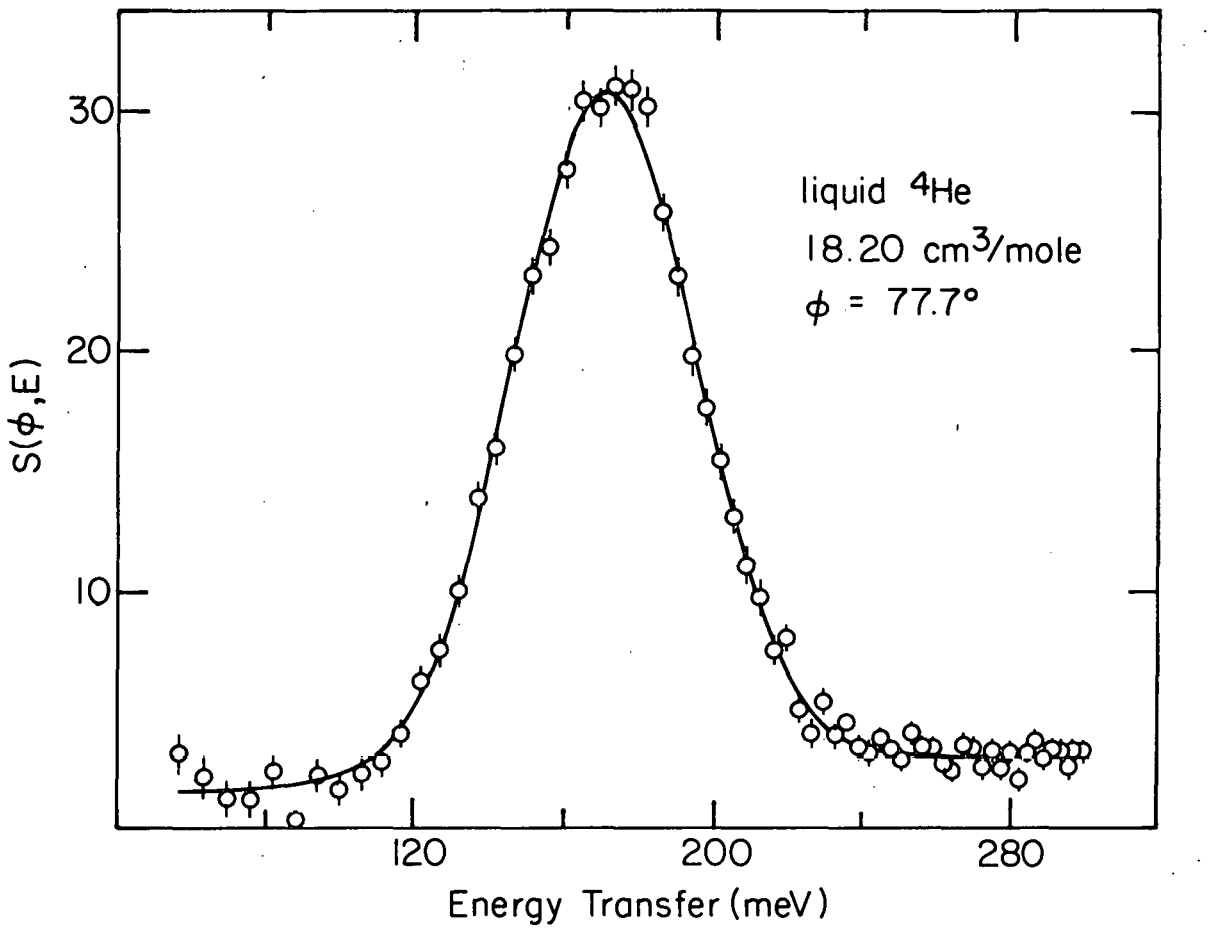

Figure 41. The scattering function derived from data taken at a fixed scattering angle. These data were taken on the liquid sample at a scattering angle of 77.7°.

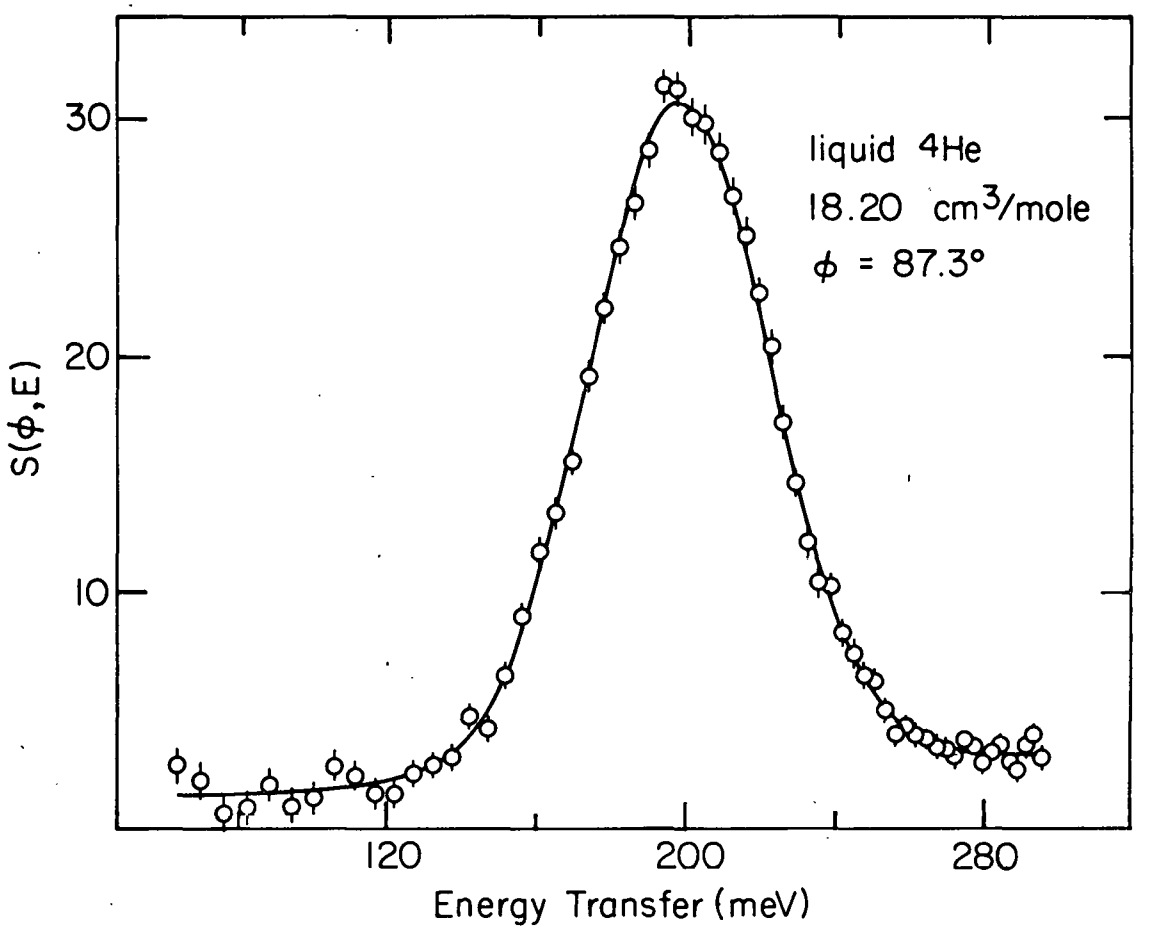

Figure 42. The scattering function derived from data taken at a fixed scattering angle. These data were taken on thc liquid sample at a scattering angle of 87.3°.

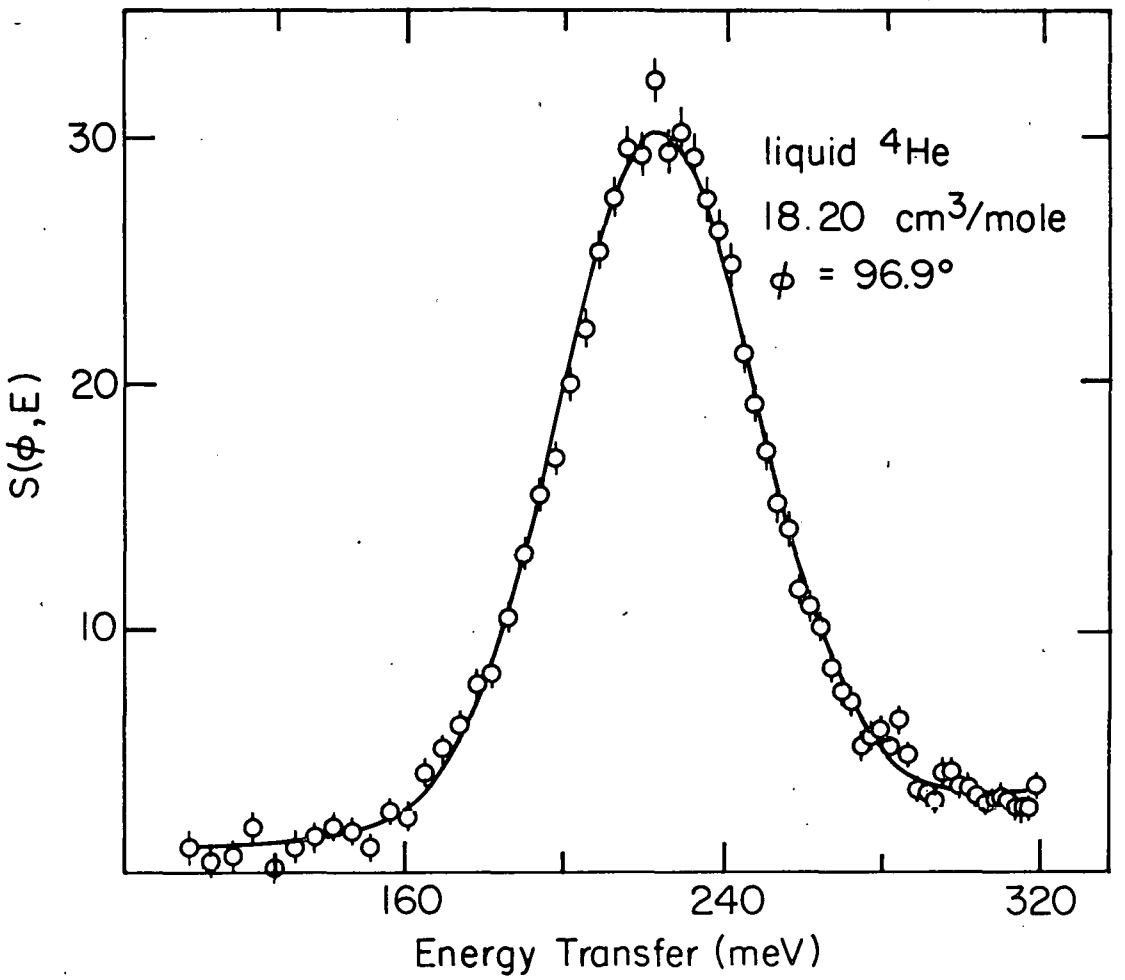

Figure 43. The scattering function derived from data taken at a fixed scattering angle. These data were taken on the liquid sample at a scattering angle of 96.9°.

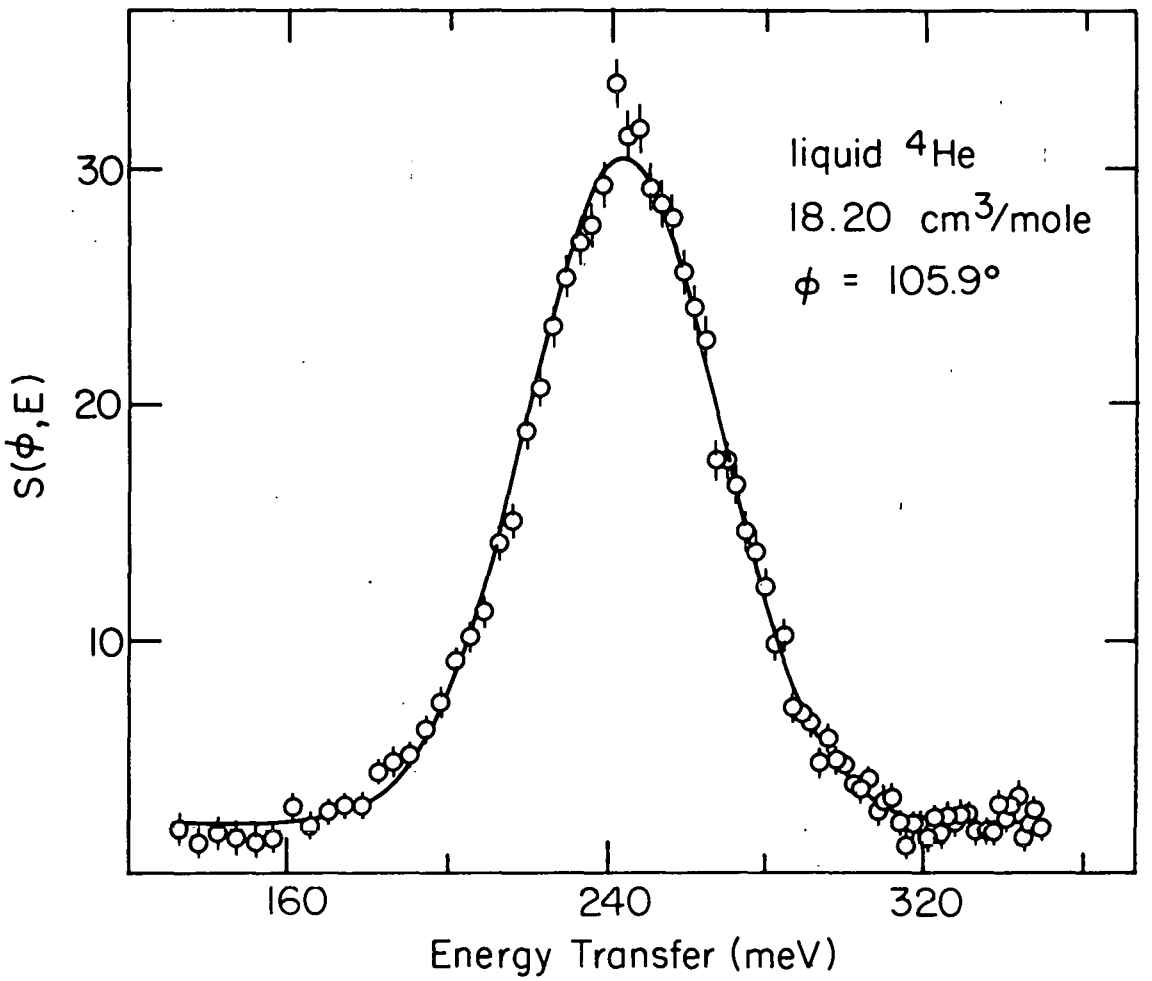

Figure 44. The scattering function derived from data taken at a fixed scattering angle. These data were taken on the liquid sample at a scattering angle of 105.9°.

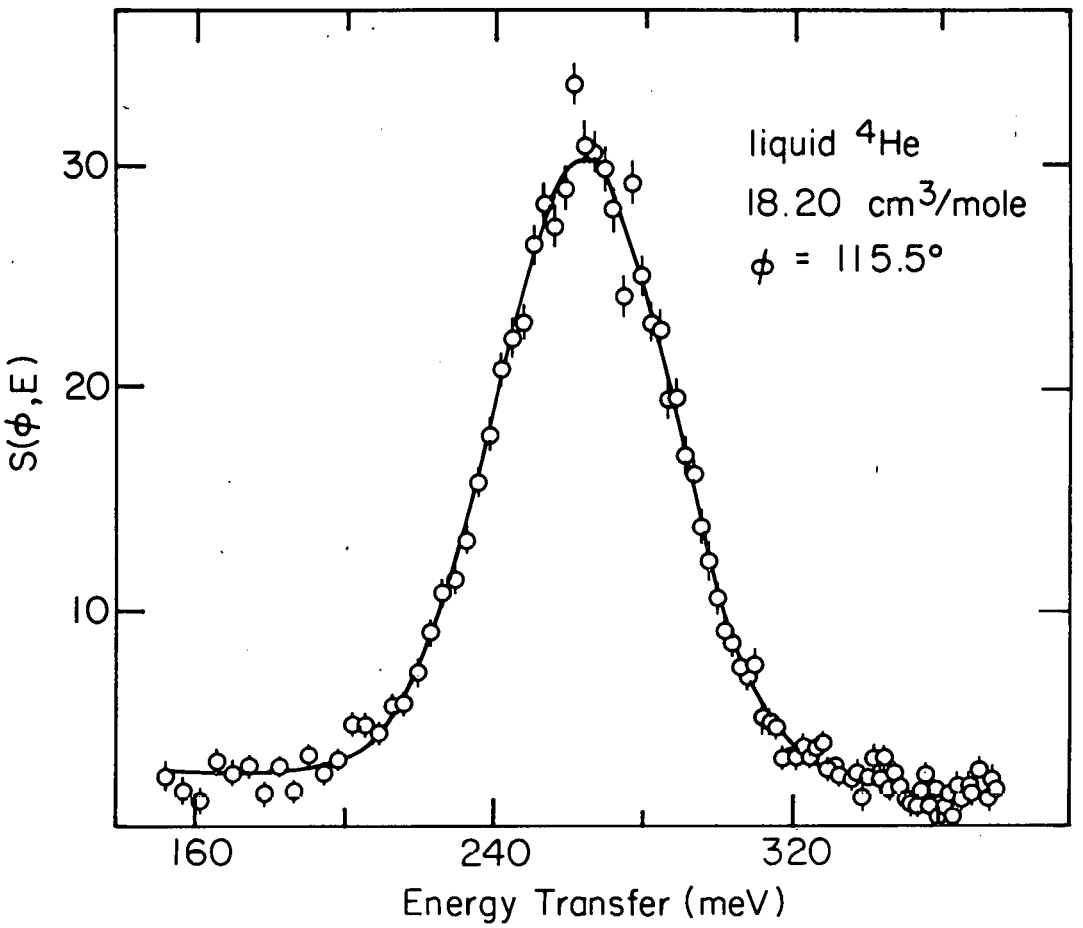

Figure 45. The scattering function derived from data taken at a fixed scattering angle. These data were taken on the liquid sample at a scattering angle of 115.5°.

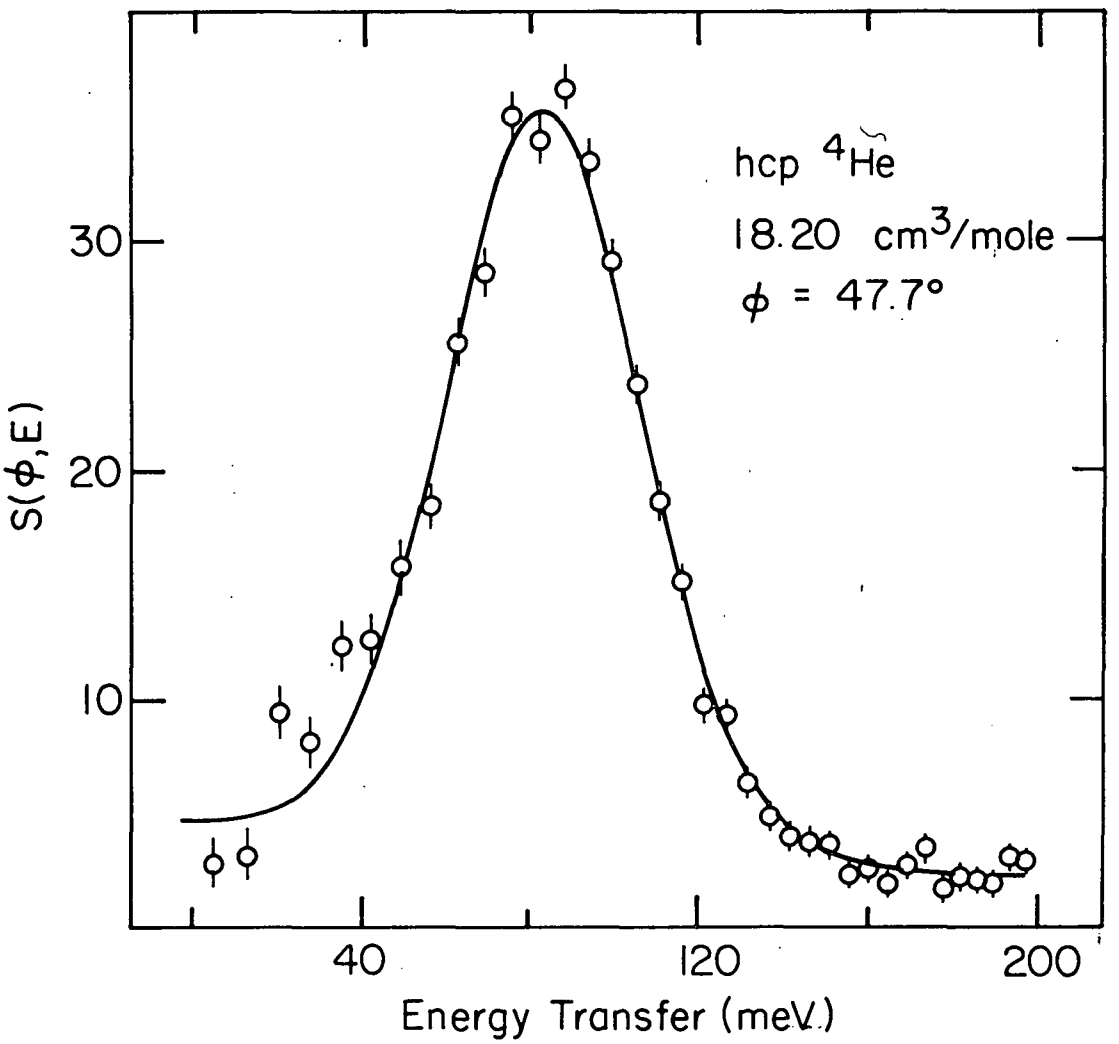

Figure 46. The scattering function derived from data taken at a fixed scattering angle. These data were taken on the high density hcp sample at a scattering angle of 47.7°. The curve is the best fit Gaussian of the form given by Eqn. (32). The spectrometer resolution has not been subtracted from these data.

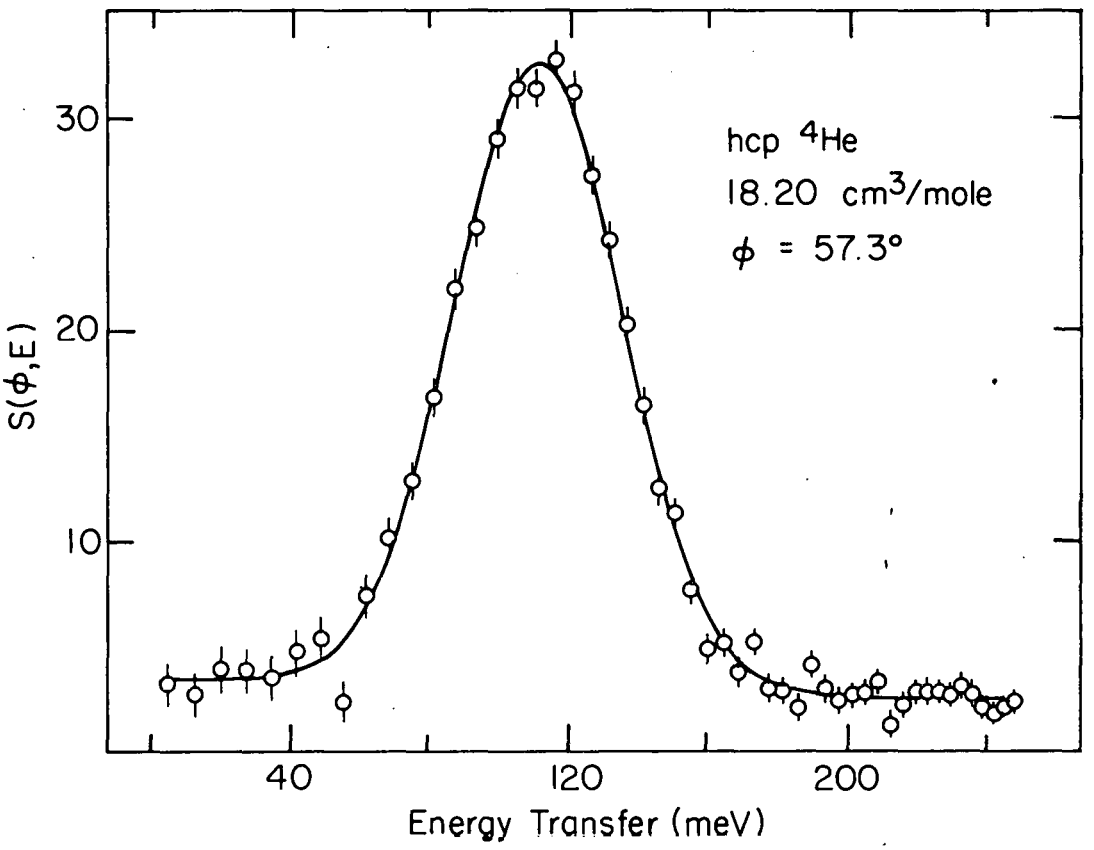

Figure 47. The scattering function derived from data taken at a fixed scattering angle. These data were taken on the high density hcp sample at a scattering angle of 57.3°. The curve is the best fit Gaussian of the form given by Eqn. (32).

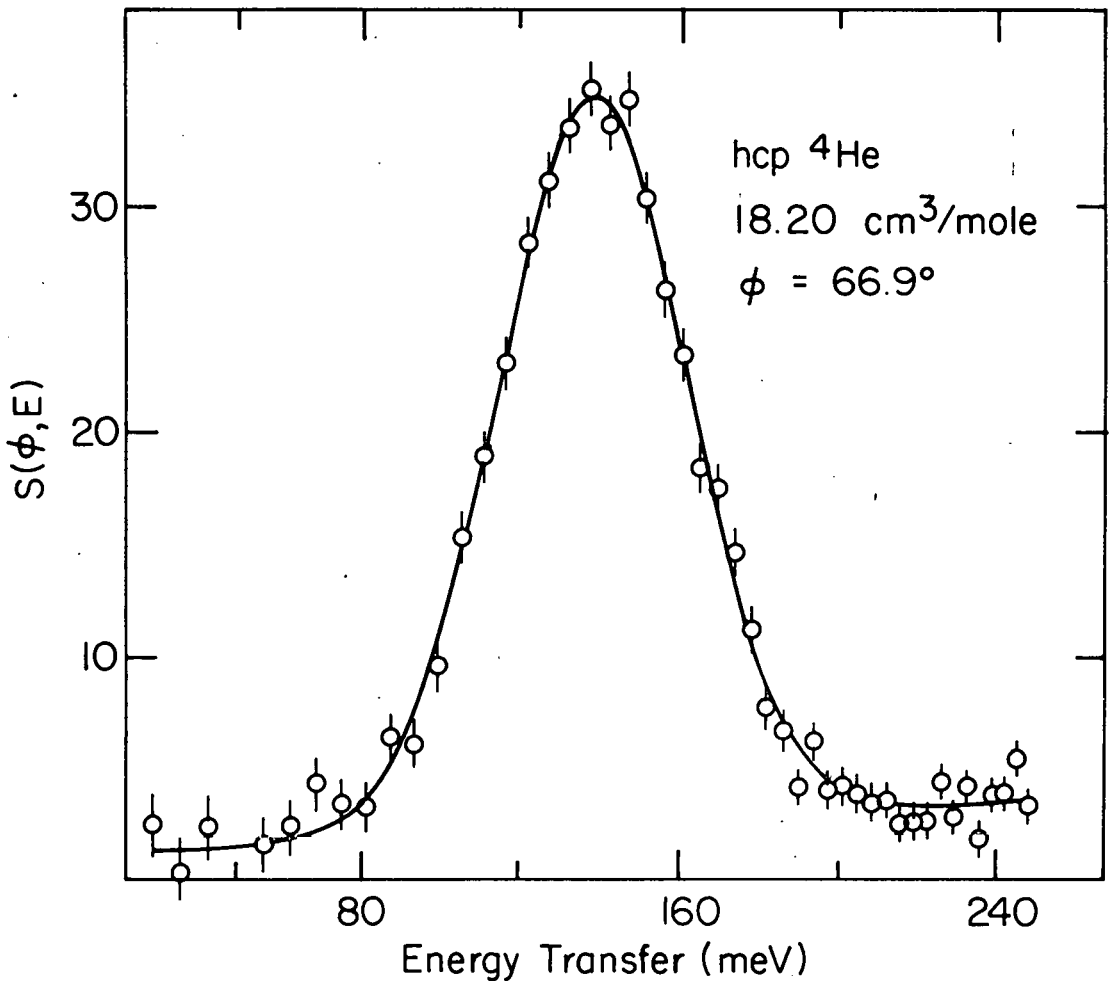

Figure 48. The scattering function derived from data taken at a fixed scattering angle. These data were taken on the high density hcp sample at a scattering angle of 66.9°.

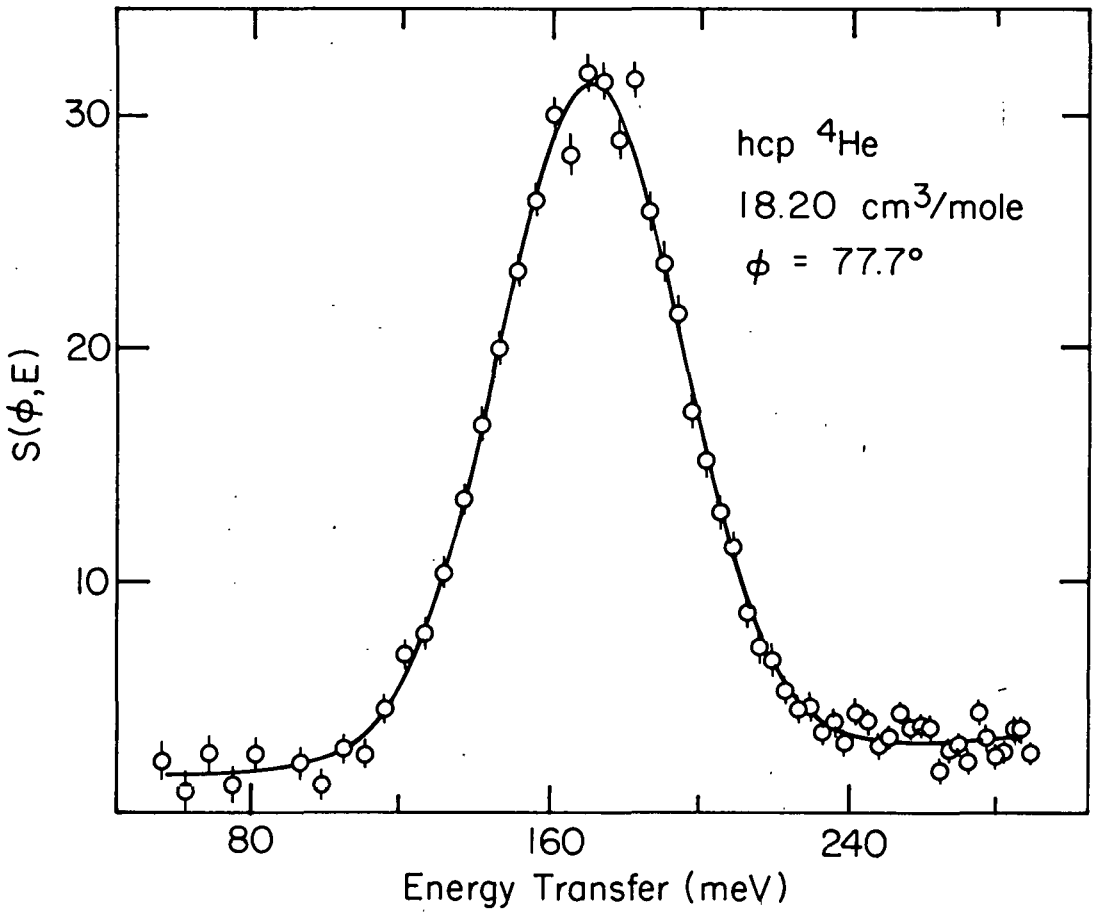

Figure 49. The scattering function derived from data taken at a fixed scattering angle. These data were taken on the high density hcp sample at a scattering angle of 77.7°.

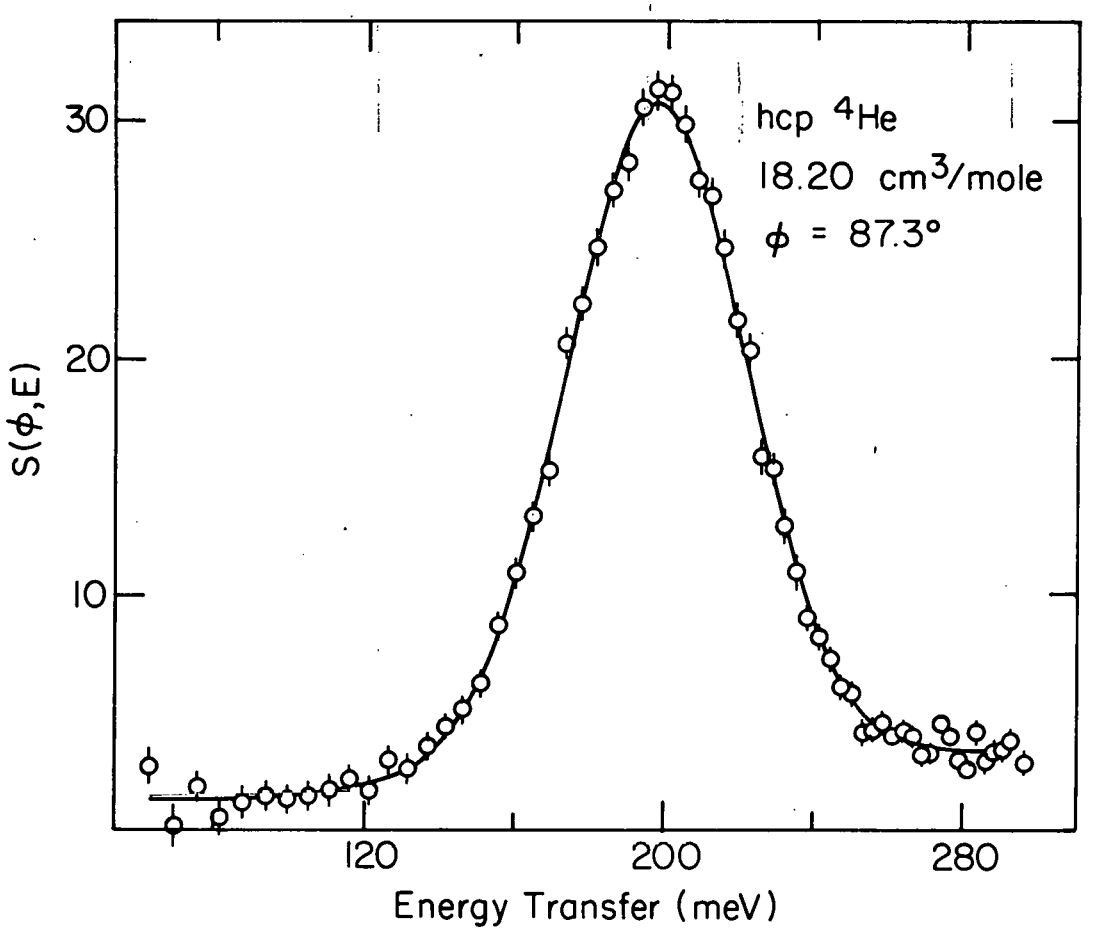

Figure 50. The scattering function derived from data taken at a fixed scattering angle. These data were taken on the high density hcp sample at a scattering angle of 87.3°.

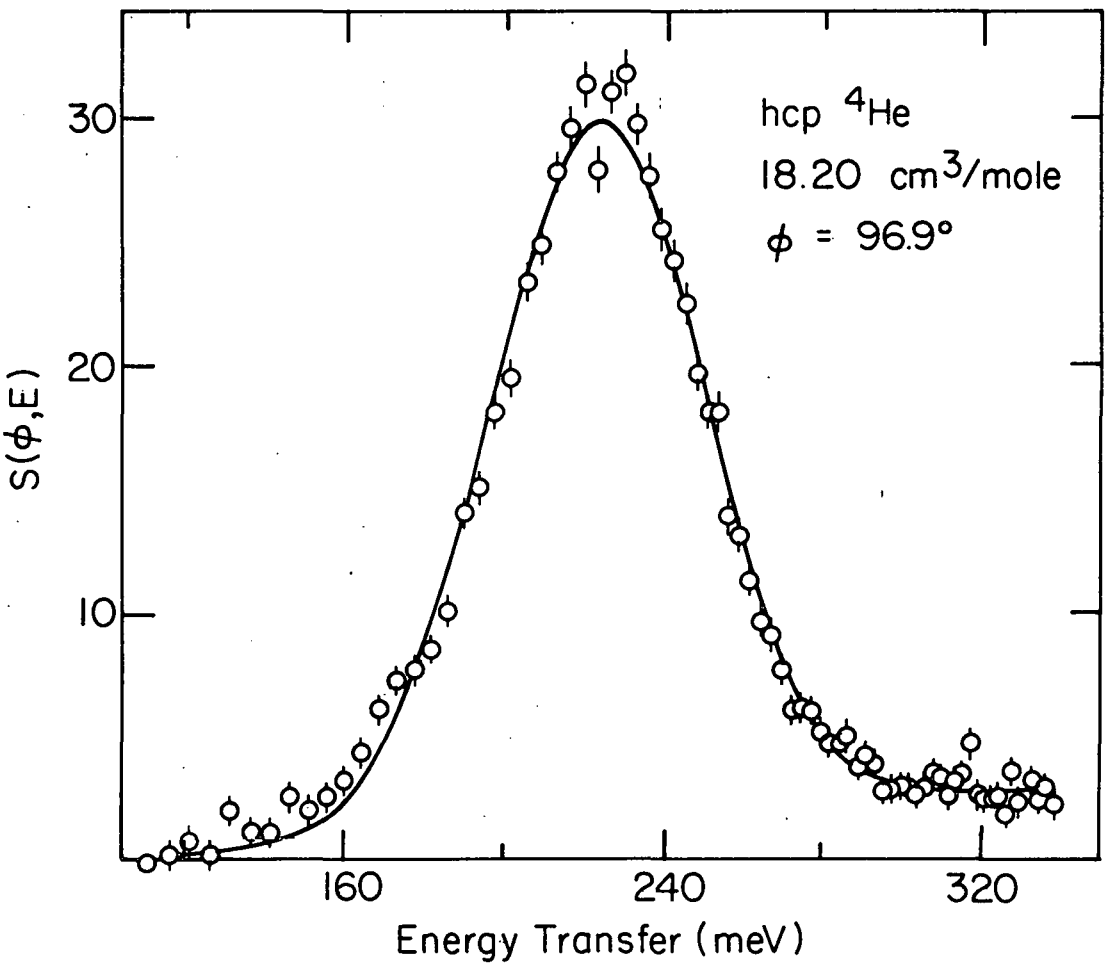

Figure 51. The scattering function derived from data taken at a fixed scattering angle. These data were taken on the high density hcp sample at a scattering angle of 96.9°.

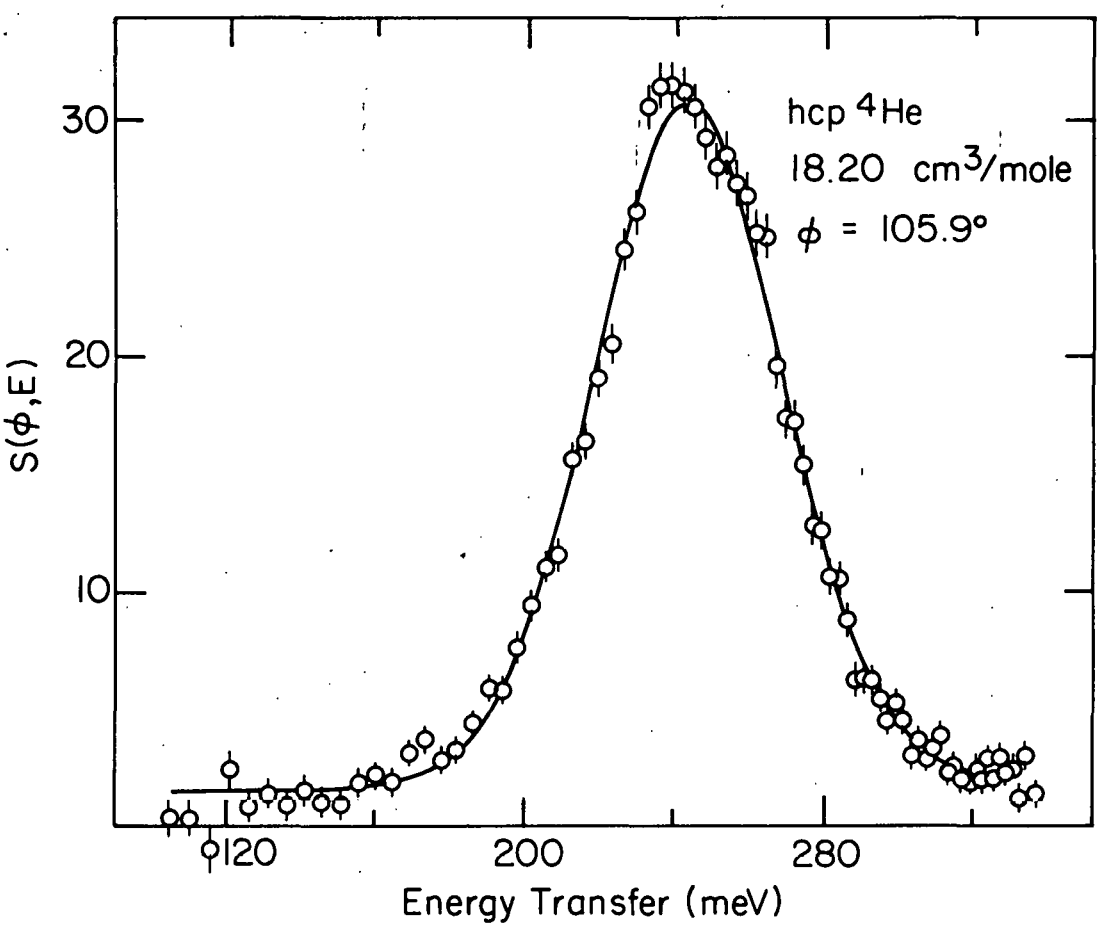

Figure 52. The scattering function derived from data taken at a fixed scattering angle. These data were taken on the high density hcp sample at a scattering angle of 105.9°.

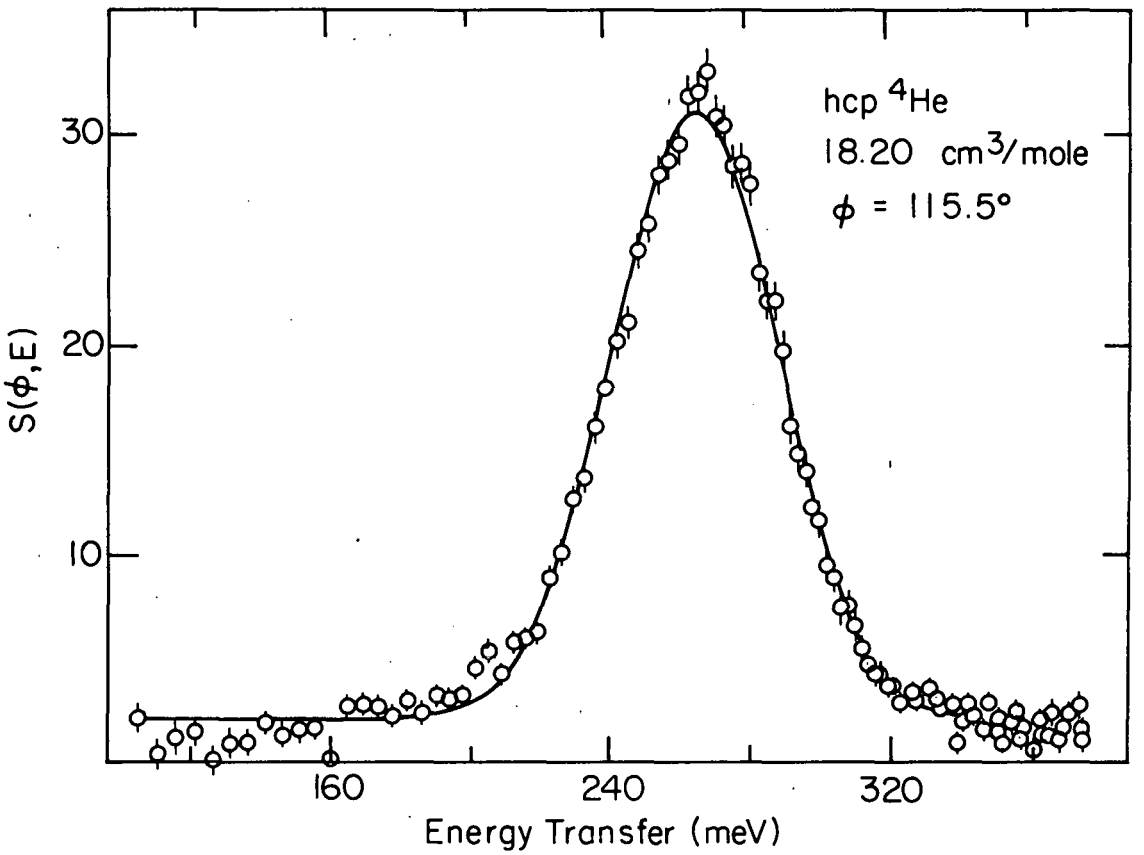

Figure 53. The scattering function derived from data taken at a fixed scattering angle. These data were taken on the high density hcp sample at a scattering angle of 115.5°.

Table 2. Parameters extracted from the data taken on the 19.45 cm^3/mol hcp ^{4}He sample (see Eqn. (32)). The first column contains the eight scattering angles at which data were taken. The second column contains the values of the recoil energy about which the data peaks were centered. The third column contains the standard deviations of the observed $S(\phi,E)$ peaks. Columns four, five and six contain the amplitude and background parameters defined in Eqn. (32). The seventh column contains the Compton defects. The last column contains the standard deviations of the $S(\tilde{Q},E)$ peaks calculated from Eqn. (33).

ϕ (deg)	E_r (meV)	σ_ϕ (meV)	A_1 (meV^{-1})	A_2 (meV^{-1})	A_3 (meV^{-2})	ΔE (meV)	σ_Q (meV)
47.7	83.3	22.1	29.0	5.0	-.015	5.5	17.2
57.3	111.6	21.8	31.8	-1.8	.021	6.0	18.8
66.9	137.8	23.2	34.8	-2.4	.021	2.8	22.4
77.7	170.7	23.6	30.4	0.1	.010	2.9	24.7
87.3	198.4	23.6	28.7	0.7	.008	2.7	26.4
96.9	223.2	24.6	29.1	1.2	.006	1.7	29.5
105.9	243.8	23.0	29.7	2.5	-.001	0.5	28.9
115.5	263.9	22.6	30.2	1.9	-.0002	0.2	29.9

Table 3. Parameters extracted from the data taken on the 18.20 cm^3/mole liquid ^4He sample (see Eqn. (32)). The first column contains the eight scattering angles at which data were taken. The second column contains the values of the recoil energy about which the data peaks were centered. The third column contains the standard deviations of the observed $S(\phi,E)$ peaks. Columns four, five and six contain the amplitude and background parameters defined in Eqn. (32). The seventh column contains the Compton defects. The last column contains the standard deviations of the $S(\tilde{Q},E)$ peaks calculated from Eqn. (33).

ϕ (deg)	E_r (meV)	σ_ϕ (meV)	A_1 (meV^{-1})	A_2 (meV^{-1})	A_3 (meV^{-2})	ΔE (meV)	σ_Q (meV)
47.7	83.9	22.3	29.4	5.4	-.020	6.5	17.5
57.3	112.0	23.1	29.8	0.2	.010	6.4	20.5
66.9	138.6	24.2	31.1	-0.1	.013	3.6	23.6
77.7	171.3	24.4	28.3	0.4	.009	3.5	25.7
87.3	198.7	24.2	27.7	0.5	.008	3.0	27.2
96.9	223.9	24.5	27.5	0.9	.007	2.4	29.3
105.9	244.4	24.1	28.1	2.8	-.002	1.1	30.5
115.5	264.4	23.6	28.3	1.8	0	0.7	31.4

Table 4. Parameters extracted from the data taken on the 18.20 cm^3/mole hcp ^4He sample (see Eqn. (32)). The first column contains the eight scattering angles at which data were taken. The second column contains the values of the recoil energy about which the data peaks were centered. The third column contains the standard deviations of the observed $S(\phi,E)$ peaks. Columns four, five and six contain the amplitude and background parameters defined in Eqn. (32). The seventh column contains the Compton defects. The last column contains the standard deviations of the $S(\vec{Q},E)$ peaks calculated from Eqn. (33).

ϕ (deg)	E_r (meV)	ϕ_ϕ (meV)	A_1 (meV^{-1})	A_2 (meV^{-1}	A_3 (meV^{-2}	ΔE (meV)	σ_Q (meV)
47.7	82.2	23.1	29.8	2.2	-.001	5.4	18.7
57.3	111.5	23.9	29.8	.9	.004	5.9	21.6
66.9	137.9	23.5	32.9	1.4	.010	2.9	22.7
77.7	170.4	24.2	29.0	.7	.008	2.6	25.5
87.3	197.8	24.0	28.1	.6	.008	2.1	27.0
96.9	223.1	25.8	27.7	-.4	.014	1.6	31.1
105.9	243.5	24.8	28.9	.5	.008	0.2	31.4
115.5	264.3	23.3	29.4	4.9	-.013	0.6	31.0

included in the tables because they are not independent of the other fitting parameters.

Several fitting routines were used; they all worked by searching for the parameters that give the lowest value for chi squared. All the fitting routines gave essentially the same results for the parameters. The quoted uncertainty in each parameter is given, for proper normalization of chi squared, by the amount by which the parameter must be changed to make a change in chi squared of one.[51]

As was discussed in Chapter 4, neutron spectroscopic data were taken on a room temperature vanadium foil sample. Because the vanadium was not in a sample container, the background was much lower than in the measurement on helium. The raw data were converted to $S(\phi,E)$ and four of these are shown in Figures 54 through 57. These data were used to evaluate the spectrometer's resolution (see discussion in Chapter 3), and to normalize the scattering from the helium samples (see discussion of Eqn. (31)).

B. Determination of $S(\vec{Q},E)$

As discussed in Chapter 2, when data are taken at a fixed angle, $S(\vec{Q},E)$ can be extracted from the data by interpolating the $S(\phi,E)$ data. This has been done for all of our data sets. The resultant $S(\vec{Q},E)$ data and their corresponding Gaussian fits are shown in Figures 59 through 77. In these figures, the circles are the values of $S(\vec{Q},E)$

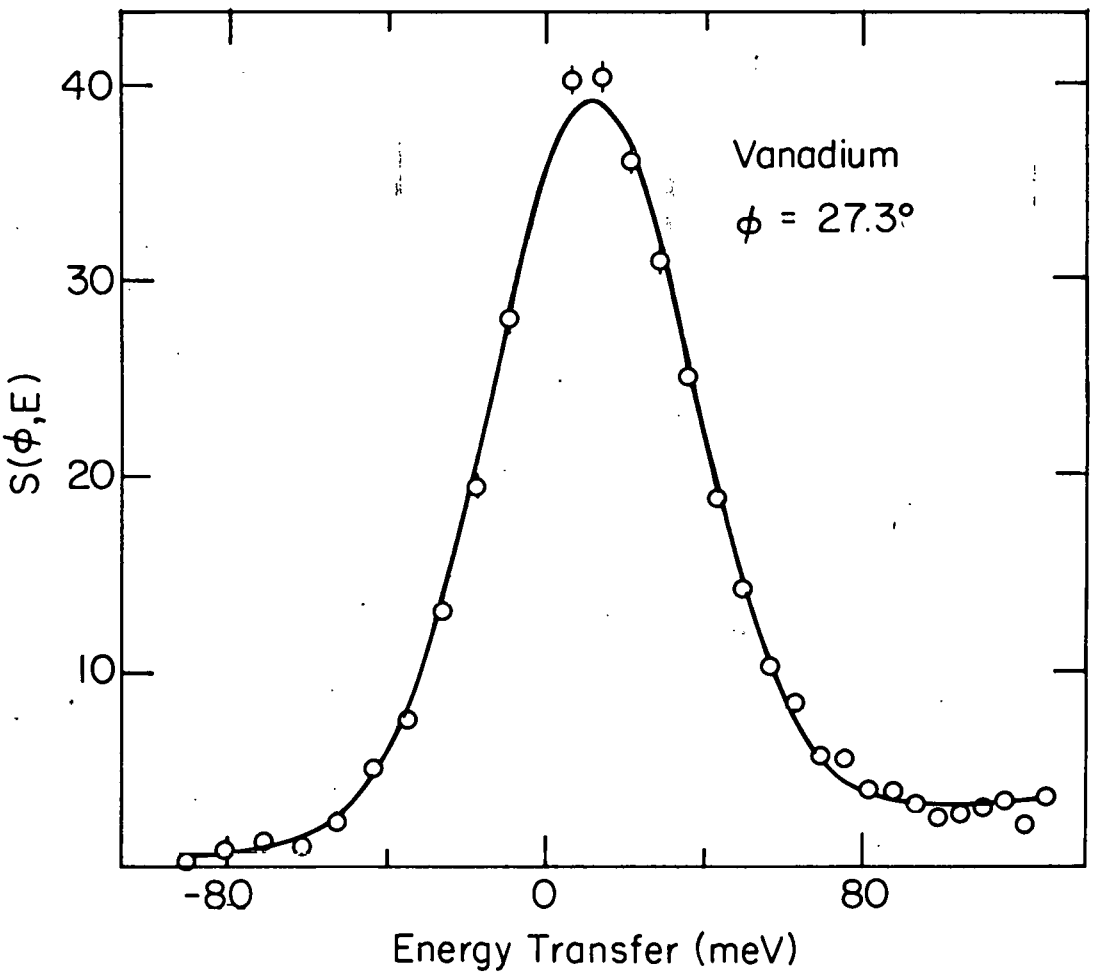

Figure 54. The scattering function at fixed scattering angle for the vanadium foil. These data were used to determine experimentally the spectrometer resolution and to normalize the scattering from the helium samples. The curve is the best fit Gaussian of the form given by Eqn. (32).

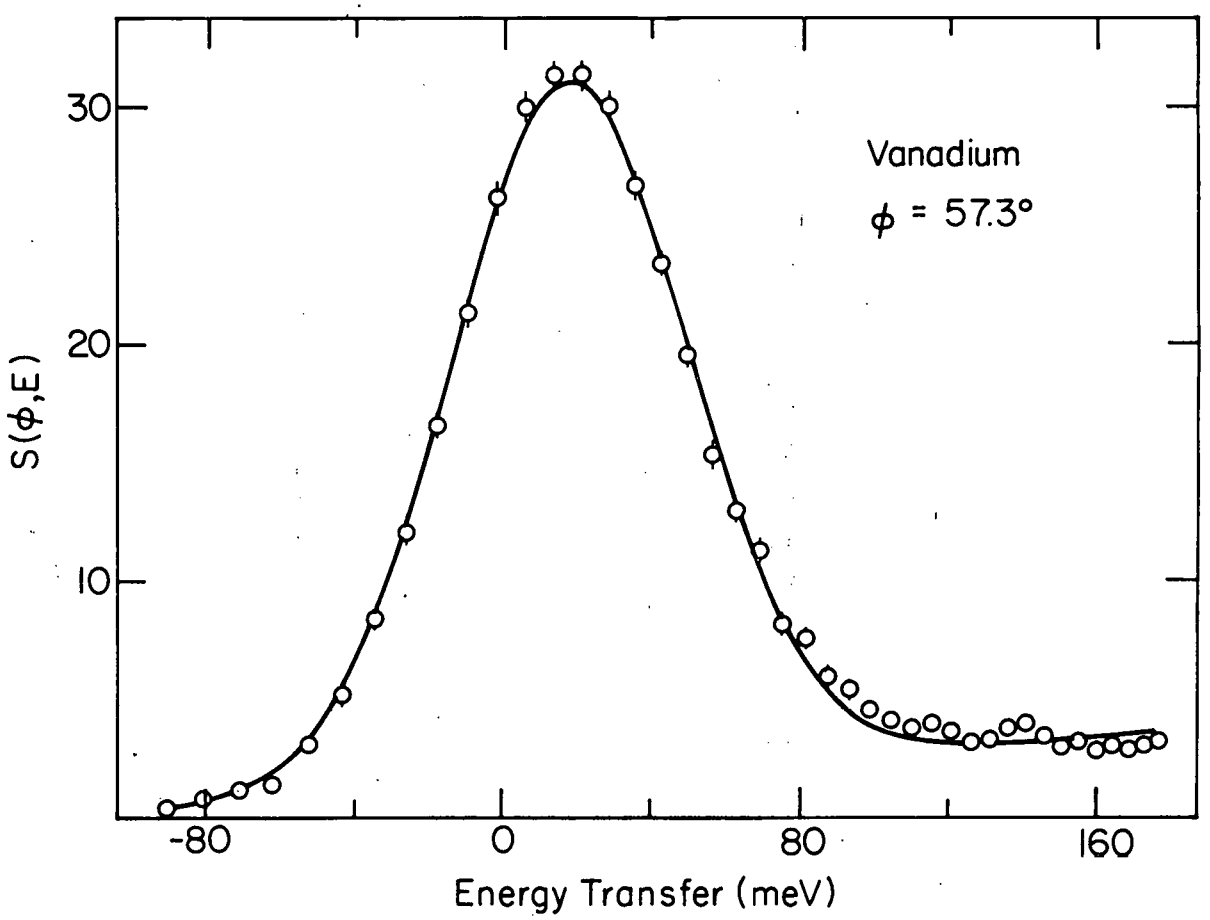

Figure 55. The scattering function at fixed scattering angle for the vanadium foil. These data were used to determine experimentally the spectrometer resolution and to normalize the scattering from the helium samples. The curve is the best fit Gaussian of the form given by Eqn. (32).

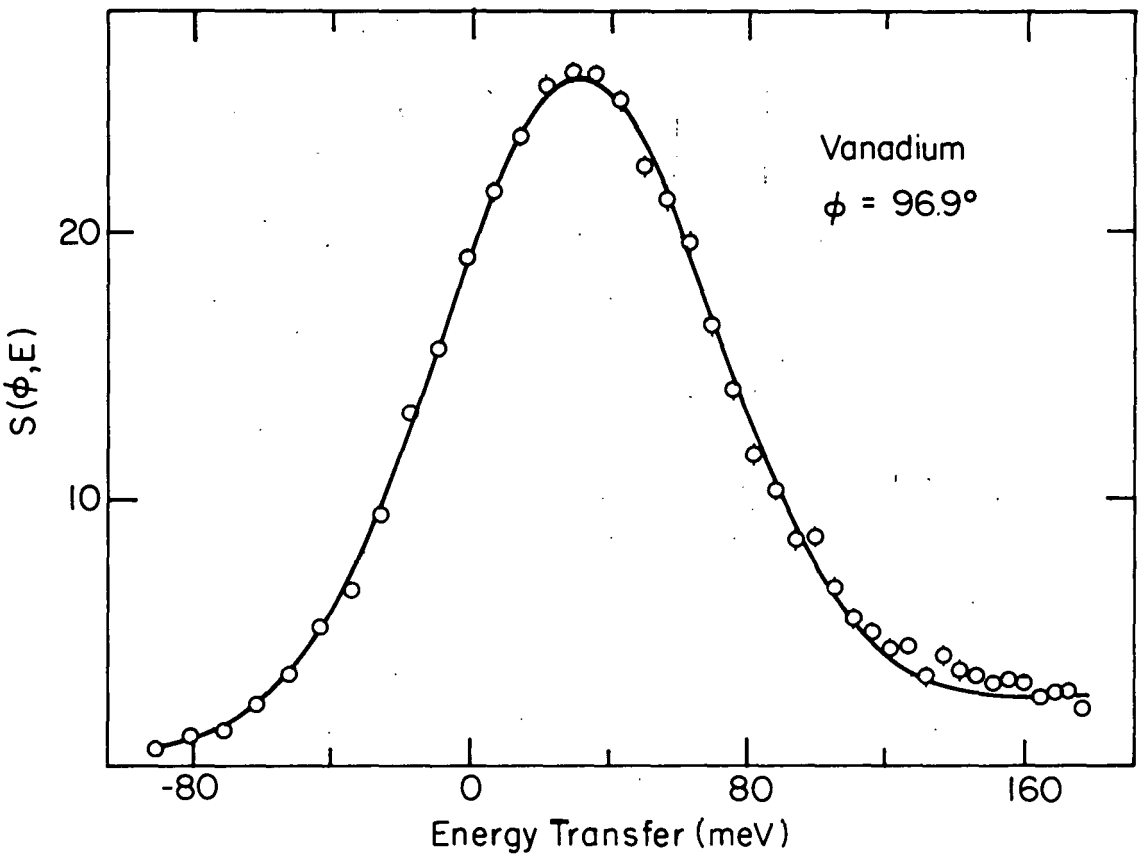

Figure 56. The scattering function at fixed scattering angle for the vanadium foil. These data were used to determine experimentally the spectrometer resolution and to normalize the scattering from the helium samples. The curve is the best fit Gaussian of the form given by Eqn. (32).

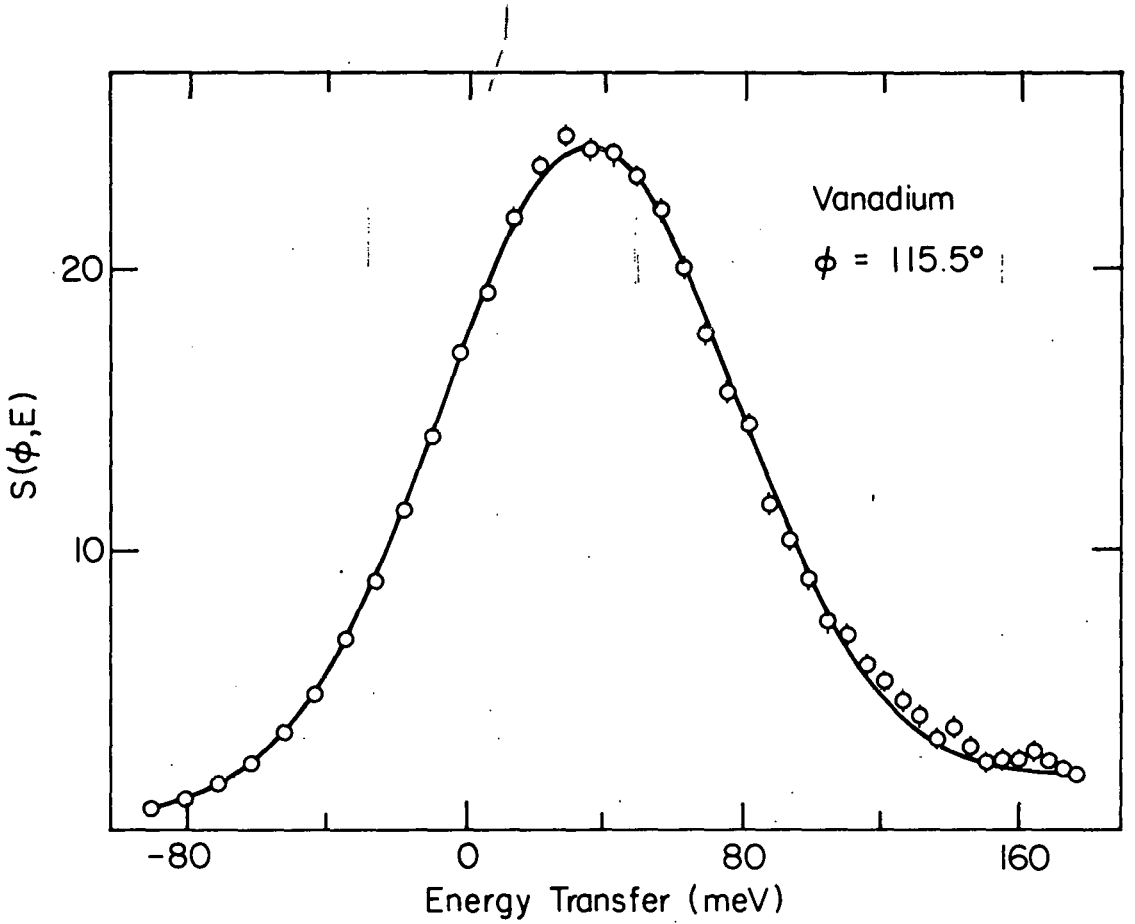

Figure 57. The scattering function at fixed scattering angle for the vanadium foil. These data were used to determine experimentally the spectrometer resolution and to normalize the scattering from the helium samples. The curve is the best fit Gaussian of the form given by Eqn. (32).

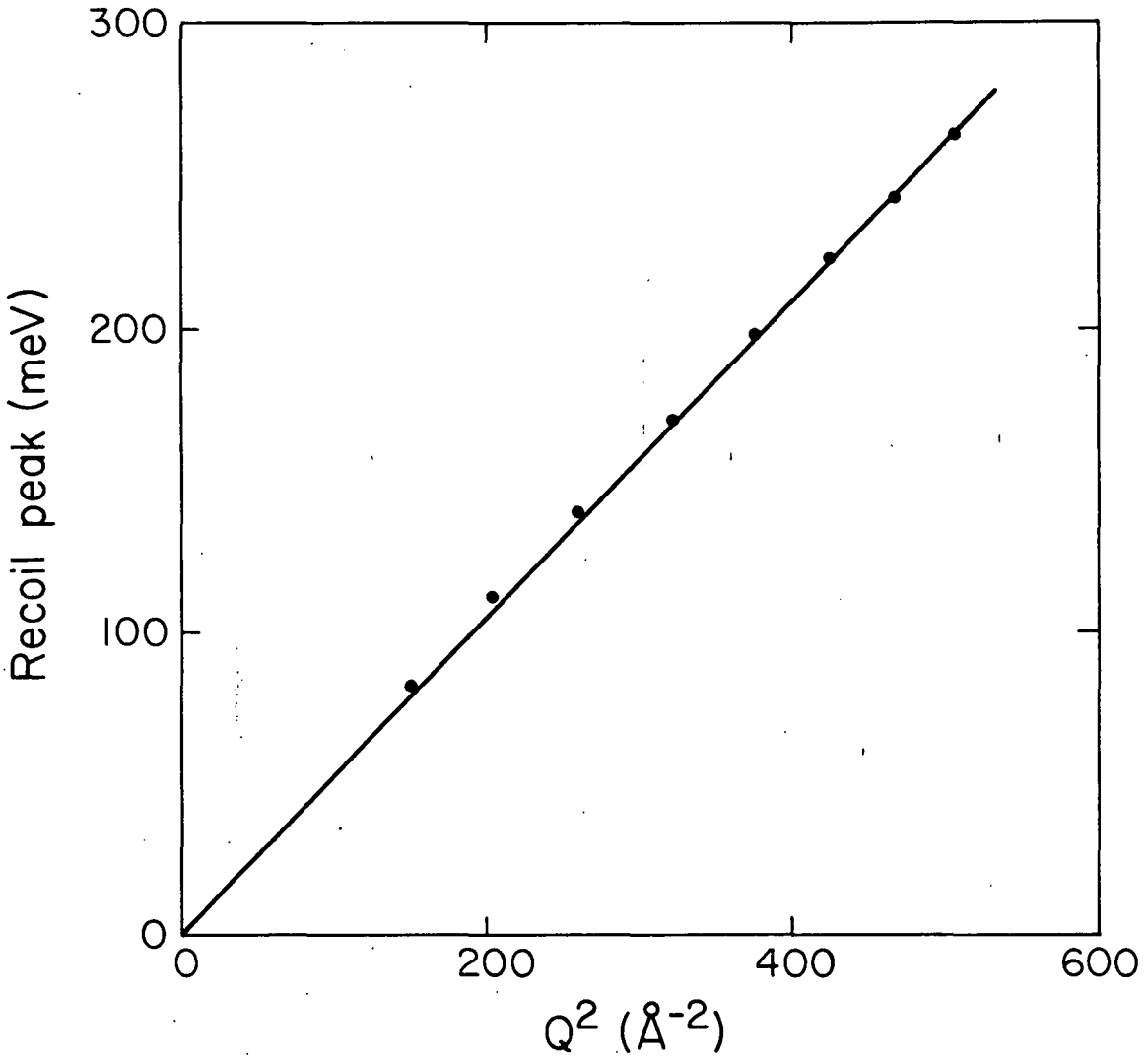

Figure 58. The mean energy transfer versus momentum transfer squared. If the impulse approximation assumptions are valid and the neutrons interact with only single helium nuclei as if they were free particles, the energy transfer should be proportional to the square of the momentum transfer (Eqn. (17)). The points represent the energy and momentum transfer for scattering at the eight scattering angles. The size of the points is the uncertainty; the data points for the three samples lie within the uncertainties. The straight line is a plot of Eqn. (17) with the mass equal to the ^{4}He atomic mass. The smaller-Q points lie above the line by an amount related to the ^{4}He binding energy (see text). At even smaller Q, cooperative motion of neighboring atoms cause the points to fall below the line.

interpolated from the $S(\phi,E)$ data sets; the uncertainty in each data point is indicated by the error bar. The same form of the fitting function used for $S(\phi,E)$ was used to fit the $S(\vec{Q},E)$ data (see Equation (32)). Figures 59 through 67 correspond to the low density solid sample, Figures 68 through 77 correspond to the liquid sample, no $S(\vec{Q},E)$ plots are shown for the high density solid for the sake of brevity.

Interpolating the $S(\phi,E)$ data to get $S(\vec{Q},E)$ was not an essential step in the data analysis; the interpolation was carried out for several reasons. The first was to check the validity of the relationship given in Equation (25) which relates the variance of a $S(\phi,E)$ peak to the variance of the corresponding $S(\vec{Q},E)$ peak. We also wanted to check for deviation of the $S(\vec{Q},E)$ peak from Gaussian line shape. Because the conversion from $S(\phi,E)$ to $S(\vec{Q},E)$ and subsequently fitting $S(\vec{Q},E)$ to a Gaussian involves several additional data analysis steps, and because each step introduces more uncertainty into the calculation, we felt that this conversion could be done with a smaller uncertainty using Equation (25).

Equation (25) gives the relationship between σ_ϕ and σ_Q, but does not include the effects of the spectrometer resolution. Because the resolution function is convoluted with the actual $S(\vec{Q},E)$ peak to result in the observed $S(\vec{Q},E)$ peak, the resolution must be subtracted

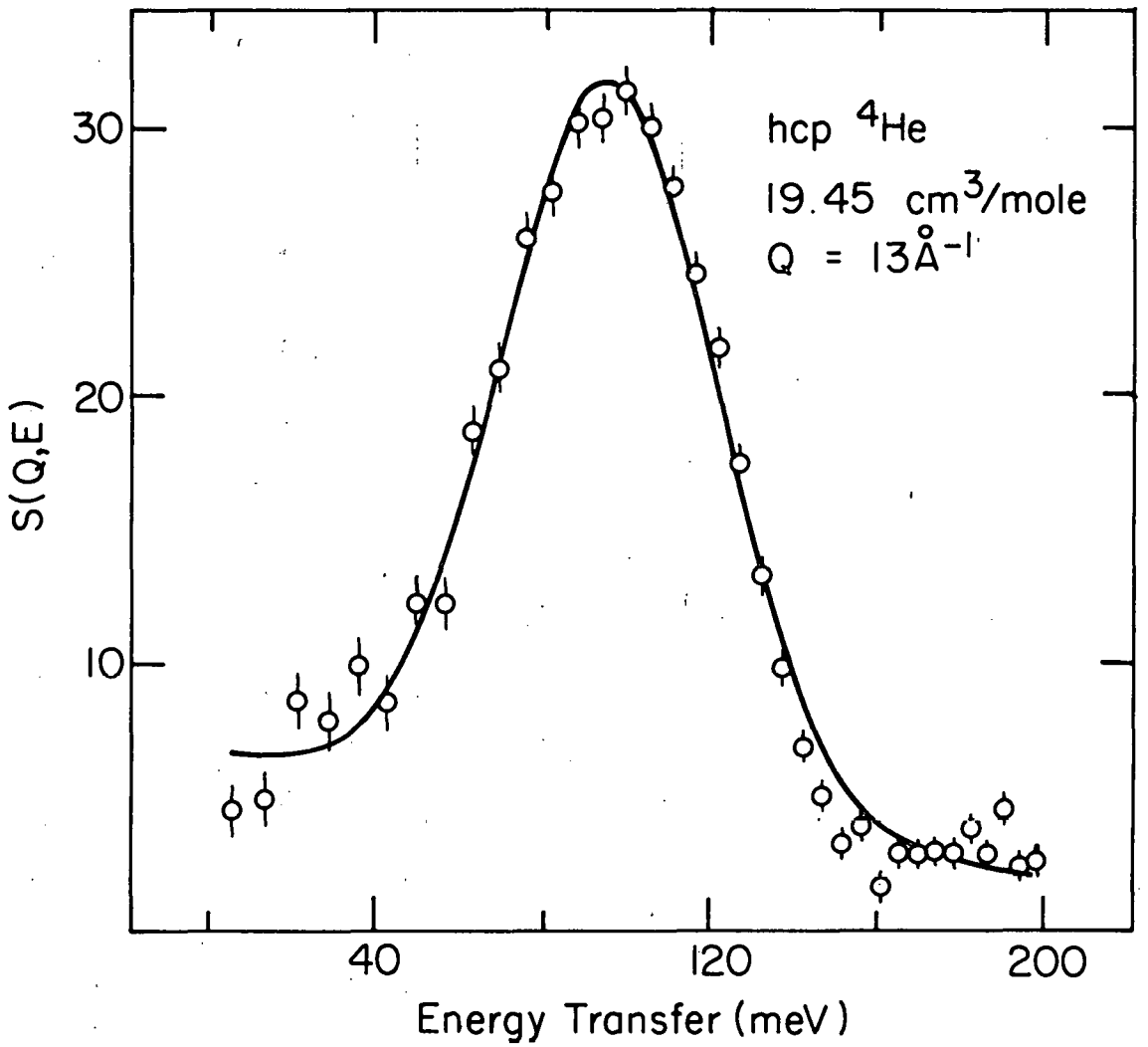

Figure 59. The dynamic structure factor versus energy transfer. These data represent $S(\vec{Q},E)$ interpolated to $Q = 13$ Å^{-1} for the low density hcp ^{4}He sample; the uncertainty in each point is indicated. The curve is the best fit Gaussian of the form given in Eqn. (32).

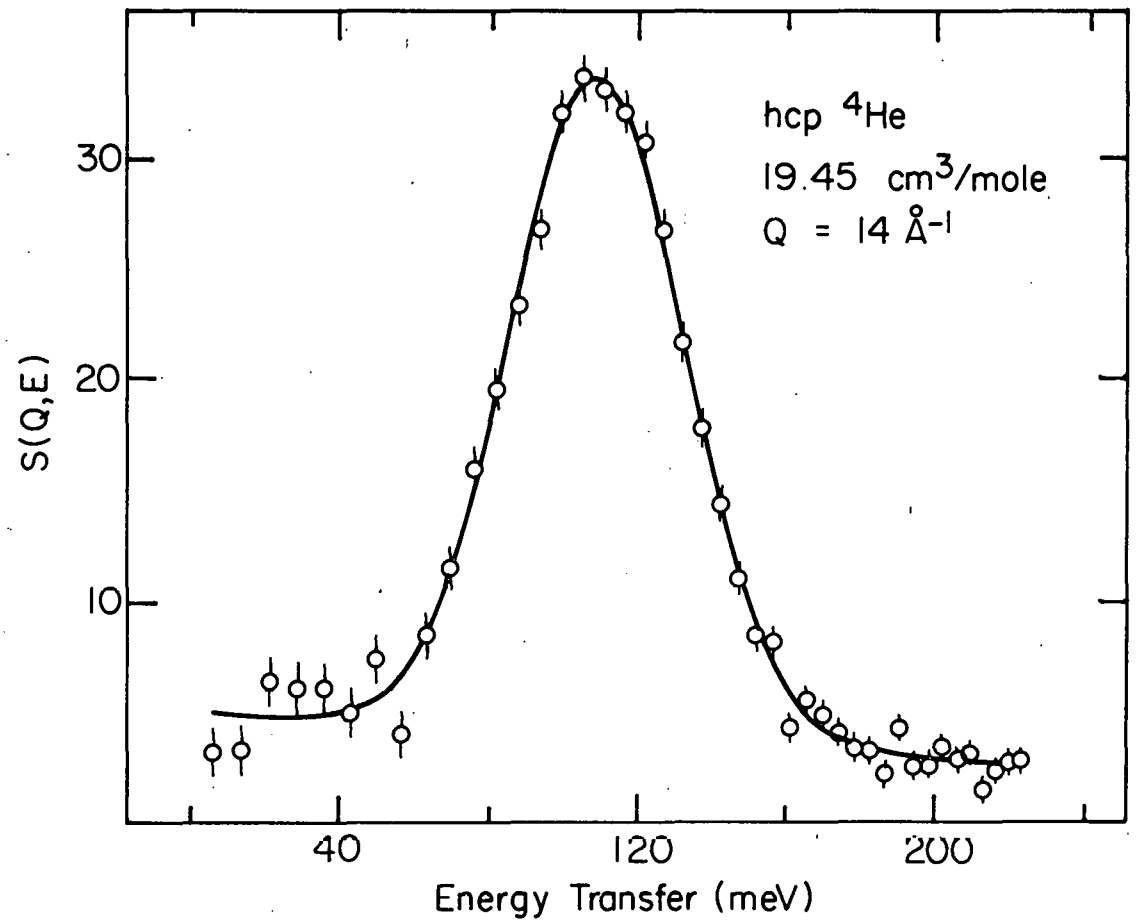

Figure 60. The dynamic structure factor versus energy transfer. These data represent $S(\vec{Q},E)$ interpolated to $Q = 14$ Å^{-1} for the low density hcp ^{4}He sample; the uncertainty in each point is indicated. The curve is the best fit Gaussian of the form given in Eqn. (32).

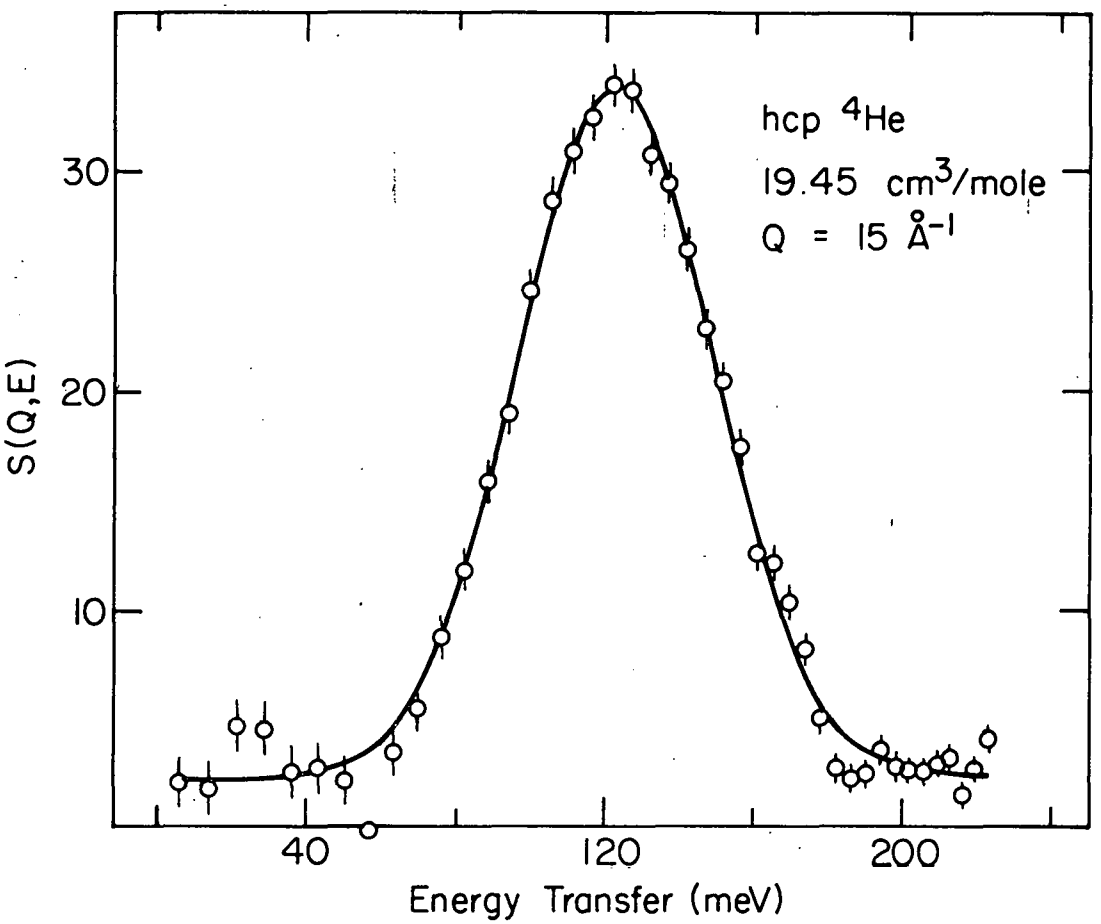

Figure 61. The dynamic structure factor versus energy transfer. These data represent $S(\vec{Q},E)$ interpolated to $Q = 15$ Å^{-1} for the low density hcp ^{4}He sample; the uncertainty in each point is indicated.

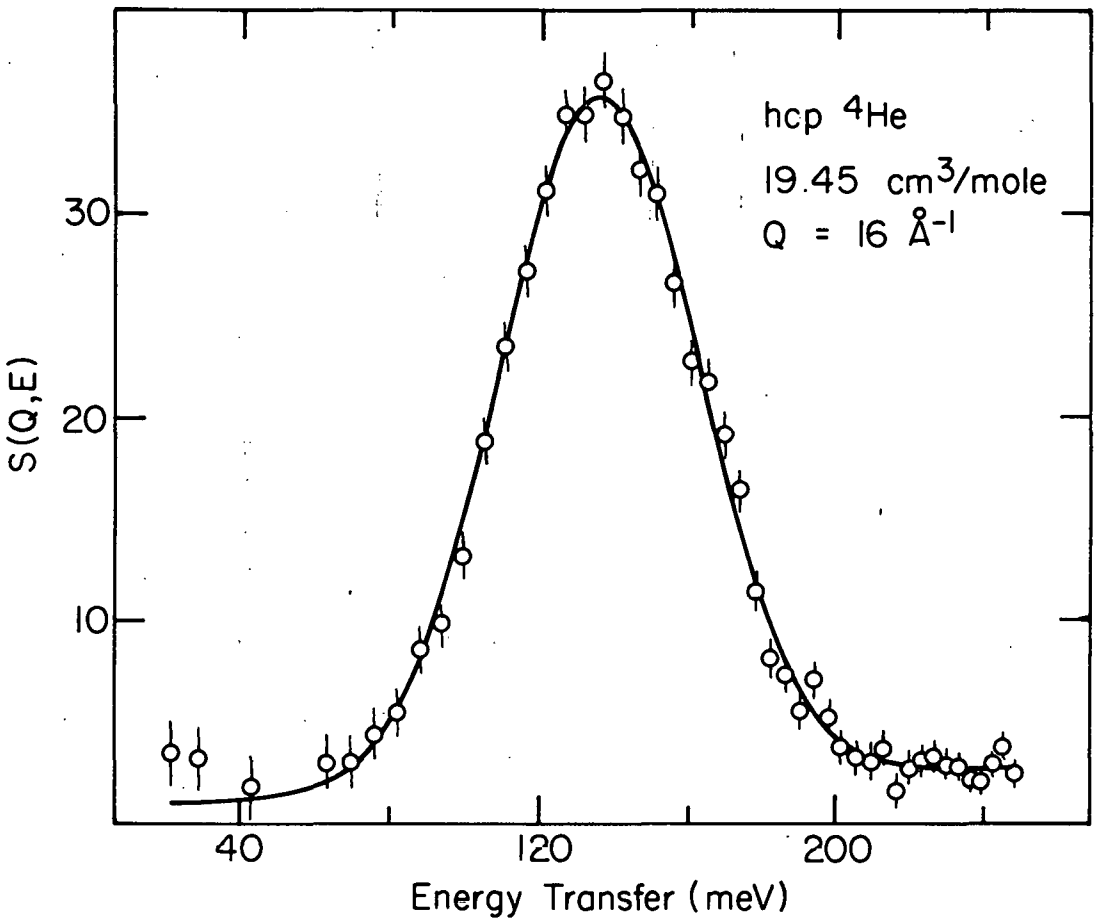

Figure 62. The dynamic structure factor versus energy transfer. These data represent $S(\vec{Q},E)$ interpolated to $Q = 16$ Å^{-1} for the low density hcp ^{4}He sample.

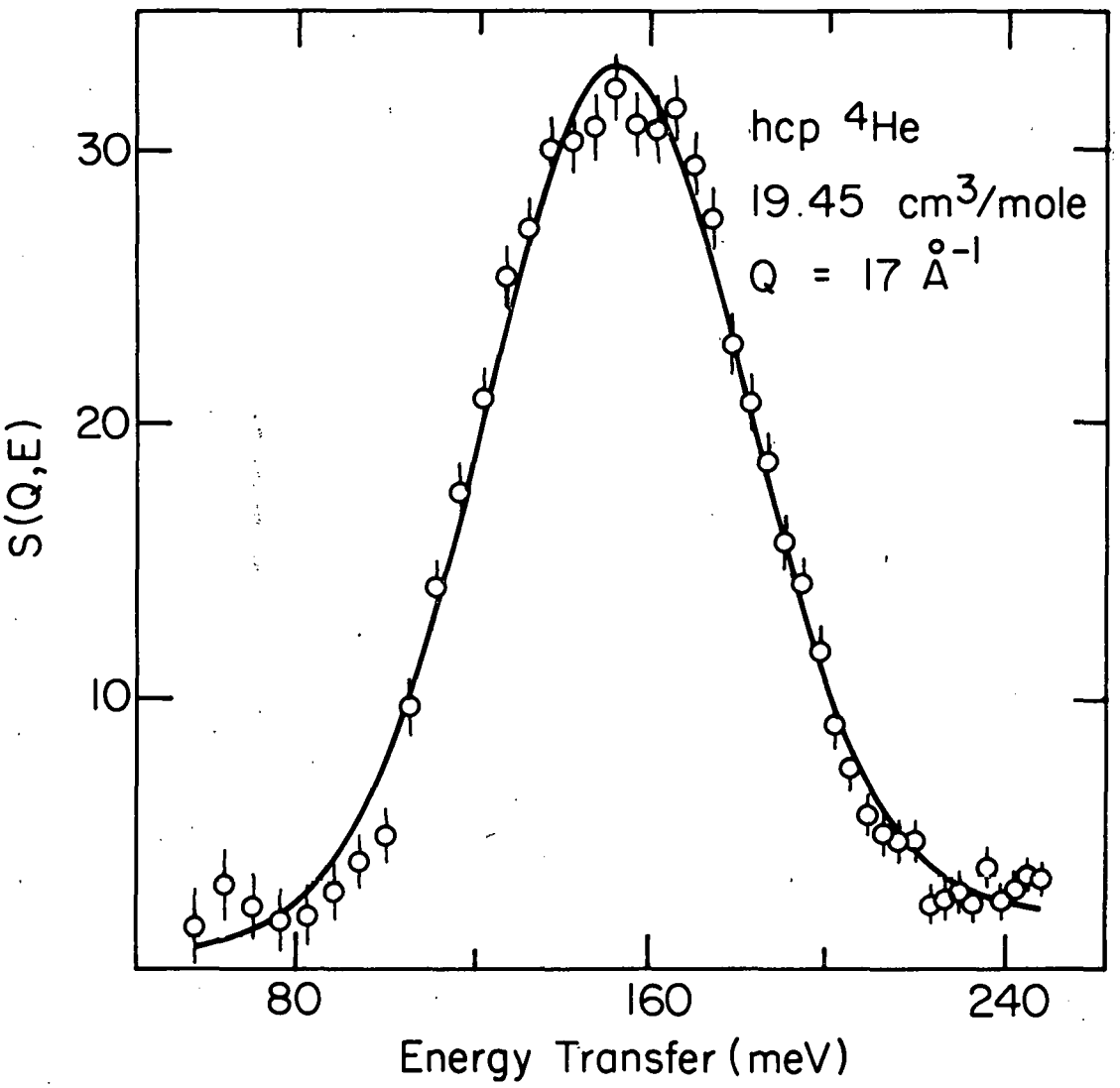

Figure 63. The dynamic structure factor versus energy transfer. These data represent $S(\vec{Q},E)$ interpolated to $Q = 17$ Å^{-1} for the low density hcp ^{4}He sample.

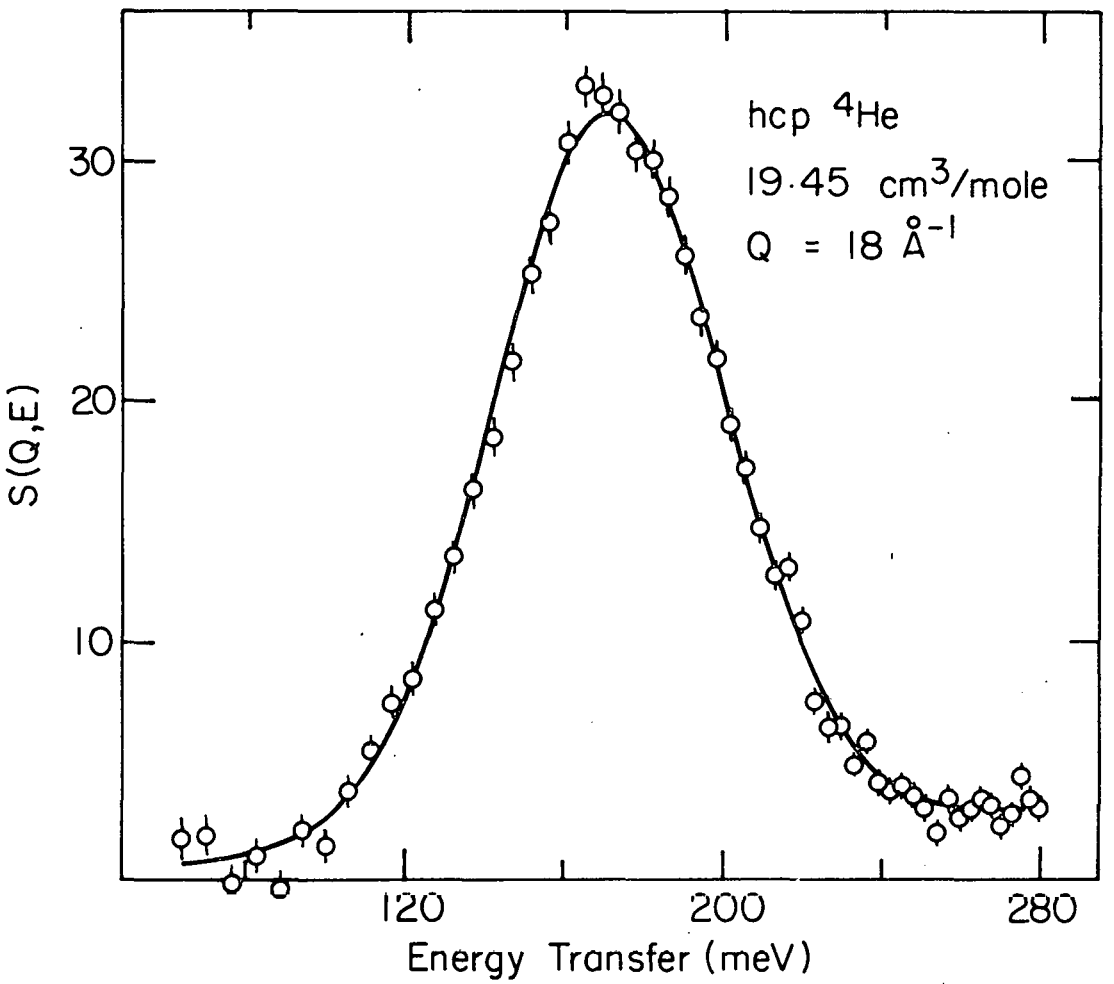

Figure 64. The dynamic structure factor versus energy transfer. These data represent $S(\vec{Q},E)$ interpolated to $Q = 18$ Å^{-1} for the low density hcp ^{4}He sample.

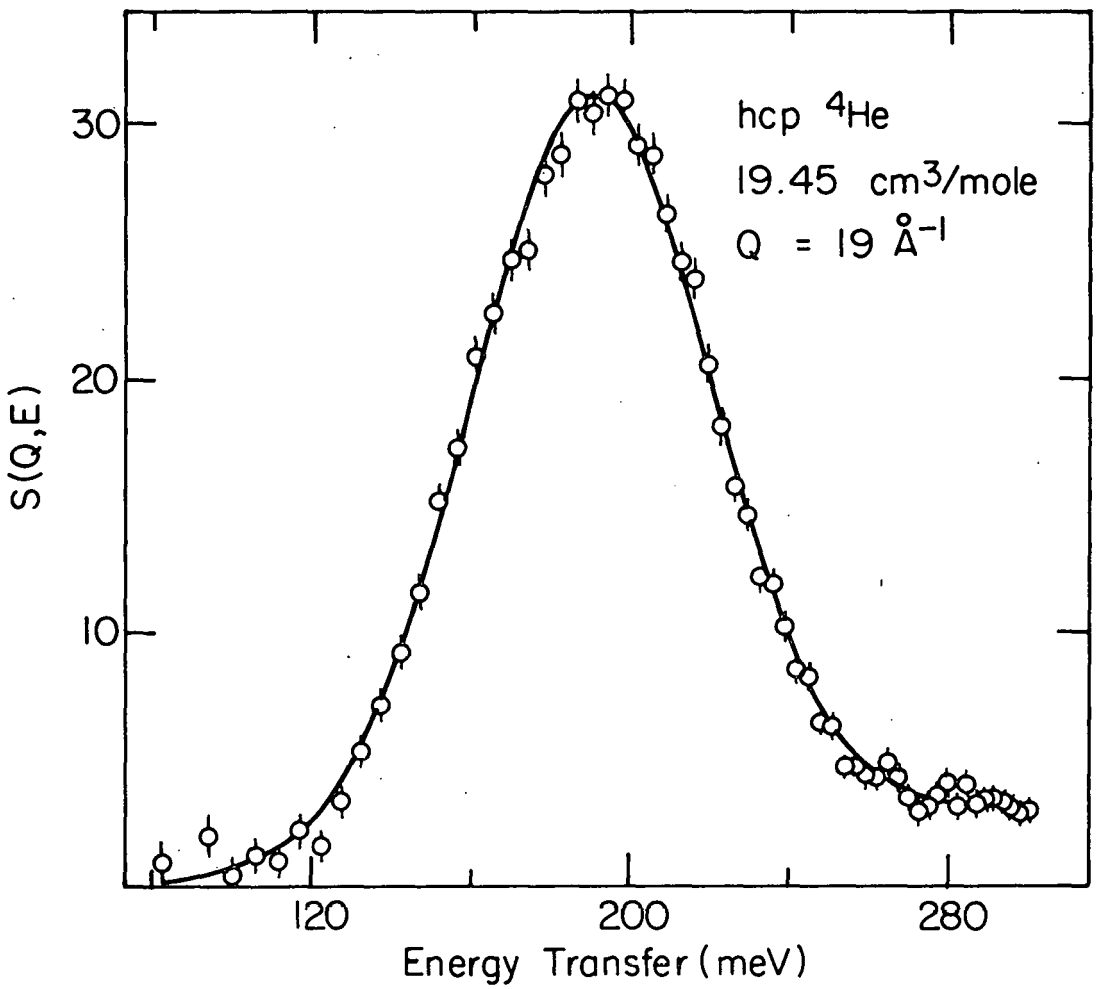

Figure 65. The dynamic structure factor versus energy transfer. These data represent S(Q,E) interpolated to Q=19 Å^{-1} for the low density hcp ^{4}He sample.

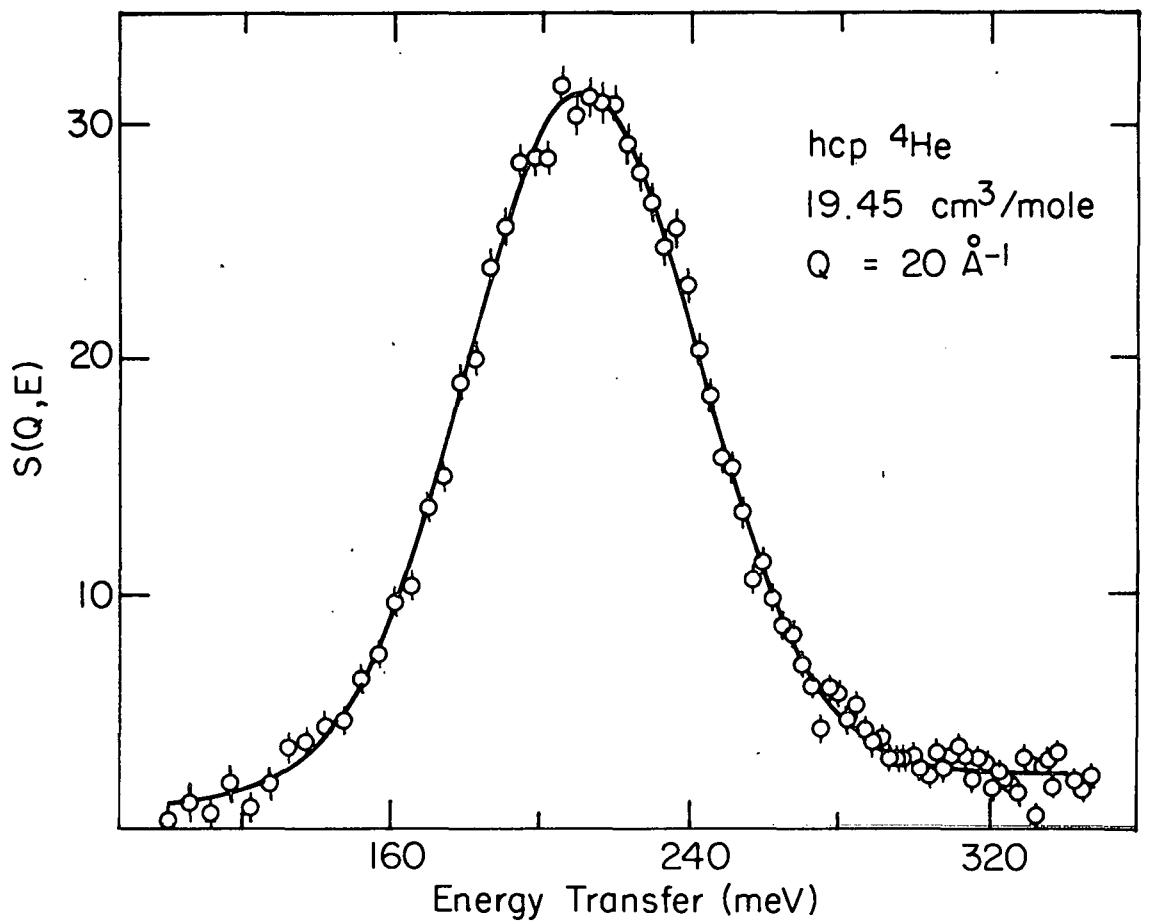

Figure 66. The dynamic structure factor versus energy transfer. These data represent $S(\vec{Q},E)$ interpolated to $Q = 20$ Å^{-1} for the low density hcp ^{4}He sample.

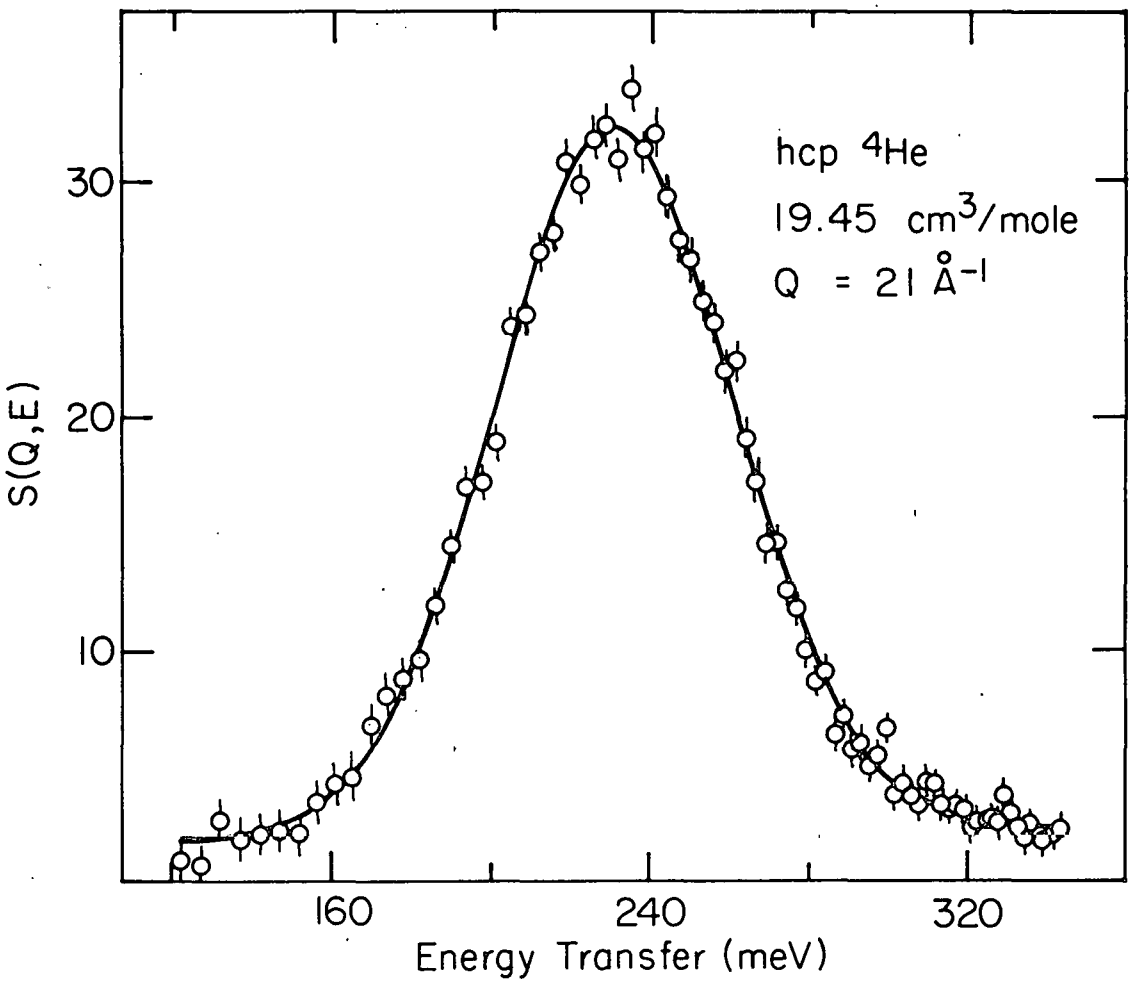

Figure 67. The dynamic structure factor versus energy transfer. These data represent $S(Q,E)$ interpolated to $Q = 21$ Å^{-1} for the low density hcp ^{4}He sample.

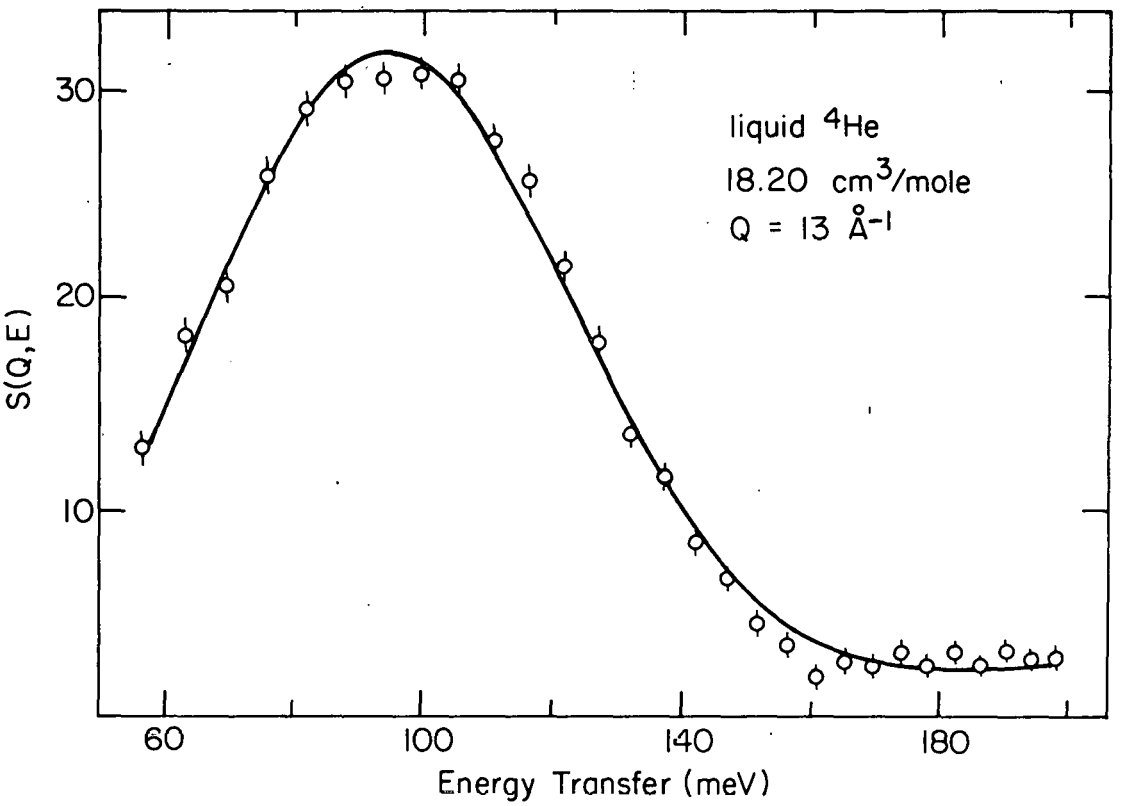

Figure 68. The dynamic structure factor versus energy transfer. These data represent $S(\vec{Q},E)$ interpolated to $Q = 13$ Å^{-1} for the liquid ^{4}He sample; the uncertainty in each point is indicated. The curve is the best fit Gaussian of the form given in Eqn. (32).

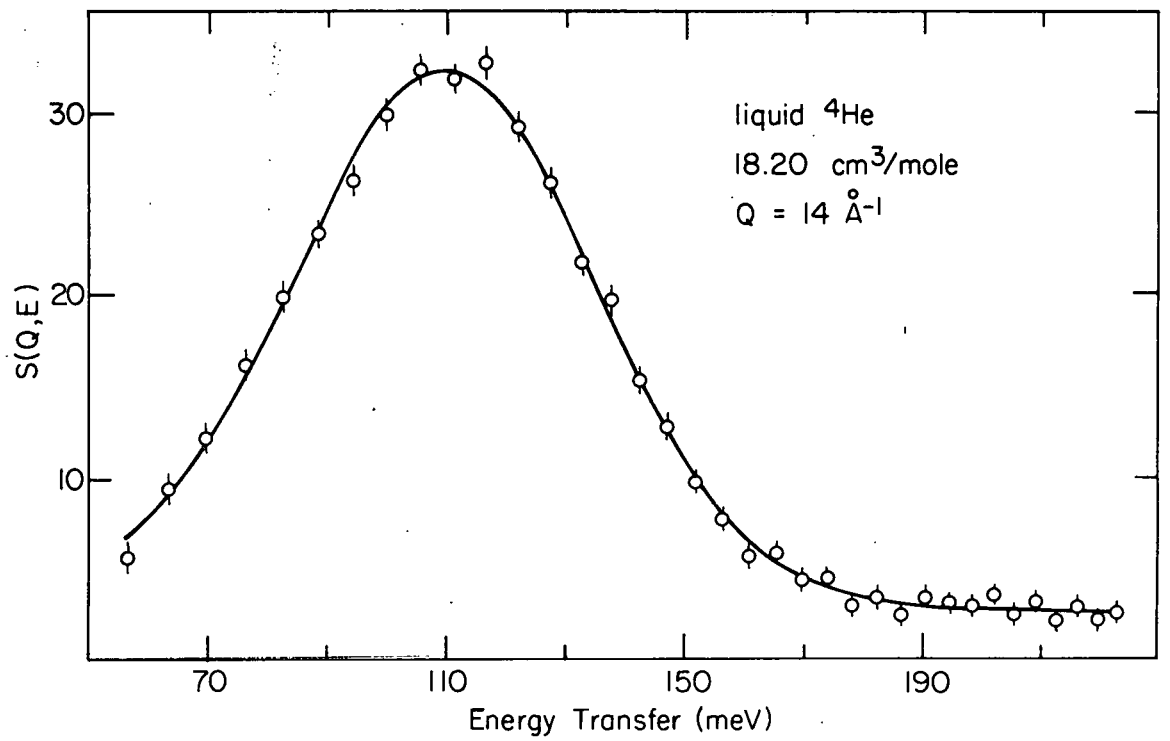

Figure 69. The dynamic structure factor versus energy transfer. These data represent $S(\vec{Q},E)$ interpolated to $Q = 14$ Å^{-1} for the liquid ^{4}He sample; the uncertainty in each point is indicated. The curve is the best fit Gaussian of the form given in Eqn. (32).

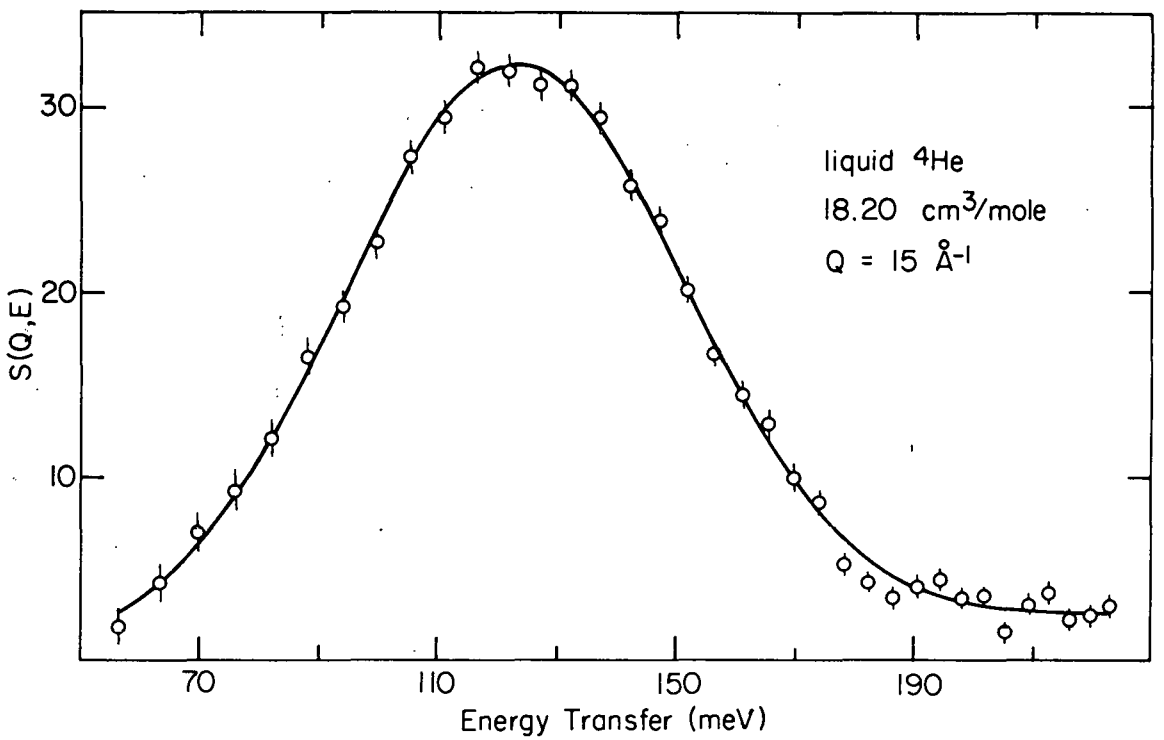

Figure 70. The dynamic structure factor versus energy transfer. These data represent $S(\vec{Q},E)$ interpolated to $Q = 15$ Å^{-1} for the liquid ^{4}He sample; the uncertainty in each point is indicated.

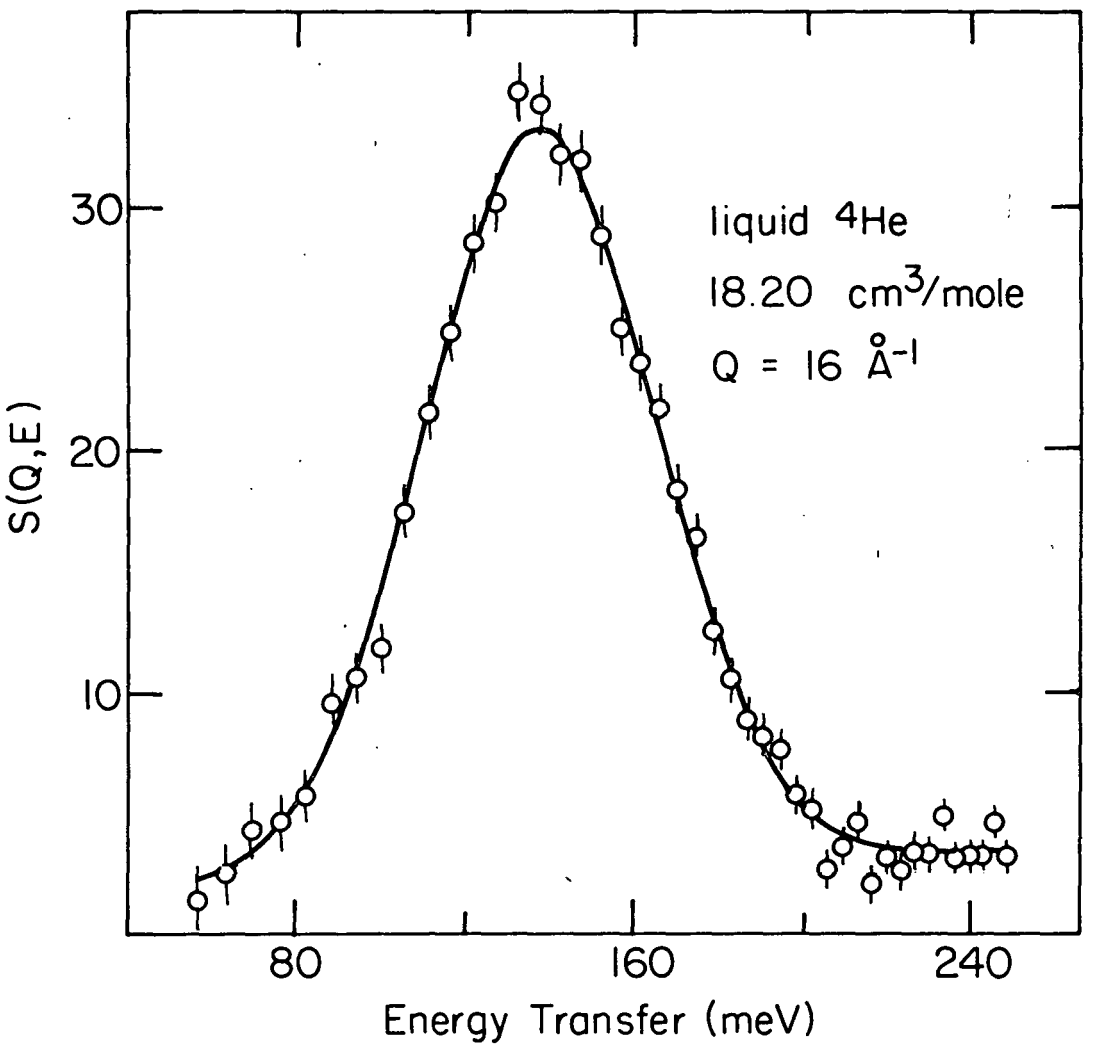

Figure 71. The dynamic structure factor versus energy transfer. These data represent $S(Q,E)$ interpolated to $Q = 16$ Å^{-1} for the liquid ^{4}He sample.

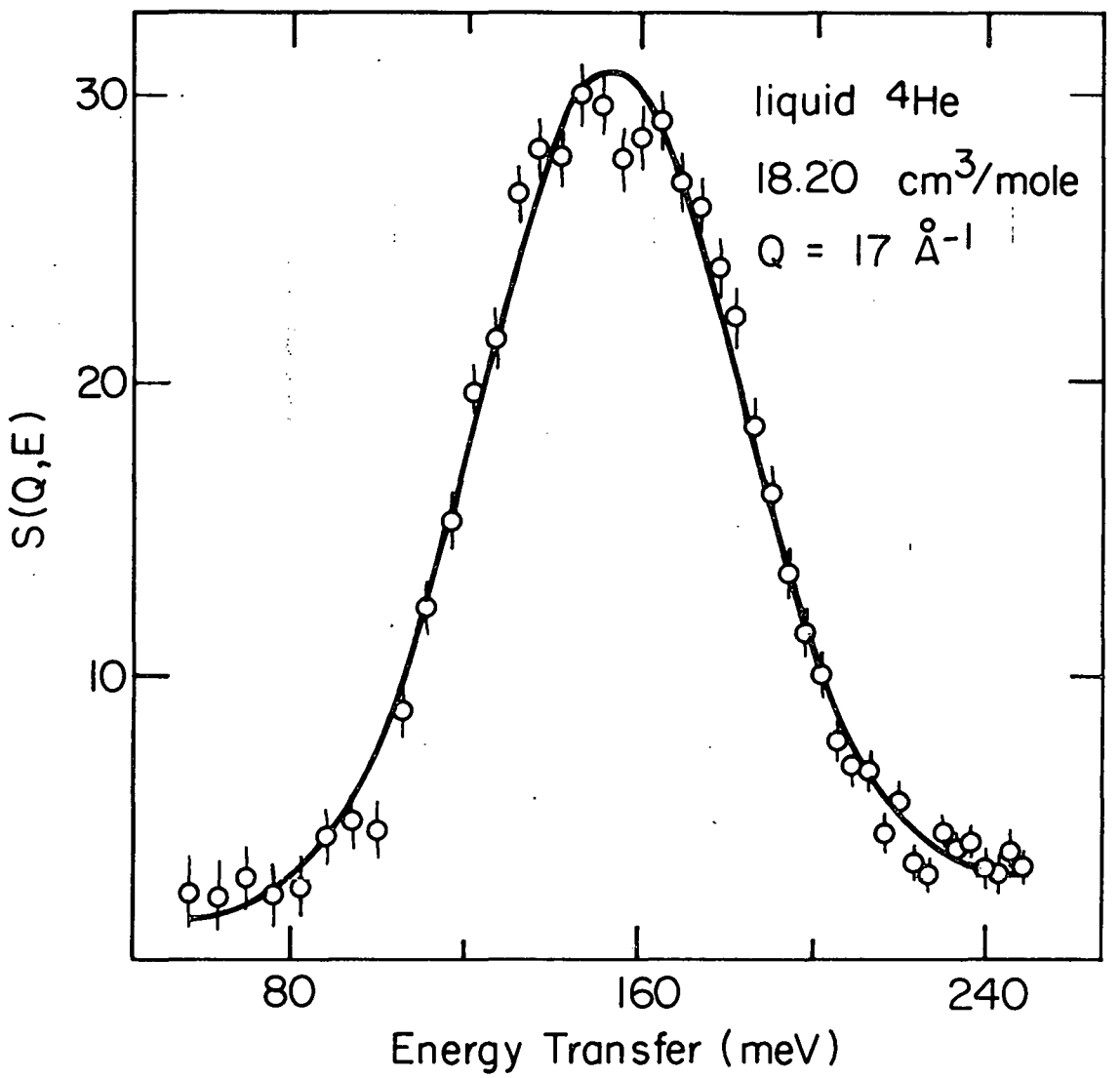

Figure 72. The dynamic structure factor versus energy transfer. These data represent $S(\vec{Q},E)$ interpolated to $Q = 17$ Å^{-1} for the liquid ^{4}He sample.

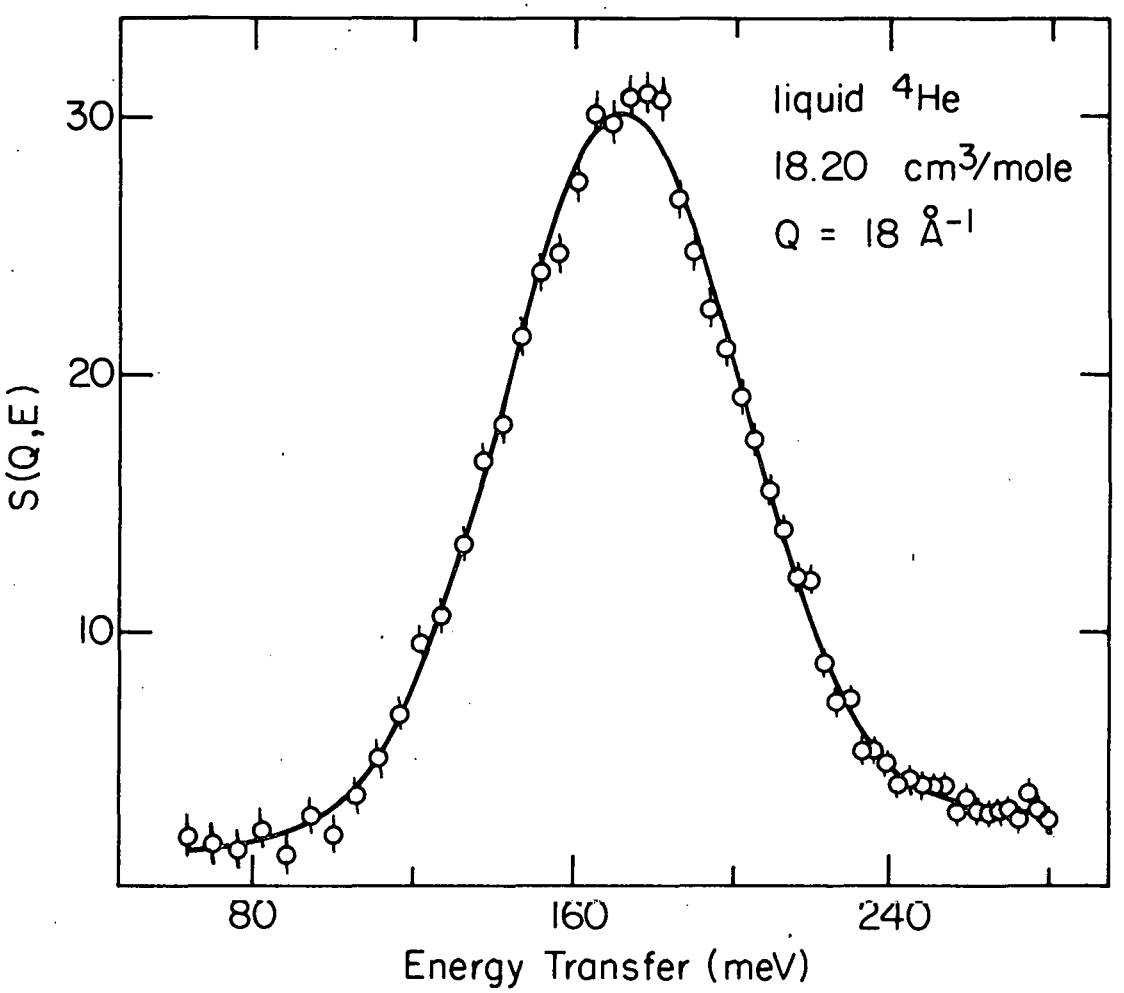

Figure 73. The dynamic structure factor versus energy transfer. These data represent $S(\vec{Q},E)$ interpolated to $Q = 18$ Å^{-1} for the liquid ^{4}He sample.

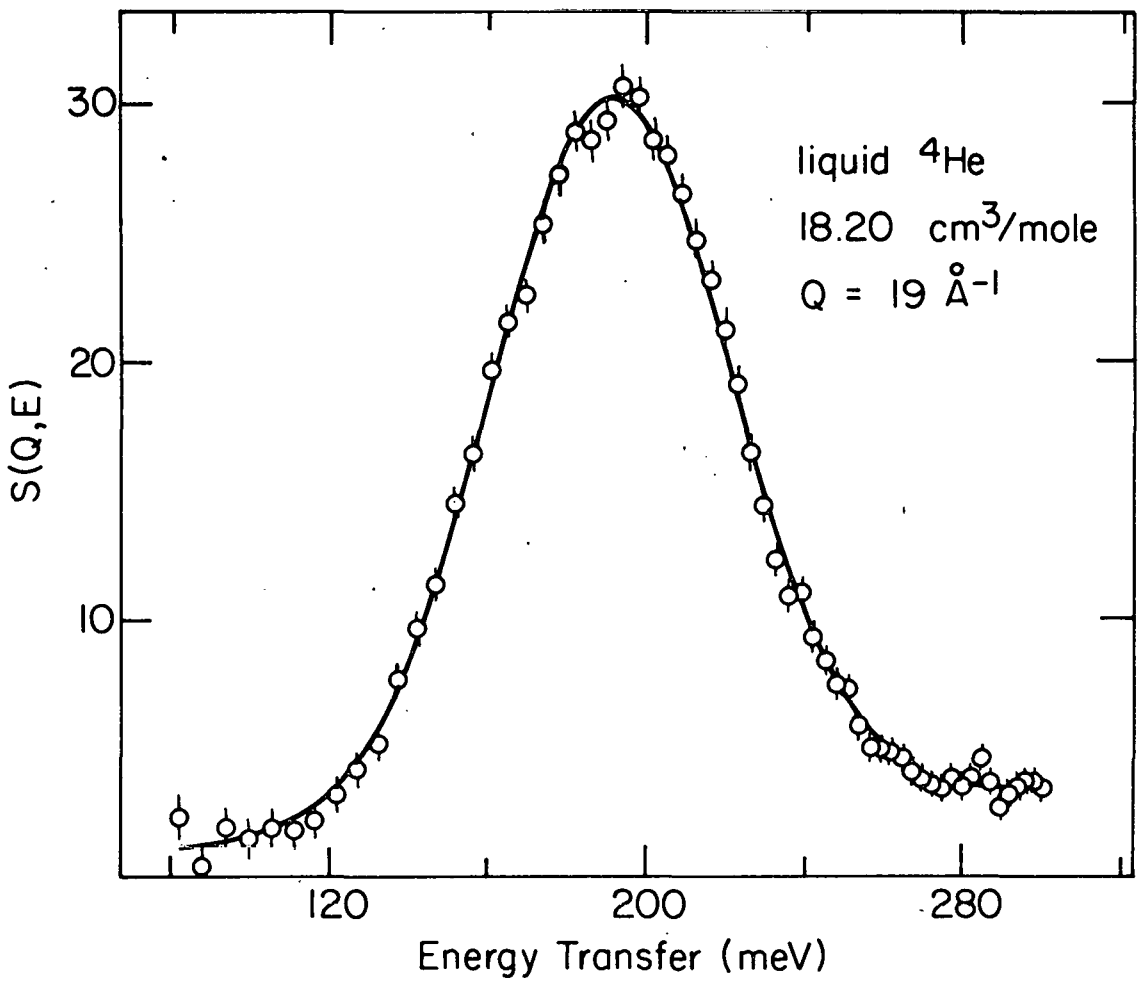

Figure 74. The dynamic structure factor versus energy transfer. These data represent $S(Q,E)$ interpolated to $Q = 19$ Å^{-1} for the liquid ^{4}He sample.

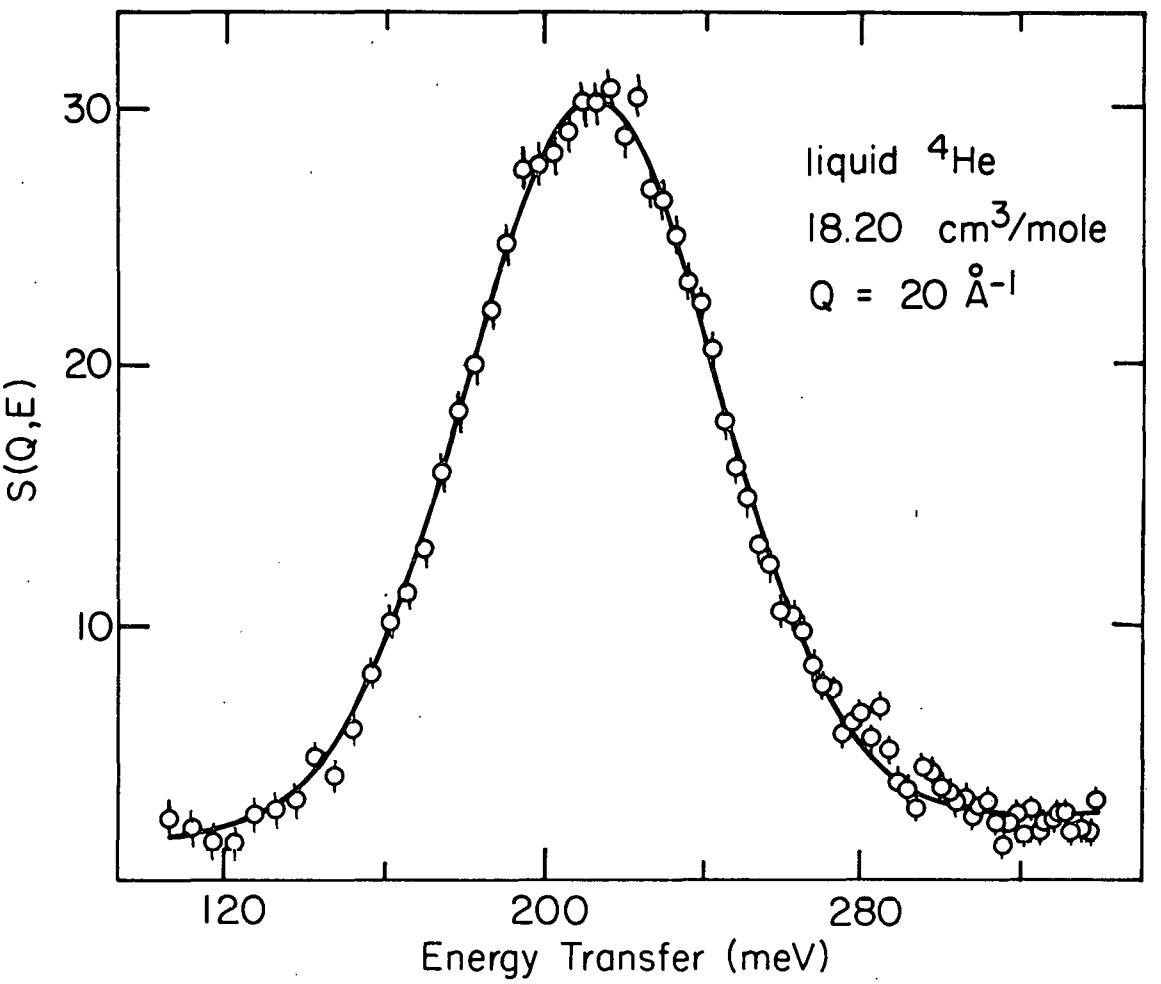

Figure 75. The dynamic structure factor versus energy transfer. These data represent $S(\vec{Q},E)$ interpolated to $Q = 20$ Å^{-1} for the liquid ^{4}He sample.

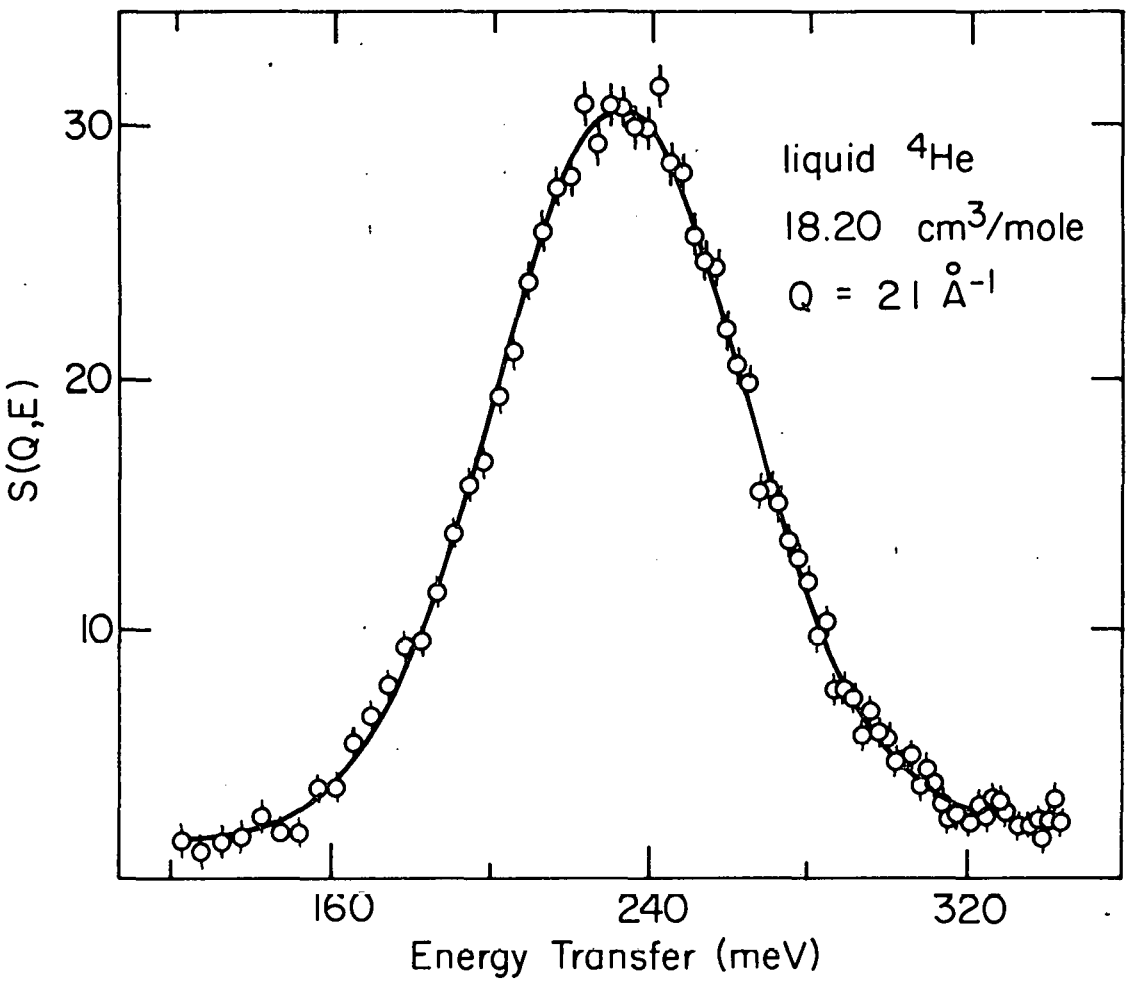

Figure 76. The dynamic structure factor versus energy transfer. These data represent $S(\vec{Q},E)$ interpolated to $Q = 21$ Å^{-1} for the liquid ^{4}He sample.

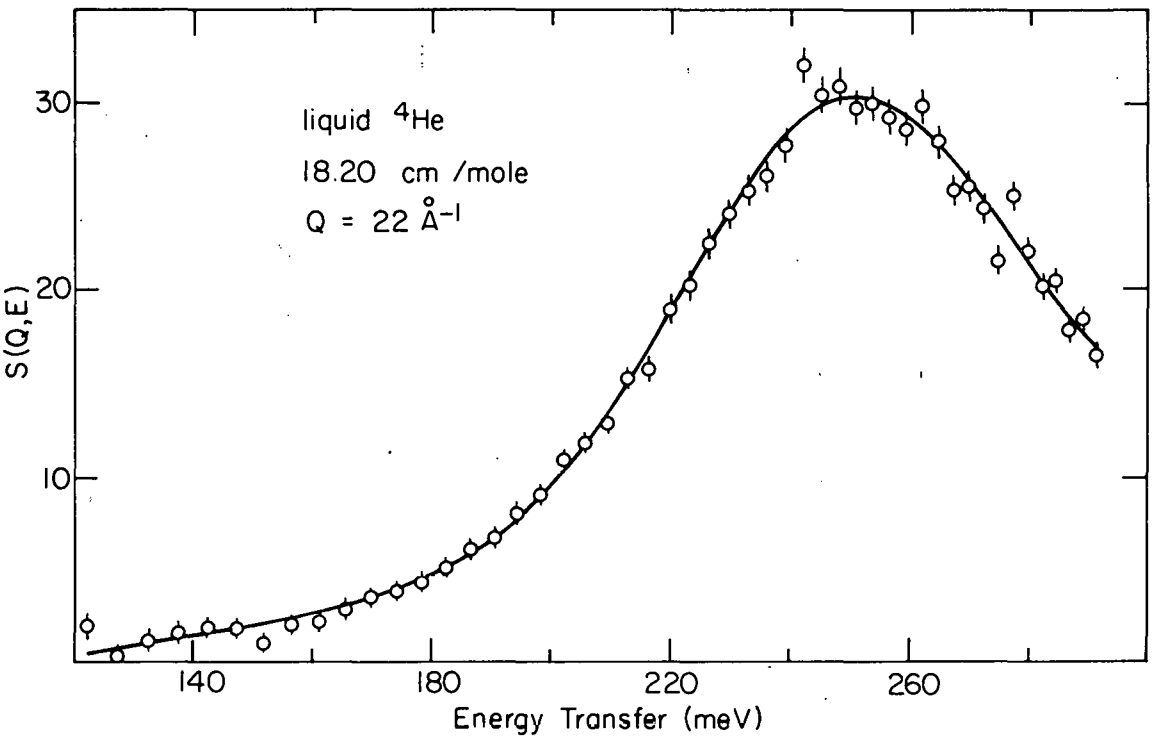

Figure 77. The dynamic structure factor versus energy transfer. These data represent $S(\vec{Q},E)$ interpolated to $Q = 22$ Å^{-1} for the liquid ^{4}He sample.

from the observed peak width. Since $S(\vec{Q},E)$ and the resolution function are both Gaussians, and since the widths of convoluted Gaussians add in quadrature, the conversion from σ_ϕ to σ_Q is

$$\sigma_Q^2 = (1 - C_\phi)^2 \sigma_\phi^2 - \sigma_R^2 \qquad (33)$$

and c_ϕ is given by Equation (26). These conversions have been carried out for all three samples and the resultant σ_Q's are given in Tables 2, 3 and 4.

One of the predictions of the impulse approximation is the expected linear relationship between σ_Q and Q (Equation (19)). Figures 78 and 79 are plots of the σ_Q versus Q for the two solid samples (Figure 78) and the liquid sample (Figure 79). The size of the points is the uncertainty in the values of σ_Q. From Equation (19) we expect the functional relationship between σ_Q and Q to be linear, have a zero intercept, and have a slope equal to $(\hbar^4 A/2M^2)^{1/2}$. This is a further test of the applicability of the impulse approximation.

The straight lines in Figures 78 and 79 are the best fit straight lines constrained to pass through the origin. From the slopes of these lines we extract the following values for the Gaussian parameter A:

$$\begin{aligned} A &= 3.42 \pm 0.10 \ \text{Å}^{-2} \quad \text{for } 19.45 \ \text{cm}^3/\text{mole solid} \\ &= 3.78 \pm 0.10 \ \text{Å}^{-2} \quad \text{for } 18.20 \ \text{cm}^3/\text{mole solid} \\ &= 3.73 \pm 0.06 \ \text{Å}^{-2} \quad \text{for } 18.20 \ \text{cm}^3/\text{mole liquid} \ . \end{aligned} \qquad (34)$$

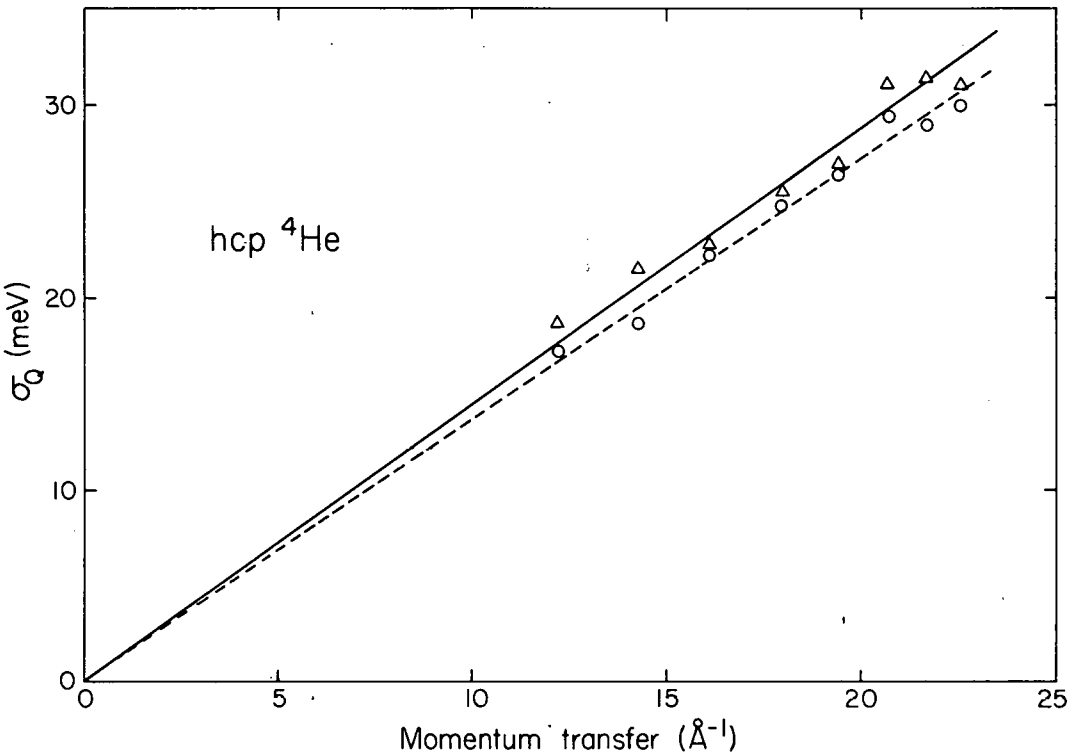

Figure 78. The standard deviation of $S(\vec{Q},E)$ versus momentum transfer. The data for the two hcp ^{4}He samples at the eight scattering angles is plotted. The triangles represent the high density solid, the circles represent the low density solid; the uncertainty in each point is represented by the size of the symbol. According to Eqn. (19), σ_Q is proportional to Q with a proportionality constant that depends on the Gaussian parameter A (see Eqn. (13)) and the mass of the scattering atom. The two lines are the best fit straight lines constrained to pass through the origin; the solid line is the fit for the high density solid, the dashed line is the fit for the low density solid. The single-atom Gaussian parameter, A, is extracted from the slope of the line. Some of the scatter in the data is due to anisotropy in the solids.

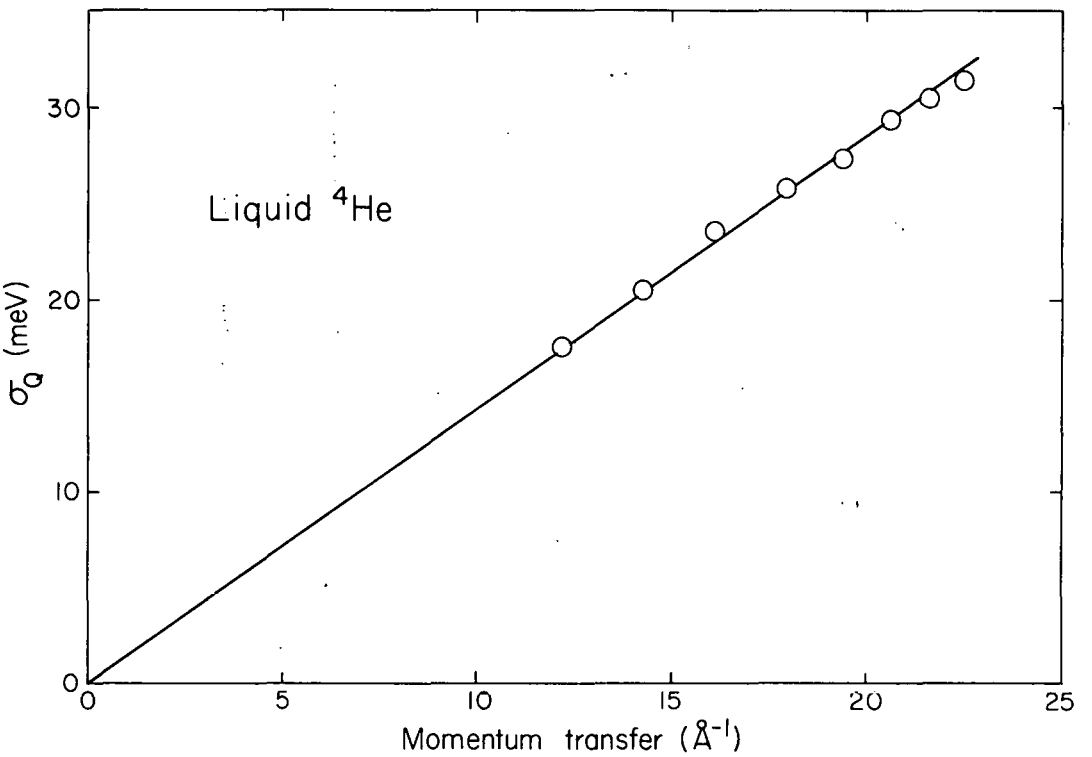

Figure 79. The standard deviation of $S(\vec{Q},E)$ versus momentum transfer. The circles represent the data for the liquid ^{4}He sample at the eight scattering angles; the size of the symbols represents the uncertainty. According to Eqn. (19), σ_Q is proportional to Q with a proportionality constant that depends on the Gaussian parameter A (see Eqn. (13)) and the mass of the scattering atom. The line is the best fit straight line constrained to pass through the origin. The single-atom Gaussian parameter, A, is extracted from the slope of the line.

Using Equation (20), one can convert these values of A into values of the expectation value of the kinetic energy of a ^{4}He atom. These are

$$\begin{aligned} \langle KE \rangle &= 31.1 \pm 0.9 \text{ K} \quad \text{for } 19.45 \text{ cm}^3\text{/mole solid} \\ &= 34.3 \pm 0.9 \text{ K} \quad \text{for } 18.20 \text{ cm}^3\text{/mole solid} \\ &= 33.8 \pm 0.6 \text{ K} \quad \text{for } 18.20 \text{ cm}^3\text{/mole liquid .} \end{aligned} \tag{35}$$

In comparing these values with theoretical results, one needs to compare the kinetic energy values with calculated single-atom kinetic energies. One cannot directly compare the above values of A with theoretical values unless the theories use the same many-atom wave function. In the next chapter we will compare the above results with theoretical calculations.

C. Compton Defects

In Figure 58, one will notice that the peak centers for smaller Q lie above the line expected for single particle scattering. In Compton scattering experiments, such deviations are termed Compton defects. They are referred to as positive Compton defects if the points lie above the line and negative Compton defects if they lie below the line. In the case of Compton scattering, the origin of these defects is understood[52] and similar effects in inelastic neutron scattering probably give rise to the observed neutron Compton defects. In our data, all the Compton defects are positive (see Tables 2, 3 and 4) but

negative Compton defects have been observed in inelastic neutron scattering from solid ^{4}He at lower momentum transfer.[53]

Negative Compton defects arise when the spectator atoms (atoms in the vicinity of the scattering atom) recoil with the scattering atom thus increasing the effective mass of the scattering atom. We see from Equation (17) that this gives rise to energy transfers that are smaller than expected for a given momentum transfer meaning the corresponding peak center will fall below the expected E_r versus Q^2 curve. This is precisely what occurred in the first observation of a single-atom scattering peak by Kitchens et al.[53] Their experiment involved inelastic neutron scattering from liquid and solid helium with momentum transfers in the range 2.5 to 5.5 $\mathring{A}^{-1}$. One would expect that as the momentum transfer increases the scattering event will become more like single-atom scattering and the negative Compton defect will approach zero. This is the trend one observes in Compton scattering.[54]

If one goes through the derivation in Equations (6) through (17) including a binding energy of the initial helium atom state and assuming the final state is unbound, one finds that the peak should be centered at a recoil energy of

$$E_r = \frac{\hbar^2 Q^2}{2M} + E_b \qquad (36)$$

where E_b is the binding energy. In the case of Compton scattering, this binding energy is the binding energy of the electron to the atom.[55] The binding energy of a helium atom in a solid at densities equal to those of our samples, is about 0.4 meV.[25] However, in our experiment we do not expect the binding energy to equal the positive Compton defect. To understand why, consider a helium atom in the bulk; nothing in the potential well in which such an atom sits corresponds to the binding energy, i.e. the potential does not become constant at an energy E_b above its minimum (as in a muffin tin potential). As the helium atom moves away from its equilibrium position, it encounters a sharp rise in its potential energy corresponding to the hard core repulsion of its nearest neighbor, which appears very high compared to the kinetic energy of the helium atom. As the helium atom recoils after the collision with the neutron, it passes between the neighboring atoms to an interstitial position. The potential it encounters along its path is certainly finite but is nevertheless very large compared to its zero point kinetic energy. This potential does not correspond to the binding energy of the atom in the solid.

To understand the origin of the positive Compton defect, we return to a classical view of the scattering process. The collision between the neutron and the helium atom occurs over a small, but finite, time interval. During

this time interval, the helium atom begins recoiling. As it recoils, its potential energy increases. This increase in potential energy during the collision gives rise to a positive Compton defect in the same way that the binding energy gives rise to a positive defect in Compton scattering. As the momentum transfer increases, the time duration of the scattering event decreases leading to a decrease in the change in the atom's potential energy that occurs during the collision. Thus this defect also approaches zero as the momentum transfer increases.

A rather interesting pattern is evident if one plots the Compton defect as a function of momentum transfer (the Compton defects are listed in Tables 2 through 4, momentum transfers are listed in Table 1). The first two points have a Compton defect of about 6 meV (the values range from 5.4 to 6.5 meV) while the third point has a defect of about 3 meV (2.8 to 3.6 meV). The Compton defect then goes to zero in a smooth fashion. This pattern holds for all three samples. This dramatic drop and the subsequent smooth decrease are the most significant features of the Compton defect versus momentum transfer plot. We can speculate about the origin of this sudden decrease in the Compton defect; however we emphasize that the following is speculation.

If one takes the single-particle wave function we have determined to be appropriate for a helium atom in a

cell model of the solid, one can calculate the energy spacing of the excited states by using a harmonic oscillator with the same wave function as a model. Such a calculation gives 4. meV as the energy level spacing for single-particle excitations of the helium atom in its potential. If one assumes the state only lasts one period of its oscillation, the uncertainty in its energy is 0.7 meV. It is possible that the sudden decrease in the Compton defect between the data taken at 57.3° and that taken at 66.9° is due to a transition that the helium atom makes from its ground state to the first excited state in its potential well. The helium atom does not remain long in this first excited state, in fact the helium atom is recoiling with a kinetic energy of about 100 meV and is in the process of tunneling among its neighbors to an interstitial site. The important point is that there does exist a first excited state to which the helium atom can make a transition. At sufficiently high momentum transfer, these effects must also disappear and the single-atom peak should be centered at the recoil energy given by Equation (17). One would expect that the contribution to the Compton defect due to the transition to the excited state would vanish suddenly as the momentum transfer is increased and the contribution due to the binding energy to approach zero smoothly. This is what we observe.

D. Anisotropy of $n(\vec{p})$

Moving now to Figures 78 and 79, we will try to explain why there is more "scatter" in the data than is expected from the uncertainty in each data point. One will notice that the data points in Figure 78 lie further from the expected σ_Q versus Q line than their uncertainties. At least some of this "scatter" is due to anisotropy in the solid samples. First, one will notice that the data points in Figure 79, σ_Q versus Q for the ^{4}He liquid, lie within their uncertainties of the straight line fit to the data. So in the case of our isotropic sample, the liquid, the deviation from the fit is not greater than the uncertainty. This is an indication that the scatter may be due to sample anisotropy but perhaps the diffraction data contain some information that will correlate preferred orientation of the sample with the observed deviation of a value of σ_Q from the fit to the data.

Certainly the scatter in the values of σ_Q cannot be attributed to any systematic error arising from misalignments in the sample with respect to the spectrometer because, of the eight sets of data (corresponding to the eight scattering angles) on the two solid samples, the deviations of the observed σ_Q comapred with the straight line fit have the same sign for four of the fits and opposite signs for four. One would expect a systematic error to give the same sign deviation for scattering at the same

angle from two unrelated samples. Any misalignment of the cryostat/spectrometer system (e.g. sample cell center being misaligned, sample cell not being vertical, chopper being misaligned) would have a small first order effect on the center of the observed peak and a second order effect on the peak width.

The following assumptions are implicit in our comparison of the diffraction data to deviations in Figure 78: 1) A helium atom in the solid is confined inside a volume whose shape and dimensions correspond to a Wigner-Seitz cell for a 18.20 cm^3/mole hcp ^4He lattice.[50] 2) The deviation from isotropy that we observe in a given sample direction (defined by $\vec{Q}$ for a given detector group) is representative of the deviation from isotropy for the entire sample in that direction. This assumption, though not exact for every sample and sample direction, is correct, on average, for a statistical ensemble of samples. It is the best estimate one can make given the limited data we have about the anisotropy of our sample. 3) The crystal did not rotate during the 67 hours we observed it. In his thesis,[41] B. A. Fraass describes observations of helium crystals that rotated in a cylindrical Lucite sample cell while x-ray diffraction data were being taken. We assume this did not happen in our case. 4) The anisotropy factor described below varies sufficiently slowly that it can be interpolated between two angles differing by about 5°.

For a powder spectrum, the integrated cross-section per unit cell for a reflection of multiplicity Z is

$$\sigma = \frac{\lambda^3 Z}{4V \sin(\phi/2)} |F|^2 \qquad (37)$$

where V is the volume of the unit cell, ϕ is the scattering angle, λ is the neutron wavelength and $|F|^2$ is the magnitude squared of the structure factor. The structure factors are easily calculated[57] and their magnitudes squared are listed in Table 5. The multiplicity factors, also listed in Table 5, are taken from Reference 58. The neutron wavelengths must be calculated for each peak at each angle since they depend on the lattice spacing and the scattering angle via the Bragg condition (Equation (24)). The relative amplitudes of the diffraction peaks at each angle are then calculated.

We include the anisotropy of the sample by assuming that each helium atom is confined in a volume defined by the Wigner-Seitz cell of a hcp lattice. Since the expectation value of the momentum of a particle in a potential well varies inversely with the width of the well, we expect the average value of the momentum of a helium atom in a given crystal direction to vary (approximately) inversely with the width of the Wigner-Seitz cell in that direction. That is, if our sample was a single crystal, the measured momentum distribution would be

Table 5. Summary of parameters and data associated with the diffraction data collected on the 18.20 cm^3/mole hcp ^4He sample. Each of the numbers in this table is associated with Bragg reflections from one set of lattice planes; the Miller indices of the seven observed reflections are listed in the top row. $|F|^2$ is the square of the structure factor for a monatomic hcp lattice. Z is the multiplicity of the scattering plane. The next row contains the calculated widths (perpendicular to the scattering plane), in Å, of the Wigner-Seitz cell for 18.20 cm^3/mole hcp ^4He. The last eight rows contain a summary of the diffraction data collected on the sample; the numbers are the amplitudes (in hundreds of neutrons) of observed Bragg peaks at the eight scattering angles.

	100	200	110	101	102	103	002
$\|F\|^2$	1	1	4	3	1	3	4
Z	6	6	6	12	12	12	2
Cell Width	3.499	3.499	3.499	3.654	3.774	3.887	4.285
ϕ = 47.7°	30				18.8	15	12.5
57.3°	3.6	16	8.3		45	8.3	37.5
66.9°					35	13.5	
77.7°	4.5		3.8				
87.3°	1.6						4.8
96.9°				6.2		1.2	8.8
105.9°			14.0	3.1			
115.5°		8.8	1.2	.9		1.0	

anisotropic with a directionally dependent width inversely proportional to the width of the Wigner-Seitz cell in that direction. However, our sample, being polycrystalline, has a momentum density given by the average of the momentum densities of all the crystallites in a given sample (as opposed to lattice) direction. The calculated widths of the Wigner-Seitz cell in crystal directions corresponding to the observed Bragg peaks (perpendicular to the corresponding reflecting planes) are given in Table 5.

One should keep in mind that our inelastic measurements determine the momentum distribution in the direction of $\vec{Q}$. In the diffraction (elastic) experiment, if a crystallite is aligned so that a (002) Bragg peak appears at a given scattering angle, then $\vec{Q}$ lies along the (002) direction in that crystallite. If one then carries out a spectroscopic experiment so that the momentum transfer is parallel to the $\vec{Q}$ in the diffraction experiment, one would measure the momentum distribution in the (002) direction for that crystallite. An important consideration in this analysis is that for scattering at a given angle, the momentum transfer, $\vec{Q}$, for a diffraction experiment is not parallel to the momentum transfer for a spectroscopic experiment. The lighter the scattering atom the greater will be the difference in the momentum transfers for these two types of experiments. Thus, one must compare the diffraction data taken at one angle with the spectroscopic

data taken at another angle determined so that the corresponding momentum transfers will be parallel.

Returning to our search for correlations between sample anisotropy and deviations of σ_Q from the straight line fit, we make two sums from our diffraction data. The first sum is the observed amplitude of a diffraction peak divided by the relative amplitude of the peak at that angle (including the Debye-Waller factor) summed over all the observed peaks at each scattering angle. The second sum is the peak amplitude divided by the relative amplitude and the width of the Wigner-Seitz cell perpendicular to the reflecting planes summed over the observed peaks at each scattering angle. The anisotropy factor that we define is the second sum divided by the first and is associated with the sample direction defined by $\vec{Q}$ in the inelastic scattering experiment. Dividing by the first sum essentially normalizes the anisotropy factor so that the factor calculated for a few relatively small peaks can be compared with a factor calculated for several relatively large peaks. With this view in mind, the anisotropy factor is just the weighed average of the inverse of the Wigner-Seitz cell width normalized with the assumption that the fraction of the sample that gives rise to the Bragg peaks is representative of the full sample.

We next calculate the direction of $\vec{Q}$ for the diffraction measurement at each of the eight scattering angles and the direction of $\vec{Q}$ for the spectroscopic measurement at

each scattering angle. We then interpolate the anisotropy factors between the elastic-scattering $\vec{Q}$ directions so that the interpolated factors and the inelastic scattering data correspond to momentum transfers in the same direction. We expect a positive correlation between these interpolated anisotropy factors and the deviation of the corresponding σ_Q from the straight line fit to our σ_Q versus Q plot. We can make this comparison for only the six lowest Q points because our diffraction data do not extend to as large angles (between $\vec{Q}$ and the unscattered beam) as the inelastic data.

We find very good correlation between the magnitude of the interpolated anisotropy factor and the sign of the deviation of σ_Q from the fit (five of the six points are so correlated). The correlation coefficient[51] between the interpolated anisotropy factor and the σ_Q deviation (sign and magnitude) is 0.56. The fact that the correlation coefficient is less than 1.0 (complete correlation) reflects the fact that there remains scatter in the data (expected to be roughly as large as the scatter in the liquid data) and unobserved sample anisotropy (probably the case of the one point for which the σ_Q deviation seems to have the wrong sign).

A full analysis of the anisotropy requires construction of a pole figure diagram[59] which would require that diffraction data be taken at several different sample

orientations. This was not possible with our cryostat/ diffractometer system. However, we believe that the correlation between the anisotropy factor and the σ_Q deviations indicates that most of the scatter in the data is due to anisotropy of the sample. It would be interesting to carry out this experiment on a single-crystal ^{4}He sample so that the anisotropy of the momentum distribution could be directly measured.

6. SUMMARY

Spallation neutron sources have made a variety of experiments possible that are, at best, difficult with a reactor based source. The availability of high flux epithermal neutron beams makes feasible experiments in which single atom motion can be studied. If one can attain sufficiently high momentum transfer, one can extract the single-atom momentum distribution by making the impulse approximation. The single-atom position space wave function can be inferred, in principle, from a sufficiently precise momentum distribution. Because the wave functions of nearest neighbor atoms in solid helium have significant overlap, knowledge of the single-atom wave function is important in determining the interaction of near neighbor atoms.

Analysis of our experimental data depends on the applicability of the impulse approximation to scattering of epithermal neutrons from condensed matter. The limits on the applicability of the impulse approximation in the case of Compton scattering are well understood. There are enough differences between Compton scattering and inelastic neutron scattering, however, that the generally accepted rules of applicability for the impulse approximation cannot be translated simply from the former to the latter sets of experiments.

There are characteristics of the data peaks that indicate when sufficient momentum transfer has been attained to satisfy requirements that are necessary (though not sufficient) for the applicability of the impulse approximation. The first characteristic is that the peak should be centered about an energy transfer that is the same as one would expect if the neutrons scattered from free helium atoms (Equation (17)). We find this is satisfied quite well (Figure 58) with deviations qualitatively explained in terms of binding energy effects on the scattering event. These effects seem to have vanished at the higher momentum transfers attained in this experiment. Further, the width of $S(\vec{Q},E)$ should be proportional to the momentum transfer. This is also satisfied (Figures 78 and 79). Deviations of the peak widths from the linear fit for data on crystalline specimens seem, in part, to be due to sample anisotropy. It would be extremely interesting to measure the anisotropy of the momentum distribution in single crystal hcp ^{4}He. Estimates (my own) indicate that the Gaussian parameter, A, measured along the (001) and (100) directions in the 18.20 cm^3/mole sample should be 3.07 and 4.60 $\mathring{A}^{-2}$ respectively, a difference that should be easily observable.

The data show a fully resolved single-atom scattering peak. The dynamic structure factor extracted from this peak is fit to a symmetric Gaussian function. While

published calculations indicate that leading order corrections to the impulse approximation introduce an asymmetry to the structure factor;[60] our data show no such asymmetry or other systematic deviation from Gaussian behavior. A Gaussian $S(\vec{Q},E)$ implies that the momentum density is Gaussian which implies that the single-atom wave function is Gaussian. This justifies the assumption (Equation (2)) that the single-atom wave function is Gaussian. From the experimentally determined structure factor, the Gaussian parameter in the single-atom wave function (Equation (18)) can be determined.

Since particle exchange and vacancy tunneling are affected strongly by the part of the wave function in the tails, the extent to which the tails of the peaks depart from a Gaussian shape is of great interest. We could find no systematic departure in our data. A detailed Monte Carlo calculation of the spectrometer resolution is planned; this, along with further experiments that will collect larger data sets to decrease the experimental uncertainty about the shape of the tails, should be helpful in searching for systematic deviations from Gaussian behavior. One should be cautious about such plans since it is precisely in the tails of the data that Weinstein and Negele[43] have shown that the measurement cannot be expected to give the momentum density unambiguously. Theories, however, have commonly indicated that the momentum

density should be Gaussian. The Green's Function Monte Carlo calculation by Whitlock et al.,[25] which gave generally good results for the properties of solid helium that were calculated, found a momentum density that shows no appreciable deviation from Gaussian behavior for the top 99% of the peak.[27] Below this, there is an intriguing departure from Gaussian shape. So, within present experimental uncertainties, the experimental evidence is that there is no deviation from a Gaussian momentum density, while the theoretical evidence is that the deviation is only in the extreme tails.

In order to compare our results to theory, we need a calculation of the kinetic energy of the atoms in the solid. Many authors[8,19,61] have calculated single-atom wave function Gaussian parameters for hcp ^{4}He (and even more have calculated Gaussian parameters for bcc ^{3}He[8,19,61,62,63,64]). However, these results are not directly comparable to our results since these authors include correlations differently and therefore their kinetic energy per atom is not related to the Gaussian parameter by Equation (20). There have been two published calculations that report single-atom kinetic energies[25,26] and since they find nearly the same values for the kinetic energy, we will compare our results with the more recent calculation.

The calculation by Whitlock et al.[25] was carried out on solid and liquid ^{4}He. Their calculation on the solid was carried out on fcc ^{4}He interacting with a Lennard-Jones potential at molar volumes that range from 24.0 to 17.0 cm^3/mole (they quote the sample density in dimensionless units of $\rho\sigma_L^3$, in which units their densities range from 0.420 to 0.592). Though their calculation was done on a fcc structure, a subsequent calculation[65] indicated that the difference between the results using a fcc instead of a hcp structure is minimal. The calculation on liquid and solid ^{4}He yielded theoretical values for the Bose condensate fraction, the total energy, the kinetic energy, the potential energy, the pressure, the speed of sound, the structure factor, and the compressibility. Compared to available experimental values for pressure, compressibility, and total energy[56] for the solid phase, their results are very good but often outside the quoted uncertainty. Their results for the kinetic energy per atom are compared with our results and displayed in Figure 80 (note that zero has been suppressed and the results are displayed in terms of Gaussian parameter or single-atom kinetic energy versus sample density or sample molar volume). The uncertainties in the theoretical values are given as the size of the points while the uncertainties in our results are indicated by the error bars. Obviously, the results do not agree. I hasten to point out that the

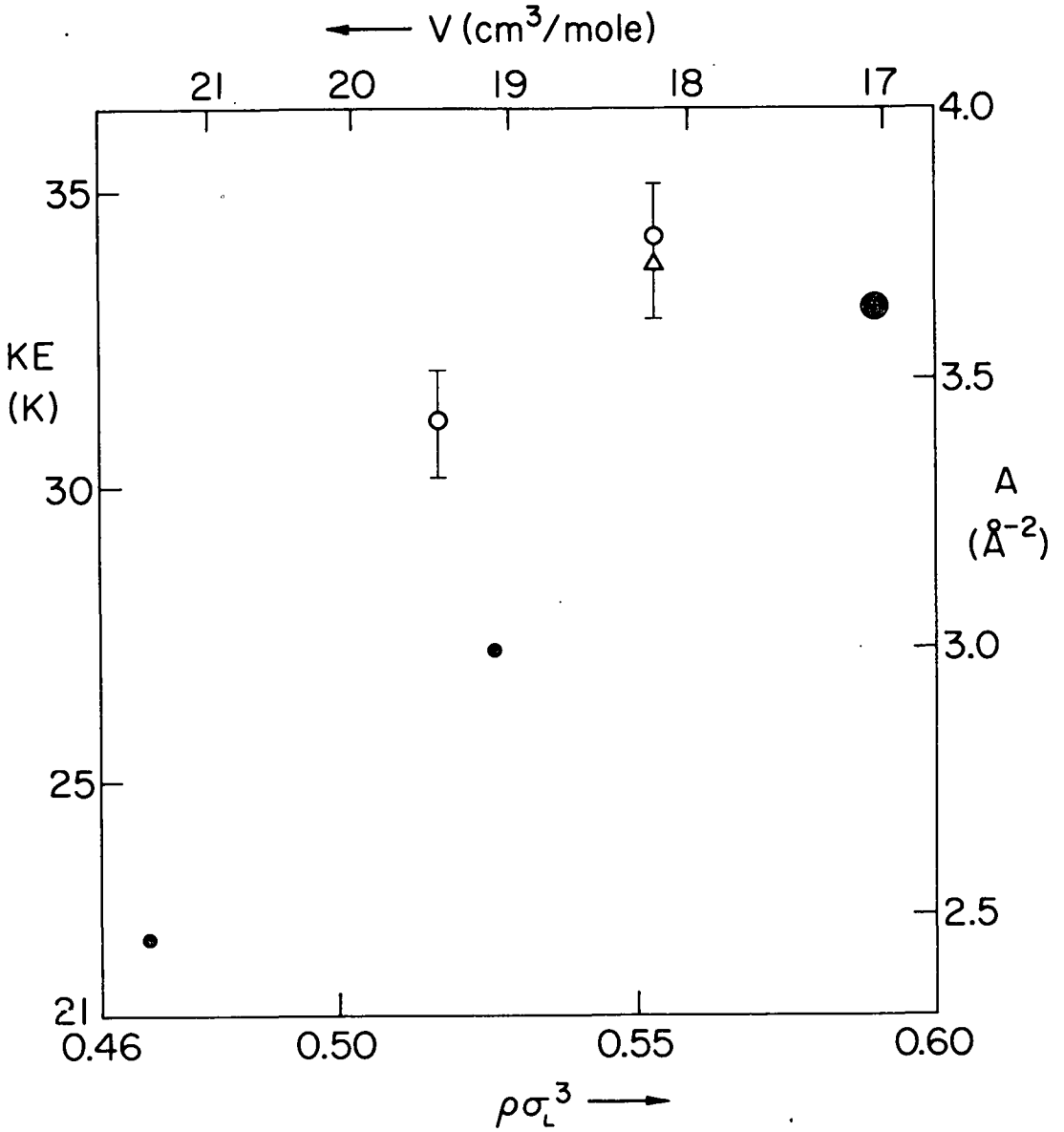

Figure 80. A comparison of the present results with those reported by Whitlock et al. The kinetic energy (K/atom) is plotted versus helium density. The solid circles represent the theoretical data, the size of the symbols representing the uncertainty. The open circles represent the results of the present experiment on the two solid samples; the triangle represents the liquid sample result.

slopes of the two curves are the same; that is, they both have the same dependence of the kinetic energy or molar volume.

An obvious difference between our experiment and the calculation is that the experiment was conducted at 1.70 K while the calculation was carried out at 0 K. To see if we can explain the different results in terms of this temperature difference, we can use the Debye model for the specific heat to determine the energy difference between solid helium at 0 K and at 1.70 K. The Debye temperature for solid helium at 18.20 cm^3/mole is 38 K. If we integrate the Debye specific heat between 0 and 1.7 K, we find the energy difference between these two states of the solid, in temperature units, to be 0.009 K per atom. So we see that the solid at 1.70 K is essentially in its ground state.

Comparing the theoretical results with other experimental results we find that the zero temperature pressures calculated by Whitlock et al. are below those measured by Edwards and Pandorf[56] for hcp ^{4}He by about 20%. This implies that the kinetic energy per atom in solid ^{4}He is higher than indicated by this calculation.

One should be able to estimate the change in single-atom kinetic energy necessary to increase the pressure by 20%. Since the theory and experiment give the same dependence of single-atom kinetic energy on molar volume,

one can assume that this value is accurate. The derivative of the expectation value of the single-atom kinetic energy with respect to the molar volume is

$$\frac{\partial \langle KE \rangle}{\partial V} = -2.56 \text{ K mole/cm}^3. \tag{38}$$

We know the compressibility from the work of Edwards and Pandorf. Interpolating between their values to find the compressibility for hce ^{4}He at 0 K, one finds

$$\kappa = \frac{1}{V}\frac{\partial V}{\partial P} = \begin{array}{l} -0.160 \times 10^{-2} \text{ atm}^{-1} \text{ for } 18.20 \text{ cm}^3\text{/mole} \\ -0.242 \times 10^{-2} \text{ atm}^{-1} \text{ for } 19.45 \text{ cm}^3\text{/mole} \end{array} . \tag{39}$$

Combining these one finds

$$\frac{\partial \langle KE \rangle}{\partial P} = \begin{array}{l} 0.074 \text{ K/atom for } 18.20 \text{ cm}^3\text{/mole} \\ 0.121 \text{ K/atom for } 19.45 \text{ cm}^3\text{/mole} \end{array} . \tag{40}$$

Inserting the increases in pressure necessary to make the theoretical pressures agree with the measurements, one finds that corresponding values for <KE> will increase by

$$\Delta \langle KE \rangle = \begin{array}{l} 1.00 \text{ K for } 18.20 \text{ cm}^3\text{/mole} \\ 1.21 \text{ K for } 19.45 \text{ cm}^3\text{/mole} \end{array} . \tag{41}$$

Thus one finds some consistent qualitative discrepancies between the theoretical results and experiments, but the results still differ by more than the estimated uncertainties.

Referring again to Figure 80, one will notice that the kinetic energy of the high density solid sample is 0.5 K higher than the kinetic energy of the liquid sample with the same density. This result agrees quite well with the calculation by Whitlock et al. For solid and liquid helium at a molar volume of 22.86 cm^3/mole, they find that the solid has a kinetic energy about 1.4 K per atom higher than the liquid. At higher density, the trend in their data is toward a smaller difference in the kinetic energies of the two phases. If one extrapolates (using a quadratic function fit to the data) their results for the liquid to 18.20 cm^3/mole and interpolates their results for the solid to the same density, one finds that the difference in kinetic energies to be about 0.3 K per atom. Considering the unjustified nature of the above extrapolation and the relatively large error bars on our experimental results, these two results are very close.

The reason that the atoms in the solid have a higher kinetic energy than those in the liquid at the same molar volume is due, in part, to the uncertainty principle. The atoms in the two phases have, on average, the same volume per atom; however, the atoms in the solid are restricted to lattice sites. Because they are more restricted in position space, the atoms in the solid have broader momentum-space wave functions which implies a higher kinetic energy.

There remain questions about the applicability of the impulse approximation to inelastic neutron scattering to determine atomic momentum distributions. By all criteria currently available, our experimental method is valid. Further measurements of momentum densities in the various phases of solid and liquid ^{3}He and ^{4}He (as well as other suitable solids) are planned. By exploration of a broader range of experimental conditions, these should help answer any remaining questions about this experimental method.

APPENDIX A

In discussing the Compton defect in Chapter 5, mention was made of a cell model for the ^{4}He solid in which each atom was treated as a ground state harmonic oscillator whose wave function is a Gaussian, given by Eqn. (2), with widths as determined by the present experiment (Eqns. (34)). In this appendix, this model will be discussed in more detail.

The ground state wave function for a harmonic oscillator is given by

$$\psi(r) = C \exp[-r^2\sqrt{Mk}/2\hbar] \tag{A.1}$$

where k is the oscillator force constant. Equating this wave function with the single-atom wave function we have determined to be appropriate for the ground state of hcp helium (Eqn. (2)), one finds

$$k = \frac{\hbar^2 A^2}{M} \tag{A.2}$$

and for the frequency

$$\omega = \sqrt{\frac{k}{M}} = \frac{\hbar A}{M} \ . \tag{A.3}$$

We thus find the energy level spacing for the three dimensional harmonic oscillator model to be

$$\Delta E = \hbar\omega = 3.58 \text{ meV for } 19.45 \text{ cm}^3/\text{mole}$$
$$= 3.95 \text{ meV for } 18.20 \text{ cm}^3/\text{mole} . \qquad (A.4)$$

Now, our model for the ground state of the solid looks very much like an Einstein model, a collection of oscillators all having the same frequency. One can calculate the Einstein temperature, θ_E, thus

$$\theta_E = \frac{\hbar\omega}{k_B} = 41.3 \text{ K for } 19.45 \text{ cm}^3/\text{mole}$$
$$= 45.7 \text{ K for } 18.20 \text{ cm}^3/\text{mole} . \qquad (A.5)$$

And, using an approximation from Born and Huang,[66] one can estimate the Debye temperature

$$\theta_D \sim .75\ \theta_E = 31.1 \text{ K for } 19.45 \text{ cm}^3/\text{mole}$$
$$= 34.3 \text{ K for } 18.20 \text{ cm}^3/\text{mole} \qquad (A.6)$$

(compare these values with Eqns. (35)). These θ_D's are consistent with the values found by Ahlers interpolated to 1.7 K (29.6 K and 35.9 K respectively).[67] Whether the θ_D's in Eqn. (A.6) are within the uncertainties of those reported by Ahlers depends on the uncertainty one assigns to Eqn. (A.6).

From the Debye temperature, one can estimate the Grüneisen parameter from

$$\gamma = -\frac{V}{\theta_D}\frac{\Delta\theta_D}{\Delta V} . \qquad (A.7)$$

Taking the average of our molar volumes for V and the average of our Debye temperatures for θ_D, one finds

$$\gamma = 2.89 \ . \qquad \text{(A.8)}$$

Though not within the uncertainty, this is consistent with the 1.7 K value found by Ahlers[68] of about 2.7.

REFERENCES

1. J. Chadwick, Proc. Royal Soc. A 136, 692 (1932).

2. H. Kamerlingh Onnes, Konink. Akad. Wetensch. Amsterdam, Proc. 11, 168 (Sept. 8, 1908).

3. R. J. Bell and I. J. Zucker, in Rare Gas Solids, Vol. 1, ed. M. L. Klein and J. A. Venables, (Academic Press, New York, 1976), Chap. 2.

4. J. N. Murrell in Rare Gas Solids, Vol. 1, ed. M. L. Klein and J. A. Venables, (Academic Press, New York, 1976), Chap. 3.

5. J. de Boer and A. Michels, Physica 6, 97 (1939).

6. Q. N. Usmani, S. Fantoni, and V. R. Pandharipande, Phys. Rev. B 26, 6123 (1982).

7. R. A. Aziz, V. P. S. Nain, J. S. Carley, W. L. Taylor, and G. T. McConville, J. Chem. Phys. 70, 4330 (1979).

8. L. H. Nosanow, Phys. Rev. 146, 120 (1966).

9. E. R. Grilly, J. Low Temp. Phys. 11, 33 (1973).

10. E. R. Grilly and R. L. Mills, Annals of Physics 8, 1 (1959).

11. W. Ramsay and M. W. Travers, Roy. Soc. Proc. 63, 437 (1898).

12. R. W. Gray and W. Ramsay, J. Chem. Soc. 95, 1073 (1909).

13. H. R. Glyde, in Rare Gas Solids, Vol. 1, ed. M. L. Klein and J. A. Venables, (Academic Press, New York, 1976), Chap. 8.

14. R. A. Guyer, R. C. Richardson, and L. I. Zane, Rev. Mod. Phys. 43, 432 (1971).

15. F. W. DeWette and B. R. A. Nijboer, Phys. Lett. 18, 19 (1965).

16. N. Bernardes, Phys. Rev. 112, 1534 (1958).

17. L. H. Nosanow and G. L. Shaw, Phys. Rev. 128, 546 (1962).

18. R. Jastrow, Phys. Rev. 98, 1479 (1955).

19. J. H. Heterington, W. J. Mullin, and L. H. Nasanow, Phys. Rev. 154, 175 (1967).

20. K. A. Brueckner and C. A. Levinson, Phys. Rev. 97, 1344 (1955).
K. A. Brueckner, Phys. Rev. 100, 36 (1955).

21. F. Iwamoto and H. Namaizawa, Prog. Theor. Phys. Sup. 37 and 38, 234 (1966).

22. R. A. Guyer, in Solid State Physics, Vol. 23, ed. F. Seitz, D. Turnbull, and H. Ehrenreich, (Academic Press, New York, 1969), p. 413.

23. H. Horner, Phys. Rev. A 1, 1712 (1970).

24. H. R. Glyde and F. C. Khanna, Can. J. Phys. 49, 2997 (1971).

25. P. A. Whitlock, D. M. Ceperley, G. V. Chester, and M. H. Kalos, Phys. Rev. B 19, 5598 (1979).

26. J. P. Hansen and E. L. Pollock, Phys. Rev. A 5, 2651 (1972).

27. P. A. Whitlock, private communication.

28. Compton Scattering, ed. B. Williams, (McGraw-Hill, New York, 1977).

29. J. H. Heterington, Phys. Rev. 176, 231 (1968).

30. G. L. Squires, Introduction to the Theory of Thermal Neutron Scattering, (Cambridge Univ. Press, Cambridge, 1978).

31. P. C. Hohenberg and P. M. Platzman, Phys. Rev. 152, 198 (1966).

32. L. Van Hove, Phys. Rev. 95, 249 (1954).

33. C. G. Windsor, Pulsed Neutron Scattering (Taylor and Francis, London, 1981).

34. D. L. Price, J. M. Carpenter, C. A. Pelizzari, S. K. Sinha, I. Breshof, and G. E. Ostrowski, in Proc. VI Meeting of the International Collaboration on Advanced Neutron Sources, Argonne National Laboratory, June 1982, Argonne National Laboratory Report ANL-82-80, pp. 207-215 (1983).

35. B. N. Brockhouse, Bull. Amer. Phys. Soc. 5, 462 (1960).

36. J. R. D. Copley, D. L. Price, J. M. Rowe, Nuc. Instr. and Methods 107, 501 (1973).

37. D. L. Price and S. K. Sinha (to be published).

38. P. M. Platzman and N. Tzoar, Phys. Rev. 139, A410 (1965).

39. B. J. Bloch and L. B. Mendelsohn, Phys. Rev. A 9, 129 (1974).

40. P. Eisenberger and P. M. Platzman, Phys. Rev. A 2, 415 (1970).

41. B. A. Fraass, Ph.D. Dissertation, University of Illinois at Urbana-Champaign (1980).

42. L. J. Rodriguez, H. A. Gersch, and H. A. Mook, Phys. Rev. A 9, 2085 (1974).

43. J. J. Weinstein and J. W. Negele, Phys. Rev. Lett. 49, 1016 (1982).

44. J. J. Weinstein, Ph.D. Dissertation, Massachusetts Institute of Technology (1982).

45. D. S. Kupperman, Ph.D. Dissertation, University of Illinois at Urbana-Champaign (1970).

46. L. E. DeLong, O. C. Symko, and J. C. Wheatley, Rev Sci. Instr. 42, 147 (1971).

47. D. Lazarus and W. D. Seward, AEC Report No. C00-1198-519.

48. Union Carbide Ultra-high purity helium has a minimum purity of 99.999%.

49. A. T. Stewart and B. N. Brockhouse, Rev. Mod. Phys. 30, 250 (1958).

50. N. W. Ashcroft and N. D. Mermin, Solid State Physics, (Holt, Rinehart and Winston, New York, 1976), p. 73.

51. P. R. Bevington, Data Reduction and Error Analysis for the Physical Sciences, (McGraw Hill, New York, 1969).

52. L. B. Mendelsohn, in Momentum Wavefunctions--1982, ed. E. Weigold, (American Institute of Physics, New York, 1982), p. 211.

53. T. A. Kitchens, G. Shirane, V. J. Minkiewicz, and E. B. Osgood, Phys. Rev. Lett. 29, 559 (1972).

54. R. H. Stuewer and M. J. Cooper in Compton Scattering, ed. B. Williams, (McGraw-Hill, New York, 1977), Chap. 1.

55. I. E. McCarthy and R. A. Bonham, in Momentum Wave Functions--1976, ed. D. W. Devine (American Institute of Physics, New York, 1976), p. 255.

56. D. O. Edwards and R. C. Pandorf, Phys. Rev. A 140, 816 (1965).

57. C. Kittel, Introduction to Solid State Physics, 5th Ed. (John Wiley, New York, 1976), p. 58.

58. International Tables for X-ray Crystallography, Vol. I, ed. N. F. M. Henry and K. Lonsdale, (Kynoch Press, Birmingham, 1952), p. 33.

59. C. S. Barrett, Structure of Metals, (McGraw Hill, New York, 1952).

60. H. A. Gersch, L. J. Rodriguez, and P. N. Smith, Phys. Rev. A 5, 1547 (1972).

61. H. A. Goldberg and R. A. Guyer, J. Low Temp. Phys. 28, 449 (1977).

62. H. R. Glyde and F. C. Khanna, Can. J. Phys. 50, 1143 (1972).

63. H. Bolterauer and P. Gillessen, J. Low Temp. Phys. 26, 193 (1977).

64. R. A. Guyer and B. Sarkissian (unpublished). B. Sarkissian, Ph.D. Dissertation, Duke University (1968).

65. P. A. Whitlock, M. H. Kalos, G. V. Chester, and D. M. Ceperley, Phys. Rev. B 21, 999 (1980).

66. M. Born and K. Huang, Dynamical Theory of Crystal Lattices, (Clarendon Press, Oxford, 1954).

67. G. Ahlers, Phys. Rev. A 2, 1505 (1970).

68. G. Ahlers, Phys. Lett. 24A, 152 (1967).

VITA

Russell Otto Hilleke was born in [redacted] He received his secondary education at Gadsden High School, graduating in June 1969. He attended Georgia Tech from which he received a B.S. degree with honor, and no small relief, in June 1973. He served two years with the U.S. Army, his first position being assistant S-2 with the 49th Air Defense Artillary Group at Ft. Lawton, Washington. He was then assigned as a Physicist at the Ballistics Research Lab, Aberdeen Proving Ground, Maryland. Since August 1975, he has attended the University of Illinois where he has held teaching and research assistantships in the Department of Physics. He received a M.S. degree in physics in August 1976. He is a member of the American Physical Society.